8-1-2017

Remote sensing of the environmental impacts of utility-scale solar energy plants

Mohammad Masih Edalat
University of Nevada, Las Vegas, masih.edalat@yahoo.com

REMOTE SENSING OF THE ENVIRONMENTAL IMPACTS OF UTILITY-SCALE SOLAR ENERGY PLANTS

By

Mohammad Masih Edalat

Bachelor of Science- Civil Engineering
Islamic Azad University Najafabad Branch, Iran
2009

Master of Science- Environmental Engineering
Shiraz University, Iran
2012

A dissertation submitted in partial fulfillment
of the requirements for the

Doctor of Philosophy- Civil and Environmental Engineering

Department of Civil and Environmental Engineering and Construction
Howard R. Hughes College of Engineering
The Graduate College

University of Nevada, Las Vegas
August 2017

UNLV | GRADUATE COLLEGE

Dissertation Approval

The Graduate College
The University of Nevada, Las Vegas

July 25, 2017

This dissertation prepared by

Mohammad Masih Edalat

entitled

Remote Sensing of the Environmental Impacts of Utility-Scale Solar Energy Plants

is approved in partial fulfillment of the requirements for the degree of

Doctor of Philosophy- Civil and Environmental Engineering
DEPARTMENT

Haroon Stephen, Ph.D.
Examination Committee Chair

Kathryn Hausbeck Korgan, Ph.D.
Graduate College Interim Dean

Sajjad Ahmad, Ph.D.
Examination Committee Member

Jacimaria Batista, Ph.D.
Examination Committee Member

Ashok Singh, Ph.D.
Examination Committee Member

Dale Devitt, Ph.D.
Graduate College Faculty Representative

ABSTRACT

Solar energy has many environmental benefits compared with fossil fuels but solar farming can have environmental impacts especially during construction and development. Thus, in order to enhance environmental sustainability, it is imperative to understand the environmental impacts of utility-scale solar energy (USSE) plants. During recent decades, remote sensing techniques and geographic information systems have become standard techniques in environmental applications. In this study, the environmental impacts of USSE plants are investigated by analyzing changes to land surface characteristics using remote sensing. The surface characteristics studied include land cover, land surface temperature, and hydrological response whereas changes are mapped by comparing pre-, syn-, and post- construction conditions.

In order to study the effects of USSE facilities on land cover, the changes in the land cover are measured and analyzed inside and around two USSE facilities. The principal component analysis (PCA), minimum noise fraction (MNF), and spectral mixture analysis (SMA) of remote sensing images are used to estimate the subpixel fraction of four land surface endmembers: high-albedo, low-albedo, shadow, and vegetation. The results revealed that USSE plants do not significantly impact land cover outside the plant boundary. However, land-cover radiative characteristics within the plant area are significantly affected after construction. During the construction phase, site preparation practices including shrub removal and land grading increase high-albedo and decrease low-albedo fractions.

The thermal effects of USSE facilities are studied by the time series analysis of remote sensing land surface temperature (LST). A statistical trend analysis of LST, with seasonal trends removed is performed with a particular consideration of panel shadowing by analyzing sun angles for different times of year. The results revealed that the LST outside the boundary of the solar plant

does not change, whereas it significantly decreases inside the plant at 10 AM after the construction. The decrease in LST mainly occurred in winters due to lower sun's altitude, which casts longer shadows on the ground.

In order to study the hydrological impacts of PV plants, pre- and post-installation hydrological response over single-axis technology is compared. A theoretical reasoning is developed to explain flows under the influence of PV panels. Moreover, a distributed parametric hydrologic model is used to estimate runoff before and after the construction of PV plants. The results revealed that peak flow, peak flow time, and runoff volume alter after panel installation. After panel installation, peak flow decreases and is observed to shift in time, which depends on orientation. Likewise, runoff volume increases irrespective of panel orientation. The increase in the tilt angle of panel results in decrease in the peak flow, peak flow time, and runoff.

This study provides an insight into the environmental impacts of USSE development using remote sensing. The research demonstrates that USSE plants are environmentally sustainable due to minimal impact on land cover and surface temperature in their vicinity. In addition, this research explains the role of rainfall shadowing on hydrological behavior at USSE plants.

ACKNOWLEDGMENTS

This research is based upon work supported by the National Science Foundation under grant number IIA-1301726. I would like to acknowledge NSF for providing me with the opportunity to work in the project titled "Solar Energy-Water-Environment Nexus".

I would like to express my profound gratitude to my academic advisor, Dr. Haroon Stephen, for his scholastic advice and technical guidance throughout this investigation. His devotion, patience, and focus on excellence allowed me to reach this important milestone in my life. In addition, special thanks to Dr. Sajjad Ahmad, Dr. Jacimaria Batista, Dr. Ashok Singh, and Dr. Dale Devitt for their guidance, suggestions and contributions to my Advisory Committee.

Lastly, but not least, my thanks are extended to my wife, my parents, and my sister for their love and patience throughout my education.

DEDICATION

This dissertation is dedicated to my wife, Mahtab, for her love and unwavering support and sacrifice. We have grown smarter, wiser and continue to learn together.

To my parents, Mr. Heshmatollah Edalat and Mrs. Marzieh Sharifian. Without their continued and unconditional love and support, I would not be the person I am today.

TABLE OF CONTENTS

LIST OF TABLES

LIST OF FIGURES

1. CHAPTER 1- INTRODUCTION

1.1 Background

With the awareness that fossil fuels are depleting, many nations are adding renewable resources to their energy portfolios, such as geothermal, wind, and solar energy. Although harvesting solar energy has been around for a while, not until recently has this topic gained interest as a renewable energy resource, especially in areas having bright sunshine year-round. Solar energy has brought many environmental benefits compared with fossil fuels such as reduction in the emissions of greenhouse gases. These effects have resulted in increased interest in solar plants installations, and subsequently fast growth of utility-scale solar energy plants with many pending permits for installations planned for the future. As more of these plants appear on the landscape, a major challenge is to understand the adverse effects on the environment causing from changes in surface characteristics of the land. These effects depend on the size, type, and location of the installations and must be addressed appropriately in energy policies.

The motivation of this study is to enhance environmental sustainability and to promote large-scale societal benefits from renewable solar energy projects. Therefore, it is essential to quantify and minimize adverse environmental impacts of solar energy projects. Remote sensing, a powerful tool in environmental sciences is used to achieve this goal.

1.2 Description of the Problem

Harnessing the sun's energy with utility-scale solar energy (USSE) plants is growing fast but their environmental effects are not well understood. A USSE plant construction can cause significant ecosystem disturbance by fragmentation of landscape and alteration of energy balances

in adjacent plant communities. Remote sensing is a powerful tool, which can be useful to study the environmental effects of solar energy plants. Remote sensing has not been applied previously to investigate the environmental impacts of solar facilities. This study provides an insight to understand the environmental impacts of utility-scale solar energy development using remote sensing techniques.

With the awareness that fossil fuels are depleting, many nations are rapidly expanding renewable resources such as solar energy. Although harvesting solar energy has been around for a while, not until recently has this topic gained interest as a renewable energy resource, especially in areas having a high number of sunshine days on a yearly basis. In the United States, high solar insolation levels in the Southwestern united states creates significant electricity generation potential, and the rapid development of solar energy plants in these areas represents this fact (Bureau of Land Management & U.S. Department of Energy, 2015). In the US, more than 60% of megawatt (MW) capacity of the current USSE plants (projects with capacities of 20 MW or greater) (Bureau of Land Management, 2012) are located in California, Nevada and Arizona (Solar Energy Industries Association, 2016). However, according to the Solar Energy Industries Association report published in September 2016, the current operating solar plants generate 15 gigawatts (GW) electricity in the US while the plants that are under construction and development are going to generate 43 GW. Thus, it is expected to see more USSE plants appearing on the southwest US landscape in the near future.

Like any typical construction and development, solar plants can have environmental impacts on habitat, animals, plants and soil during the construction and operation phases. According to Phillips (Phillips, 2013) and Tsoutsos et al. (Tsoutsos, Frantzeskaki, & Gekas, 2005),

the main advantages of solar energy compared with fossil fuels energy are reduced emissions of greenhouse gases, reduced transmission lines, reclamation of degraded land, and improved quality of water resources, among others. In addition, the environmental impacts of photovoltaic (PV) cell production can also be reduced by converting to more advanced production process by reducing water consumption and emissions (Andersen, Gilpin, & Andrae, 2014). These positive effects of solar energy have resulted in increased interest in USSE installations in the US, with many pending permits for installations planned for the future (Bureau of Land Management, 2016). On the other hand, solar energy installations can have adverse impacts on biodiversity, land-use, soil, water resources, human health, land fragmentation, and changes in microclimate. As more of these plants appear on the landscape, a major challenge is to understand their effects on land-use and changes in surface characteristics of the land. These effects depend on the size, type, and location of the installations (Phillips, 2013; Tsoutsos et al., 2005), and must be addressed appropriately by energy policies.

During recent decades, remote sensing techniques and geographic information systems have been widely used in many environmental applications because remote sensing data covers large geographic areas with high temporal frequency. Some of the well-known applications of remote sensing are in urban and regional planning, agriculture, disasters, hydrology and water resources and flood control, forestry, land-use and land-cover analysis (Thenkabail, 2016). The large spatio-temporal coverage, cost effectiveness, time-efficiency, and accessibility are the most important reasons of using remote sensing for environmental impact assessment.

1.3 Thesis Statement

In this study, the environmental impacts of USSE plants are investigated by analyzing changes to land surface characteristics using remote sensing. The surface characteristics studied include land cover, land surface temperature, and hydrological response whereas changes are mapped by comparing pre-, syn-, and post- construction conditions. Remote sensing image analysis is used to estimate change of land cover and land surface temperature. Hydrological modeling is used to estimate change to surface water drainage pattern.

It is hypothesized that USSE plants alter land cover and land surface temperature both inside and outside the plants boundary. During construction and operation phases, land cover is directly altered inside plant areas due to site preparation and panel installation. Previous studies have shown that there is a strong linkage between land-cover change and local climate change in an area. Moreover, solar plants alter energy balance in a region and that can impact land surface temperature and land cover. Therefore, the impact on land cover and land surface temperature is expected to decrease with distance from the plant, resulting in a spatial halo around the plant.

It is also hypothesized that PV panels reduce rainfall infiltration loss during a storm, and therefore, leads to increase in runoff volume. Since solar panels are expected to create rain shadows, the area below the panels does not receive direct rainfall, instead it is routed to the edge of the panel resulting in a concentrated downpour. Therefore, the impact on hydrological response of the area is expected to depend on tilt angle of panels which is related to the covered area under the panels. The panel orientation relative to the dominant slope is also expected to impact the time of peak flow.

With a perspective of above hypotheses, following three specific objectives undertaken in this research are

1. To measure the change in land cover between pre-, syn-, and post-installation of USSE plants;

2. To determine the change in land surface temperature (LST) due to USSE plants; and

3. To compare hydrological response of pre and post PV panel installation with single-axis tracking technology.

1.4 Research Contribution

This research provides an insight into the potential environmental impacts of USSE plants by utilizing remote sensing. Remote sensing techniques have been used to acquire information on land surface features in large spatio-temporal extent, and is capable of monitoring and tracking land surface characteristics. This research demonstrates that remote sensing is an appropriate and powerful tool in the analysis of the environmental impacts of solar facilities. Three specific applications of remote sensing including land cover, land surface temperature, and hydrological response analysis are provided in this study.

This research reveals the effect of USSE plants on land cover in arid region. It is confirmed that USSE plants do not significantly impact land cover outside the plant boundary. However, within plant area, the low- and the high-albedo surfaces is increased. The high-albedo increases during construction due to land preparation processes but it decreases later on. The low-albedo increases due to solar panels and exists beyond the construction phase. Since the studied plants are constructed in arid area, the fraction of vegetation was negligible before and after the construction.

This research demonstrates the use of Spectral Mixture Analysis (SMA) to estimate land cover at solar plants. The dimensionality reduction of the multiband imagery done by normalized principal component analysis (PCA) has the highest accuracy in comparison to minimum noise fraction (MNF) approach. However, SMA on MNF shows the highest accuracy to estimate vegetation fraction. This research provides a deeper analysis using subpixel remote sensing by applying SMA to solar plants.

This research assesses the thermal behavior of USSE plants and its vicinity. The time-series analysis of remote sensing based on land surface temperature is conducted in relation to changes in albedo and shading due to solar panels. It is shown that the LST outside the boundary of the solar plant does not change, whereas it significantly decreases inside the plant after the construction. The decrease is high during the winters because of the longer shadows on the ground. This research explains the shading due to panels and its relation to time of day and time of year. It shows the method to appropriately treat LST to remove seasonal and gradual temperature variation in the data. This research provides a synoptic perspective using gridded temperature field from remote sensing compared to previous studies based on point thermometric measurements from weather stations. This research delineates steps to use Landsat 5 Thematic Mapper (TM) and Landsat 8 Thermal Infrared Sensor (TIRS) based land surface temperature to study solar plants and their thermal behavior. The spatial and temporal coverage furnished by remote sensing data helps understand the thermal impacts of USSE plants.

This research analyses the hydrological impacts of single-axis PV trackers using high resolution remote sensing surface elevation data. The study of various PV panel installation scenarios reveals relations between panel orientation and tilt angle, and peak flow discharge, peak

flow time, and total runoff volume. This research reveals that PV panel installation increases runoff volume during a storm and that runoff peak flow can significantly alter after panel installation. The panel orientation impacts peak flow: it can reduce or increase depending on relative angle to the general slope. The research confirms that time to peak flow reduces when the panel orientation is facing along the general surface slope. The peak flow time can also be increased due to the orientation of the panel compared with pre-installation. This research on hydrological response of the solar plant is evaluated using theoretical and numerical approaches.

This research reveals that the impact of PV panel installation on spatial rainfall distribution and consequently hydrological response should not be neglected in the hydrological assessment of solar facilities. It shows that the change in spatial rainfall distribution due to solar panels is not negligible as generally assumed in hydrological assessment reports of solar plants that are only focused on alteration of soil characteristics. The research findings demonstrate the prediction of hydrological behavior of a solar farm needed for the superposition of the effects of rainfall redistribution and soil alteration needed for better assessment especially in case of heavy storm events.

This research investigates the environmental impacts of USSE plants, a fast-growing industry with diverse sizes, types, and locations. In particular, the impacts on land cover, land surface temperature, and hydrological behavior are studied with the application of remote sensing data and analysis. The research confirms that USSE plants can be considered as environmentally sustainable due to minimal impact on land cover and surface temperature in their vicinity. In addition, this research demonstrates an insight into the changes in hydrological behavior due to

USSE plants. However, USSE PV plants alter hydrological behavior in a region by changing the spatial rainfall distribution reaching the ground and site preparation practices.

1.5 Dissertation Outline

The dissertation provides a study of the environmental impacts of USSE by analyzing changes to land surface characteristics using remote sensing. Brief outline for each chapter is provided as follows. The Chapter 2 provides a summary of the previous studies in environmental impacts of solar plants. It includes general background on the benefits and impacts of solar plants, comparison of solar and conventional energy resources, impacts on land use and land cover, thermal impacts, and impacts on hydrology. Then, applications of remote sensing regarding environmental impacts studies are reviewed. The Chapter 3 describes the research about the effects of USSE facilities on land cover in desert area. This study analyzed the land-cover trends by measuring changes in the land-cover fractions inside and around USSE facilities using remote sensing. The thermal effects of USSE facilities are provided in the Chapter 4. The time series of land surface temperature with particular comparison of pre- and post-installation conditions are analyzed for this purpose. The hydrological impacts of PV plants are discussed in the Chapter 5. The pre- and post-installation hydrological response over single-axis technology for various tilt angles and orientation angles are compared. The Chapter 6 provides conclusions and recommendations.

2. CHAPTER 2- LITERATURE REVIEW

The following review summarizes the previous studies on environmental impacts of solar plants. It includes benefits and impacts of solar plants, comparison of solar and conventional energy resources, life-cycle assessment of PV cells, impacts on land-use and land cover, thermal impacts, and impacts on hydrology. The review closes with applications of remote sensing regarding environmental impacts studies are reviewed.

2.1 Benefits versus Negative Impacts of Solar Plants

Although several studies have established benefits of solar energy (Mekhilef, Saidur, & Safari, 2011; Solangi, Islam, Saidur, Rahim, & Fayaz, 2011) during the last decade, many have investigated environmental and social effects of solar energy installations, including on biodiversity, visual effects relating to the loss of amenities as well as visual intrusion from an aesthetic viewpoint, land-use, degrading soil structure, reduce water resources, land fragmentation, and thermal effects in the surrounding area (Barron-Gafford et al., 2016; Chiabrando, Fabrizio, & Garnero, 2009; Edalat & Stephen, 2017; El Chaar, Lamont, & El Zein, 2011; Grippo, Hayse, & O'Connor, 2015; R. R. Hernandez et al., 2014; Tsoutsos et al., 2005). Aman et al. listed some of the positive and negative impacts of solar energy (M.M. Aman et al., 2015) and El Chaar et al. reviewed the environmental issues regarding the development of existing PV technologies (El Chaar et al., 2011). In a general overview of some environmental effects by solar technology, Tsoutsos et al. have graded the potentially negative effects, such as visual impacts, the routine and accidental release of chemicals, land-use, work safety and hygiene as well as the effect on the ecosystem and on water resources (Tsoutsos et al., 2005). They suggested that the potential environmental burdens of solar installations depend on the size and nature of the project, and often

are site-specific. Thus, although solar energy has brought significant benefits to planet earth, it still has environmental effects that need to be addressed and evaluated in more details such as impacts on land cover, temperature, and hydrological impacts.

2.2 Comparison of Solar Energy and Conventional Energy Resources

Some studies have provided information on environmental benefits by comparison of solar energy and conventional energy resources. Hosenuzzaman et al. has compared the emissions of PV technologies with coal and natural gas power plants, and therefore the health benefits that can be a result of emission reduction (Hosenuzzaman et al., 2015). Turney and Fthenakis compared the intensity of land-use for life-cycles of PV power from the installation and operation of USSE plants with that for coal power (Turney & Fthenakis, 2011). Using two kinds of metrics, transformation and occupation, they found that as the age of the power plant increased, the land-use intensity of PV power became significantly smaller than that for a coal power plant. Phillips applied a mathematical model of sustainability to the results of Turney and Fthenakis (Turney & Fthenakis, 2011); results indicated that installation and operation phases of utility-scale PV solar plants could be considered as sustainable at a strong level (Phillips, 2013). Klein and Rubin indicated life-cycle greenhouse gas emissions of using thermal energy storage is 4-9 times less than using a natural gas-fired energy backup system at a concentrating solar power (CSP) technology plant (Klein & Rubin, 2013). To sum up, environmental and human effects of USSEs, both for PV and CSP installations, depended on the size and nature of the project, were relatively small compared to other energy systems, especially coal power.

Comparison of environmental effects of solar energy and conventional energy resources indicates solar energy is more environmentally friendly in case of sustainability, emissions, and

land-use intensity. However, similar to conventional power plants, USSE plants cause disturbance during construction, development, and maintenance phases. In addition, USSE plants change energy balance and albedo and these can be a source of impacts on land cover and temperature in the region, and need to be assessed.

2.3 Life-Cycle Assessment of PV Cells

The majority of the studies on environmental impacts of solar plants are focused on PV cells in the case of production, maintenance, emission and disposal (Tyagi, Rahim, Rahim, & Selvaraj, 2013). Many scientists used life-cycle assessment (LCA) in order to analyze environmental impacts of PV cells (Bernal-Agustín & Dufo-López, 2006; Jungbluth, 2005; Pacca, Sivaraman, & Keoleian, 2007; Parida, Iniyan, & Goic, 2011; Zhang, Lv, & Zhang, 2012). After LCA of PV cells in various stages including cell production, Jungbluth (Jungbluth, 2005) stated "PV have environmental disadvantages in comparison with other renewable technologies e.g., wind and hydro power". However, in the LCA of the operational phase of PV cells, the impacts of PV panels on the environment including impacts on land surface temperature, shading on the ground, and changing spatial rainfall distribution in the area should to be considered.

2.4 Impacts on Land-Use and Land Cover

Regarding the impacts on land-use and land cover, Ong et al. (Ong, Campbell, Denholm, Margolis, & Heath, 2013) reviewed the land-use requirements for solar energy plants in the entire United States. Denholm and Margolis (Denholm & Margolis, 2008) estimated the total footprint needed for PV plants in each state in the United States. In a study on the positive and negative effects of USSE development on biodiversity, soils, water resources, and human health, Hernandez et al. (R. R. Hernandez et al., 2014) showed that potential effects on the land cover by USSE plants

are relatively small compared to other energy systems. Horner and Clark (Horner & Clark, 2013) used a harmonization process to provide a standard method to calculate solar land-use energy intensity. Murphy et al. (Murphy, Horner, & Clark, 2015) showed the off-site land-use energy intensity is less than 1% of the on-site land-use for PV and CSP technology. Results of research by Hernandez et al. (Rebecca R. Hernandez, Hoffacker, & Field, 2014) on land-use efficiency of USSE installations in California indicated that PV installations were in greater abundance than CSP installations; however, the type of technology used had no effects on land-use efficiency. De Marco et al. (De Marco et al., 2014) identified suitable areas for USSE with respect to the analysis of the legislation. Hernandez et al. (Rebecca R. Hernandez, Hoffacker, & Field, 2015) examined land, energy and environmental compatibility for PV and CSP technology in California and they identified diverse sites for small and utility-scale solar energy that could meet the state energy demand three to five times over.

USSE plants have an effect on fragmentation of the countryside as well. This effect, in the case of an installation on the ground, refers to the potential loss of the identity elements typical of the region (e.g., cultivability). According to Chiabrando et al. (Chiabrando et al., 2009), "…fragmentation is often seen as a negative factor and is opposed to nature conservation, as it is in the case of natural areas, since it causes a decrease of the biodiversity." Beylot et al. (Beylot et al., 2014) found that dual-axis trackers have more of an effect on ecosystem quality than other types, and this was influenced mainly by land occupation. In fact, they found that power plants with dual-axis trackers needed more space between each element of the PV field because that would provide wider shade than fixed and single-axis trackers.

The above-mentioned studies have focused more on land-use requirements, land fragmentation, and the potential impacts caused by changing land-cover type to install solar panels inside the plants footprint. All such studies heavily depend on measurements of the pre- and post-condition of land cover especially for synoptic view of inside and outside the facility. It is because the impacts of USSE plants may not be restricted to the inside of plant area and the impacts could manifest outside of the plant's footprint. Therefore, more studies are needed to measure the change in land cover between pre- and post-installation of solar plants. In addition, the relationship between distance and potential impacts on land cover need to be evaluated for the outside plant areas.

2.5 Thermal Impacts

PV solar farms may have thermal impacts on the environment because the surface albedo, which relates to reflectivity and absorbance rate, will be changed in the region (R. R. Hernandez et al., 2014). Taha evaluated the potential effects on air temperature by development of PV panels and consequent change in albedo (Taha, 2013). The results showed the temperature will cool down up to 0.2˚C in urban environment. Masson et al. concluded solar panels on the rooftops are able to reduce urban heat island effects (Masson, Bonhomme, Salagnac, Briottet, & Lemonsu, 2014). With PV systems, this happens due to the temperature that is reached by the PV panels during operation as a result of heating caused by sunlight. Barron-Gafford et al. studied PV heat island effect by temperature measurements at three different points (Barron-Gafford et al., 2016). They found temperatures over a PV plant in wildland were 3 to 4˚C warmer than outside areas at night. However, the difference between temperatures inside PV installation and outside were negligible in daytime.

Moreover, USSE plants occupy many square kilometers of desert area, thus affecting the thermal balance, which, according to Gunerhan et al. (Gunerhan, Hepbasli, & Giresunlu, 2008), "may destroy some species living in this kind of harsh environment." This effect could play a big part in choosing the type and location of a solar power plant. The temperature of the panels can increase up to 70°C in some areas, which can cause changes by heating the air surrounding the plant. Fthenakis and Yu showed the average temperature inside solar plants at height of 2.5 meters increased by 1.9 ˚C using computational fluid dynamics simulation (Fthenakis & Yu, 2013). Armstrong et al. studied the effects of solar energy generation technologies on microclimatic changes and consequently on ecosystem carbon cycling and greenhouse gas emissions (Armstrong, Waldron, Whitaker, & Ostle, 2014). In 2014, Qian studied the impact of land-use and land-cover change as a factor of changing in the regional surface energy balance on changes in surface solar radiation (Qian, 2014). They reported the reduction in surface solar radiation at most stations due to land-use and land-cover change.

Clearly, only a few studies on thermal impacts of USSE plants have been conducted. However, the reported results are inconsistent and need further investigation. Although the air temperature at various heights are available at some sites, surface temperature measurements at solar farms before and after installation are not available. Furthermore, surface temperature is expected to have dependence on shadowing of solar panels which has not been investigated in the literature. Therefore, the impacts of USSE plants on land surface temperature for inside the plants, considering the panels shading need to be understood. Furthermore, the impacts on land surface temperature for outside the plants and its relationship with distance need to be studied.

2.6 Hydrological Impacts

Solar plant construction impacts on hydrology of the region by changing slope, changing land surface characteristics and rainfall distribution. Cook and McCuen studied the hydrological effects of PV solar farms for pre- and post-installation on volumes and peak discharge (Cook & McCuen, 2013). They studied the effect of panel installation and land-cover type inside the facility on hydrograph.

Although hydrological assessment is necessary for each USSE project, changing in spatial rainfall distribution inside the plants are generally neglected in hydrological assessment reports. In addition, there is a need for more studies on different types of solar plants. Because depending on the location and technology, tilt angle and orientation of solar panels may differ. Thus, more studies are needed to provide a better insight about hydrological response of USSE plants, and the possible changes that after the installation of panels occurs.

2.7 Remote Sensing Techniques

Remote sensing refers to the processes of collecting information about Earth surfaces without physical contact between the surfaces of interest and sensor. Remote sensing data have been widely used for environmental assessment in recent decades because remote sensing data covers large geographic areas with high temporal frequency. Remote sensing generally refers to aerial photos and satellite imagery and many remote sensing applications have been developed to assess changes in land cover, land-use, land surface temperature, and also potential areas for solar plant installation. Mahtta et al. mapped potential areas for solar plant installation (CSP and PV) using remote sensing techniques considering land slope and solar radiation in India (Mahtta, Joshi, & Jindal, 2014). Calvert et al. reviewed the status of the application of geographic information

science and remote sensing techniques to decrease the uncertainties about renewable energy development (Calvert, Pearce, & Mabee, 2013).

2.7.1 Trend Analysis

Since remote sensing data provide consistent and repeatable measurements, they are suitable for capturing the effects caused by natural and anthropogenic disturbances. To do so, many studies have been done on trend analysis using remote sensing data (Fensholt, Rasmussen, Nielsen, & Mbow, 2009; Tottrup & Rasmussen, 2004; Verbesselt, Hyndman, Newnham, & Culvenor, 2010). Trend analysis is used to identify if an upward or downward trend is significant, such as the Mann-Kendal test (de Jong, de Bruin, de Wit, Schaepman, & Dent, 2011; Kendall, 1955; Mann, 1945; Neeti & Eastman, 2011).

Mann-Kendall test: The non-parametric Mann-Kendall test is a monotonic trend test of the variable of interest over time to identify if an upward or downward trend is significant (Kendall, 1955; Mann, 1945). The null hypothesis, H_0, is that the data do not follow a monotonic trend. The Mann-Kendall test can be calculated as follows (Neeti & Eastman, 2011),

$$S = \sum_{k=1}^{n-1} \sum_{j=k+1}^{n} sgn(X_j - X_k) \tag{2.1}$$

with

$$sgn(x) = \begin{cases} 1 & if \quad x > 0 \\ 0 & if \quad x = 0 \\ -1 & if \quad x < 0 \end{cases} \tag{2.2}$$

When n ≥ 8, the distribution of *S* is approximately normal, and the variance of *S* can be computed as follows,

$$\sigma^2 = \frac{n(n-1)(2n+5) - \sum_{m=1}^{p} t_m(t_m-1)(2t_m+5)}{18} \quad (2.3)$$

where p is the number of tied groups in the data set and t_m is the number of tied data in m^{th} tied group. The statistic S is then standardized (Z), and its significance can be estimated from the normal cumulative distribution function,

$$Z = \begin{cases} \frac{S-1}{\sigma} & if \quad S > 0 \\ 0 & if \quad S = 0. \\ \frac{S+1}{\sigma} & if \quad S < 0 \end{cases} \quad (2.4)$$

2.7.2 Land Surface Temperature Data

Remote sensing data and specifically thermal bands have been widely used to determine land surface temperature (LST) based on land surface emissivity (Jimenez-Munoz, Sobrino, Skokovic, Mattar, & Cristobal, 2014; Li et al., 2013; J. A. Sobrino, Raissouni, & Li, 2001; José A. Sobrino et al., 2008; José A. Sobrino, Jiménez-Muñoz, & Paolini, 2004; Yu, Guo, & Wu, 2014). According to Weng (Q Weng, 2009), the majority of the previous studies have been focused on the relationship between LST and surface characteristics, vegetation indices, land-use and land cover (Quattrochi & Luvall, 1997; Q. Weng, 2001). In addition, remote sensing is widely used to observe urban heat island effect through the combination of thermal remote sensing and urban micrometeorology (Voogt & Oke, 2003; Q Weng, 2003; Qihao Weng, Lu, & Schubring, 2004). Some of remote sensing thermal infrared sensors are: NOAA AVHRR, NOAA GOES, MODIS, Landsat TM 4 and 5, Landsat 7 ETM, Landsat 8 TIRS.

Remote sensing provides brightness temperature (T_B) which is defined as the temperature necessary for a black body to emit energy at the same rate as that observed from a given target

(Artis & Carnahan, 1982). The top-of-atmosphere (TOA) or at-sensor T_B can be converted from spectral radiance of thermal bands (e.g., Band 6 of Landsat 5 TM and Band 10 and 11 of Landsat 8 TIRS) using the following equation (Chander, Markham, & Helder, 2009),

$$T_B = \frac{K_2}{\ln(\frac{K_1}{L_\lambda} + 1)} \tag{2.5}$$

where T_B is the brightness temperature, K_1 and K_2 are calibration constants, and L_λ is spectral radiance at the sensor's aperture. The T_B can be related to physical temperature using Plank's radiation equation of black and gray bodies. According to Planck's equation, the rate at which a black body surface radiates energy is related to brightness temperature through the relationship,

$$L_{BB}(T_B, \lambda) = \frac{\beta}{\lambda^5 \left(e^{a/\lambda T_B} - 1\right)} \tag{2.6}$$

where L_{BB} is the spectral radiance of a black body, a and β are constants, and λ is the wavelength of the emitted radiance. Likewise, equation (2.6) can be rewritten for a gray body as,

$$L_{GB}(T, \lambda) = \frac{\varepsilon\beta}{\lambda^5 (e^{a/\lambda T} - 1)} \tag{2.7}$$

where L_{GB} is the spectral radiance of a gray body and T is kinematic (physical) temperature of the object. The ε is emissivity defined as the ratio of the radiance emitted by a gray body and the radiance emitted by a black body, at the same temperature and at a given wavelength (Li et al., 2013). Emissivity appears in Stefan–Boltzmann law and it is an intrinsic property of a material which varies with wavelength, temperature, viewing angle and surface roughness (Li et al., 2013; J. A. Sobrino et al., 2001; José A. Sobrino, Jiménez-Muñoz, & Verhoef, 2005). Artis and Carnahan

(Artis & Carnahan, 1982) has equated equations (2.6) and (2.7) to relate brightness temperature and kinetic temperature as,

$$T = \frac{T_B}{1 + (\frac{\lambda T_B}{\alpha})ln\varepsilon} \quad and \quad T_B = \frac{T}{1 - (\frac{\lambda T}{\alpha})ln\varepsilon}. \tag{2.8}$$

According to this relationship, surface temperature of an object can be calculated given the emissivity and brightness temperature. It is noted that λ is the midpoint of the band's wavelength range (e.g., for Landsat 5 TM $\lambda = 11.45\,\mu m$, and for Landsat 8 TIRS $\lambda = 10.9\,\mu m$) (Di Leo, Escobedo, & Dubbeling, 2016; Qihao Weng et al., 2004).

2.7.3 Land Surface Emissivity

In order to calculate T, ε is required. Various methods have been proposed to estimate ε which can be categorized in three groups; semi-empirical methods, multi-channel temperature/emissivity separation methods, and physical based methods (Li et al., 2013). One of the most popular methods that has shown high accuracy in band covering range 8-14 µm, is a semi-empirical method called NDVI-based emissivity method (Owe & Vandegriend, 1993). Based on NDVI value of the pixel, different relationships are proposed to calculate ε; for NDVI<0.2, 0.2≤NDVI≤0.5 and NDVI≥0.5. According to Sobrino et al. (José A. Sobrino et al., 2004), in an arid area, when NDVI<0.2, ε has a linear relationship with reflectivity value in the red region,

$$\varepsilon = b\rho_{red} + c \tag{2.9}$$

where b and c are constants derived from regression analysis. For example, the relationship that is obtained for Landsat 5 TM band 6 (the obtained root mean square below 0.01) is (José A. Sobrino et al., 2008),

$$\varepsilon = 0.979 - 0.035\rho_{red} \quad (2.10)$$

and the relationship that is obtained for Landsat 8 TIRS band 10 (the obtained root mean square ~1 K) is (Yu et al., 2014),

$$\varepsilon = 0.973 - 0.047\rho_{red}. \quad (2.11)$$

2.7.4 Land-Cover Analysis

Remote sensing is a valuable tool for land-cover analysis studies. Chen et al. provided a statistical example on vegetation estimation, based on multivariate statistical modeling and using remote sensing data (Chen, Sakai, Moriya, Koyama, & Cao, 2013). They selected the reflectance of data from four bands of a Huan Jing (HJ-1) charged-coupled device, six vegetation indexes, three principal components from principal component analysis (PCA), and three variables from tasseled-cap transformation to correlate with measured vegetation coverage. According to the results, this method had relatively high precision with environments having various densities of vegetation.

When classifying multi-spectral images, each pixel often contains a mixture of land-cover categories. One useful technique for estimating the proportion of each pixel that is covered by a series of known cover types is by spectral mixture analysis (SMA). Lu and Weng applied an SMA approach to solve the mixture problem with low-resolution data, and provided better classification results than traditional maximum-likelihood classifiers (Lu & Weng, 2004). To estimate impervious surfaces, Wang et al. compared the performance of four methods by using linear SMA for spectral-data treatment in the central area of Shanghai, China (Wang, Yao, Ji, & Zhang, 2014). Regarding endmember extraction for SMA, Mei et al. proposed an algorithm to integrate spectral

similarities and spatial context (Mei, He, Wang, & Feng, 2010). Similarly, Plaza et al. presented an automated method for unsupervised determination of pixel purity from multi-dimensional datasets (Plaza, Martinez, Perez, & Plaza, 2002). Song used Bayesian SMA to determine the effects of endmember variability on the estimation of sub-pixel vegetation fractions (Song, 2005).

2.7.5 Spectral Mixture Analysis

This technique seeks to determine the likely composition of constituent land-cover types or endmembers to produce the measured pixel value,

$$b^i = f_1^i.\rho_1^i + f_2^i.\rho_2^i + \cdots + f_N^i.\rho_N^i + e, \tag{2.12}$$

where b^i is measured i^{th} band spectral radiance of a pixel with N endmembers. The ρ^i and f^i are spectral reflectance and subpixel aerial fraction of an endmember, respectively; and e is the residual error. Such relationships for an imagery with K bands result in a system of equations that can be written in matrix form as

$$\mathbf{b} = \bar{\bar{\boldsymbol{\rho}}}\boldsymbol{f} + \boldsymbol{e} \tag{2.13}$$

where $\bar{\bar{\boldsymbol{\rho}}}$ is a K by N matrix with rows corresponding to K bands and columns corresponding to N endmembers. The symbols $\boldsymbol{f}$ and $\boldsymbol{e}$ are column vectors of subpixel aerial fraction of endmembers and the residual errors, respectively. The SMA approach poses two conditions on the subpixel land-cover fractions given by:

$$\sum_{n=1}^{N} f_n = 1 \tag{2.14}$$

and

$$0 \leq f_n \leq 1 \, , n = 1, 2, \dots , N. \quad (2.15)$$

This review indicated that remote sensing is a valuable tool for environmental impact assessment. Due to the large geographic coverage and high temporal frequency, remote sensing is an appropriate method for change detection and trend analysis. Remote sensing is capable of providing land cover and land surface temperature information, and is suitable to be applied in USSE plants environmental studies.

2.8 Summary

According to previous studies, many scientists have worked on understanding the environmental impacts of solar energy plants. However, there are gaps in the current knowledge that need to be addressed. The above review clearly identifies that the impacts of USSE plants on land cover are not well understood. Previous studies regarding impacts on land cover have focused more on the potential impacts caused by changing land-cover type to install solar panels inside the plants footprint. In other words, no one has measured and tracked pre- and post-condition of land cover due to solar plants construction. Therefore, there is a lack of measurement for the impacts of USSE plants either inside or outside of the plants area, especially to determine the relationship between distance and land-cover impacts. Additionally, the few studies on thermal impacts of solar energy and changes in albedo have been conducted, with inconsistency in the reported results. The impacts of USSE plants on land surface temperature considering shading of panels are not well understood. The review of previous studies revealed that more studies regarding hydrological impacts of USSE plants need to be conducted. Solar panels can cause changes in spatial rainfall distribution inside the plants which is generally neglected in hydrological assessment reports. In addition, slope and orientation of solar panels differ depending on the location and technology,

e.g. fixed-tilt, single axis tracking. During a storm, lack of understanding of the hydrological impacts resulting from rainfall distribution alteration may cause significant difference between expected and actual produced runoff. In this study, in order to enhance environmental sustainability of USSE plants, I have used remote sensing to answer three questions that are not answered in the literature;

- What is the impact of USSE plants on land cover inside and outside of the plants?
- What is the impact of USSE plants on land surface temperature inside and outside of the plants?
- What is the impact of USSE plants on hydrological response in the region?

In the following sections, each question is addressed in a separate chapter.

Manuscript Information Page

The following chapter has been published as a peer-reviewed article in Renewable and Sustainable Energy Reviews journal, volume 67, pages 1139-1152, 2017. Copyright information can be found in Appendix or at the Elsevier web site;

(https://www.elsevier.com/about/our-business/policies/copyright)

3. CHAPTER 3- EFFECT OF UTILITY-SCALE SOLAR ENERGY PLANTS ON LAND COVER

3.1 Introduction

Understanding the impacts of USSE plants on land cover is important. These impacts can alter regional climate, ecosystem and hydrological behavior in an area. In the construction and development phases, land surface characteristics change due to land preparation, grading, transportation, and panel installation processes. In addition, in the operation phase, panels' temperature can cause thermal effects in the region, which is a potential factor that can impact land cover. Land-cover change influences climate and ecosystem (Lambin & Geist, 2006). Furthermore, land-cover change can have an impact on regional climate by modifying albedo of the land surface and therefore, surface-atmosphere energy exchange (Charney, Stone, & Quirk, 1975; Otterman, 1974). Albedo is an important concept in climatology because it directly impacts the absorbed solar radiation and can alter energy balance in a region. It can change evapotranspiration subsequently modifying water cycle and precipitation (Eltahir, 1996). Some of the other impacts of land-cover change include impacts on biodiversity losses, soil degradation, atmospheric chemistry, nutrient cycling, infiltration rate, groundwater level and hydrology of the region.

3.2 Research Approach

This objective aims to study the effects of USSE facilities on land cover in desert areas. Trends were analyzed by measuring changes in the land-cover fractions inside and around USSE facilities using remote sensing. A time series of Landsat 5 Thematic Mapping (TM) images are used with principal component analysis (PCA), minimum noise fraction (MNF), and spectral

mixture analysis (SMA) to estimate the subpixel fraction of each pixel covered by a four-endmember model for land surface: high-albedo, low-albedo, shadow, and vegetation. The trends of these classes are compared between pre- and post-installation and thus effect of solar facility construction is determined.

3.3 Study Area

This study demonstrates a subpixel land-cover estimation approach while measuring land-cover change at two types of power plants. This study is conducted at two utility-scale solar energy (USSE) plants in Nevada, Nevada Solar One and the Nellis Solar Power Plant from 2004 to 2011. Nevada Solar One and Nellis Solar Power Plant are selected for this study because of their location and solar energy techniques; Nevada Solar One is located outside the urban area and Nellis Solar Power Plant is located inside an urban area. In addition, Nevada Solar One uses CSP techniques whereas Nellis Solar Power Plant uses PV techniques. The description of these plants is as follows.

Nevada Solar One (NS-1) is a concentrated solar power plant with a footprint of 1.62 km^2 in the Eldorado Valley near Boulder City, Nevada. The study is conducted over a rectangular area ~127 km^2 around the facility. It has been built within the City's Energy Resource Zone, which requires renewable generation as a part of plant development permits. This plant uses parabolic concentrators with mirrors to focus the sun’s energy onto oil-carrying receiver tubes. The heated oil is used to boil water into steam in order to drive a turbine power generator. This plant uses proprietary technology to track the sun’s location and to concentrate rays during peak demand hours. The solar plant provides mixed power, using 98% concentrated solar and 2% natural gas, with a nominal capacity of 64 megawatt (“Nevada Solar One,” n.d.). NS-1 construction began in February 2006, and operations started in June 2007.

Figure 3.1 compares two aerial images of NS-1 both during construction in 2006 (Figure 3.1a) and after completion in 2010 (Figure 3.1b). In Figure 3.1a, the land for the upper plant section was prepared for the construction in 2006. In Figure 3.1b, the solar panels were installed in the upper section and panels in the lower section were installed in 2010. In order to investigate changes in land-cover characteristics further, Points 1A and 2A are selected for further analysis and comparison using the proposed methods. Point 1A is located within the facility areas and Point 2A is located outside of the facility.

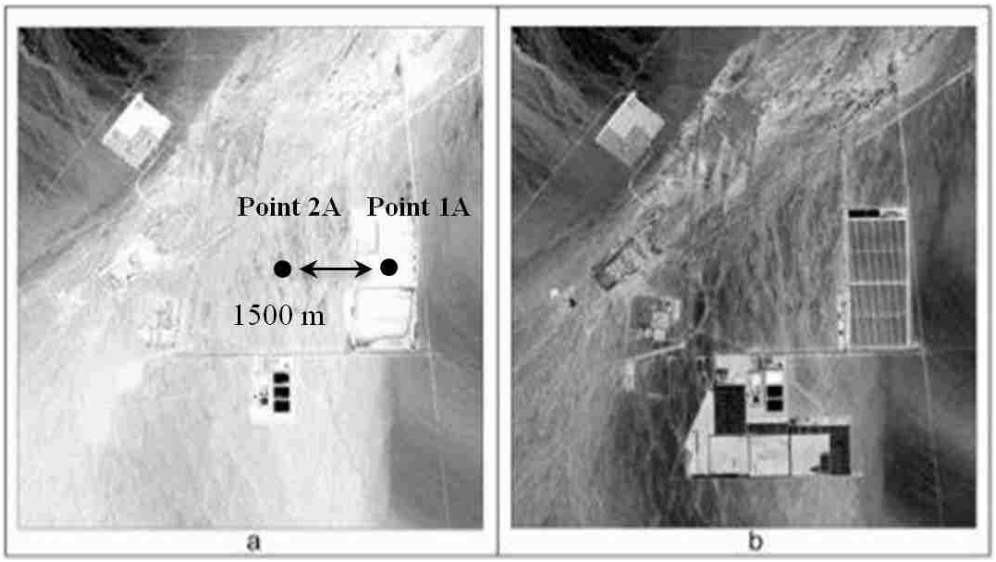

Figure 3.1 Nevada Solar One in a) 2006 and b) 2010

Nellis Solar Power Plant (NSPP), a photovoltaic power plant, spreads over 0.57 km^2 within Nellis Air Force Base located in northeast of Las Vegas in Clark County, Nevada. The effect on land cover is studied over a rectangular area ~7.76 km^2 around the facility. Its PV cells generate electrical power by converting sunlight into direct current electricity. The system contains

approximately 70,000 PV panels that employ an advanced single-axis sun-tracking system. NSPP generates more than 14 megawatt of electricity, and supplies more than 25% of the power at the Nellis Air Force Base ("Nellis Air Force Base - Nellis Solar Array," n.d.).

NSPP construction began in April 2007, and operations started in December 2007. Figure 3.2 compares two aerial images of NSPP, including before construction in 2006 and after completion in 2010. In Figure 3.2a, the land was prepared for construction in 2006. Figure 3.2b shows the solar panels completely installed by 2010. Similar to NS-1, in order to further investigate the changes in land-cover characteristics, Points 1B and 2B are selected for further analysis using the proposed methods. Point 1B is located within the facility area and Point 2B is located outside of the facility.

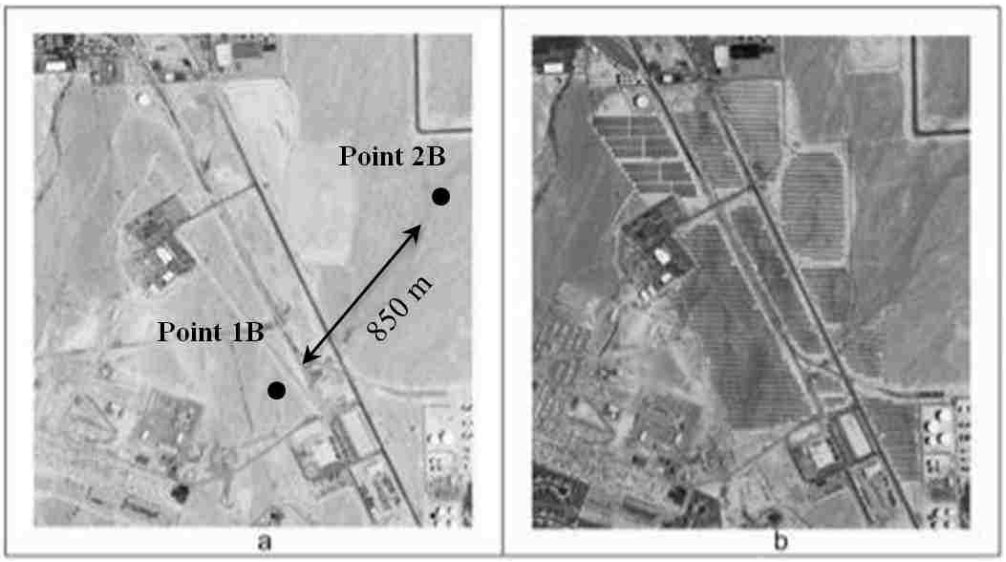

Figure 3.2 Nellis Solar Power Plant in a) 2006 and b) 2010

3.4 Remote Sensing Data

This research used aerial imagery from the Landsat 5 TM as well as from the National Agriculture Imagery Program (NAIP). TM imagery from Landsat 5 was used to estimate land-cover changes, and the higher resolution NAIP imagery was used to validate the results. These data are described below.

Landsat 5 Thematic Mapper: Landsat 5 is a low-earth-orbit satellite, recognized as the longest operating mission in history for an Earth-observing satellite. Its payload includes the thematic mapper instrument, which has orbited the planet more than 150,000 times and has transmitted over 2.5 million images. TM images consist of seven spectral bands, including visible, near-infrared, thermal, and mid-infrared bands. Bands 1, 2 and 3 are visible, Bands 4 and 5 are near-infrared, Band 6 is thermal, and Band 7 is mid-infrared. Available since 1984, this multi-channel data is used extensively to differentiate land-cover types and study trends (Jomaa, Auda, Saleh, Hamze, & Safi, 2008; Rogan, Franklin, & Roberts, 2002; Thomlinson, Bolstad, & Cohen, 1999). This data provides an opportunity to perform time-series analyses in order to understand the effects of large-scale solar power plants.

Both study sites are covered by Landsat TM Path 39 and Row 35. From March 2004 to February 2011, a total of 114 images were acquired from the USGS Earth Resource Observation Systems (EROS) Data Center (EDC). Standard TM data products are available as digital numbers (DN), which are converted to spectral radiance at the sensor's aperture. Recently, the U.S. Geological Survey (USGS) has released climate data records (CDR), which provides surface reflectance data of TM. Because this research began before the release of the CDR data, spectral radiance images were calculated from DN images. Spectral radiance images are analyzed visually

in order to isolate 76 cloud-free images appropriate for further processing. All bands had a spatial resolution of 30 m, except for thermal infrared, which was 120 m. However, thermal infrared was not used in this study.

Spectral radiance at the sensor's aperture is calculated using (Chander et al., 2009)

$$L_\lambda = \left(\frac{LMAX_\lambda - LMIN_\lambda}{Q_{calmax} - Q_{calmin}}\right)(Q_{cal} - Q_{calmin}) + LMIN_\lambda \quad (3.1)$$

where

L_λ = Spectral radiance at the sensor's aperture [W/ (m^2 sr μm)]

Q_{cal} = Quantized calibrated pixel value [DN]

Q_{calmin} = Minimum quantized calibrated pixel value corresponding to $LMIN_\lambda$ [DN]

Q_{calmax} = Maximum quantized calibrated pixel value corresponding to $LMAX_\lambda$ [DN]

$LMIN_\lambda$ = Spectral at-sensor radiance that is scaled to Q_{calmin} [W/ (m^2 sr μm)]

$LMAX_\lambda$ = Spectral at-sensor radiance that is scaled to Q_{calmax} [W/ (m^2 sr μm)].

The calculated spectral radiance images are used to estimate land-cover change. Pure pixels are selected from the same images for the SMA process, and are validated based on a high-resolution image of the study area. Through a normalization process, described in methodology section, spectral radiance images provide values identical to surface reflectance images currently provided by USGS.

Spectral radiance data can be converted to surface reflectance (ρ) data to reduce scene-to-scene variability. Chander et al. (Chander et al., 2009) provided an equation to convert the spectral radiance at the sensor's aperture to the top-of-atmosphere (TOA) reflectance of the Earth.

National Agriculture Imagery Program: The National Agriculture Imagery Program acquires aerial imagery during the agricultural growing seasons in the continental U.S. ("NAIP Imagery," n.d.), at 1-m resolution. The frequency bands that are available are natural colors – red, green, and blue (RGB). However, beginning in 2007, some states have been delivering four bands of data, RGB as well as near infrared. In this research, NAIP imagery acquired during May 2010 is used for verification of the results obtained using Landsat 5 TM. This imagery is obtained from the website for W.M. Keck Earth Science & Mining Research, from which data from 2006, 2009, 2010, and 2013 is available (http://keck.library.unr.edu/) ("Home: W.M. Keck Earth Sciences & Mining Research Information Center," n.d.).

3.5 Methods

The data processing primarily consists of three parts including 1) a data treatment step to reduce the bands number (known as dimensions) of the Landsat imagery, 2) data unmixing in order to retrieve information of sub-pixel land cover, and 3) trend analysis to estimate changes in the land cover. The data treatment is done to convert correlated TM bands into a set of linearly uncorrelated component bands. Two methods including principal component analysis and minimum noise fraction are applied. The dominant component bands are used to extract spectral signatures of land-cover types called endmembers. Spectral signatures of endmembers are used to retrieve subpixel land cover of mixels by means of a process of unmixing. Several techniques have

been developed, including linear spectral unmixing, fuzzy classification, and automatic subpixel detection. Spectral mixture analysis is used to retrieve subpixel land-cover fraction of each class.

Figure 3.3 shows the flowchart of these performed steps which are further described as follows.

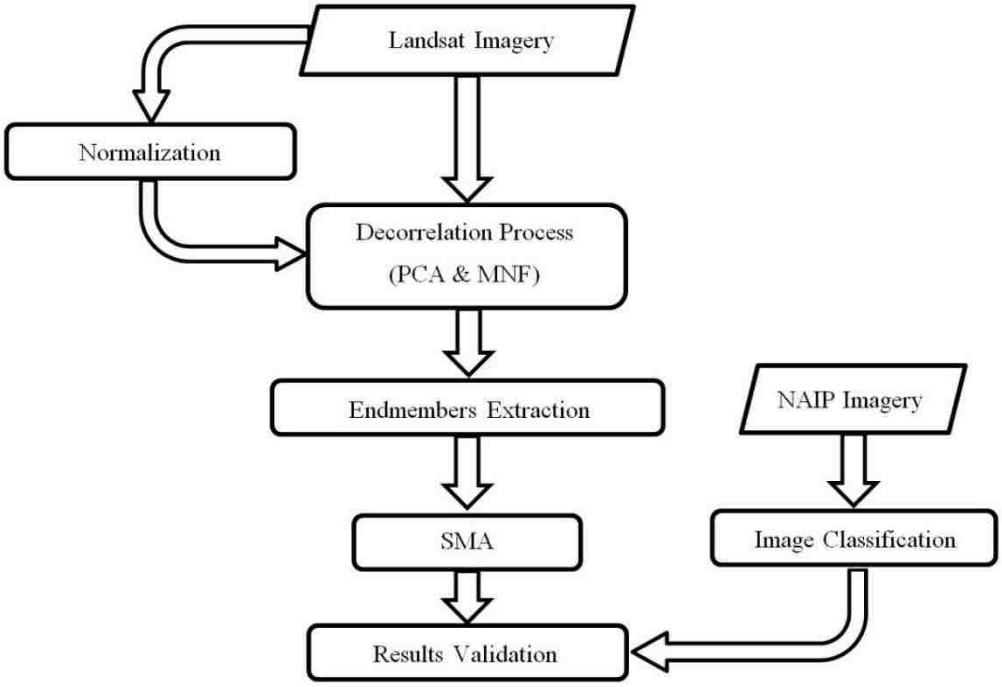

Figure 3.3 Flowchart of the methods used for data treatment of the Landsat 5 imagery

3.5.1 Data Treatment Techniques

Two methods are applied to treat TM images; principal component analysis (PCA) (P. E. Johnson, Smith, & Adams, 1985; R. A. Johnson & Wichern, 1992; Jolliffe, 2002) and minimum noise fraction (MNF) (Green, Berman, Switzer, & Graig, 1988). These methods basically involve a constrained rotation of data in a multi-dimensional space. In PCA, variance represents the

information, and the data rotation is performed such that variance is maximized along fewer dimensions. The data projections along these dimensions are called principal components. Similarly, the MNF rotates the data to achieve minimum noise along fewer dimensions. The data projections along these dimensions are called minimum noise components. Both PCA and MNF transform TM imagery such that the information of the transformed imagery is concentrated into fewer bands. These transforms are tested over arid regions to identify the most applicable methods for land-cover analysis of solar facilities. The transformation of TM imagery into fewer bands for most of the information can be used continuously in further analysis, such as for target identification, image classification, and subpixel retrieval. Often, pure pixels (containing a single land cover called an endmember) exhibit extreme values in these bands, whereas mixels (pixels containing multiple endmembers) exhibit intermediate values, depending on the level of mixing. Four endmembers are identified, including high-albedo (HA), low-albedo (LA), vegetation (VG), and shadow (SH). High-albedo represents land covers that reflect most of the light, such as concrete roofs and sand. Low-albedo is associated with land covers that absorb most of the light and appear relatively dark colored to the eyes, such as asphalt and water bodies.

The PCA and MNF transforms are used with both original data and normalized data. For original data, spectral radiance images are the input without any change; normalized data, on the other hand, is converted to get the zero mean (zero-centering) and the unit variance (normalization) for each band. The terms 'original' and 'normalized' are used to identify the results of these two input data variations. Both PCA and MNF transforms are implemented using MATLAB R2014a. However, the PCA function used in MATLAB does zero-centering but does not scale the data to unit variance (Jolliffe, 2002). MNF has the lowest noise fraction in the last component, whereas PCA has the largest variance in the first component. In this research, a TM cloud-free image,

acquired on July 18, 2007 is used to determine the spectral signatures of land-cover classes used with PCA and MNF techniques.

Table 3.1 lists the percentage of the total variance explained by each principal component in the PCA bands, and the noise fraction of each MNF band. The first three components of PCA-Original and PCA-Normalized covered 99.6% and 99.06% of the variance, respectively; the last three components of MNF-Original and MNF-Normalized carried 24.4% and 11.5% of the noise, respectively.

Table 3.1 PCA Band Variances and MNF Bands Noise Fractions

Band Number	PCA-Original		PCA-Normalized		MNF-Original	MNF-Normalized
	Total Variance (%)	Eigenvalues	Total Variance (%)	Eigenvalues	Noise Fraction	Noise Fraction
Band 1	94.3341	1444.5980	89.8667	5.3920	0.8271	0.1168
Band 2	4.1613	63.7245	7.4157	0.4449	0.2522	0.0798
Band 3	1.1043	16.9105	1.7782	0.1067	0.1891	0.0694
Band 4	0.2154	3.2986	0.5798	0.0348	0.1169	0.0434
Band 5	0.1796	2.7505	0.2406	0.0144	0.0828	0.0390
Band 6	0.0053	0.0814	0.1188	0.0071	0.0446	0.0326

As shown in Figure 3.4 and Figure 3.5, the PCA and MNF components were graphed as scatter plots to identify the endmembers corresponding to extreme corners (vertices) in these plots (Boardman, 1994; Plaza et al., 2002). Figure 3.4 shows the 2-D scatter plot of PCA-Original- and -Normalized datasets and Figure 3.5 shows the 2-D scatter plot for MNF-Original and -Normalized datasets. The types of the pixels at the extreme vertices in the scatter-plots are determined by linking the pixels back to the image-feature space.

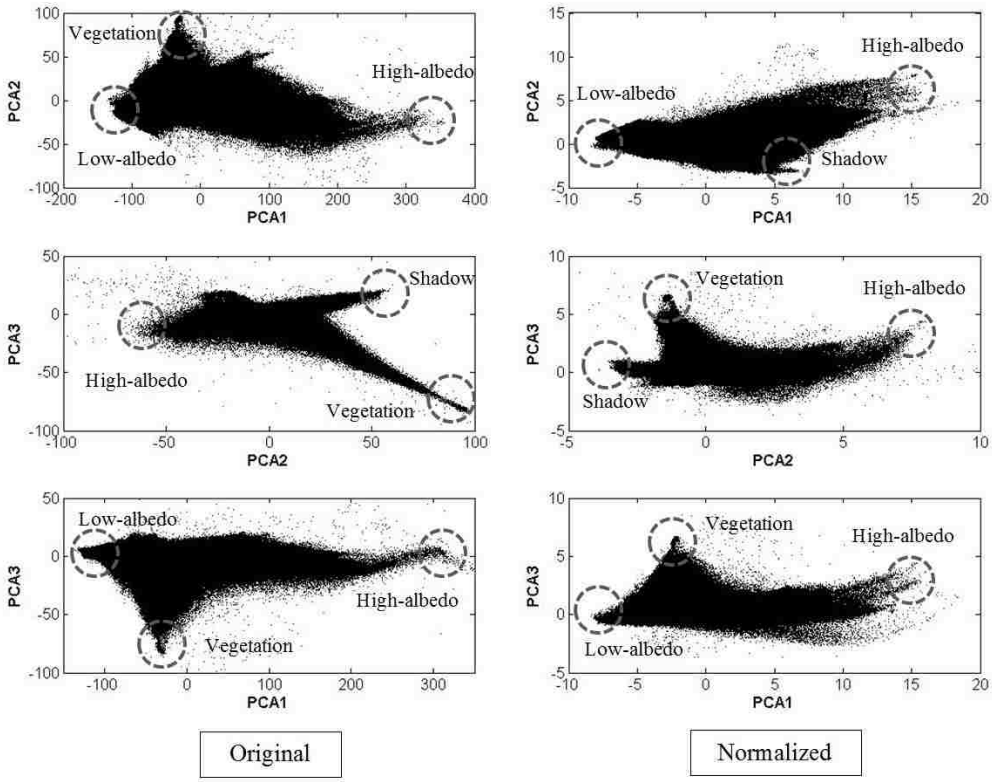

Figure 3.4 2-D scatterplot of the first three principal components of PCA (July 18, 2007)

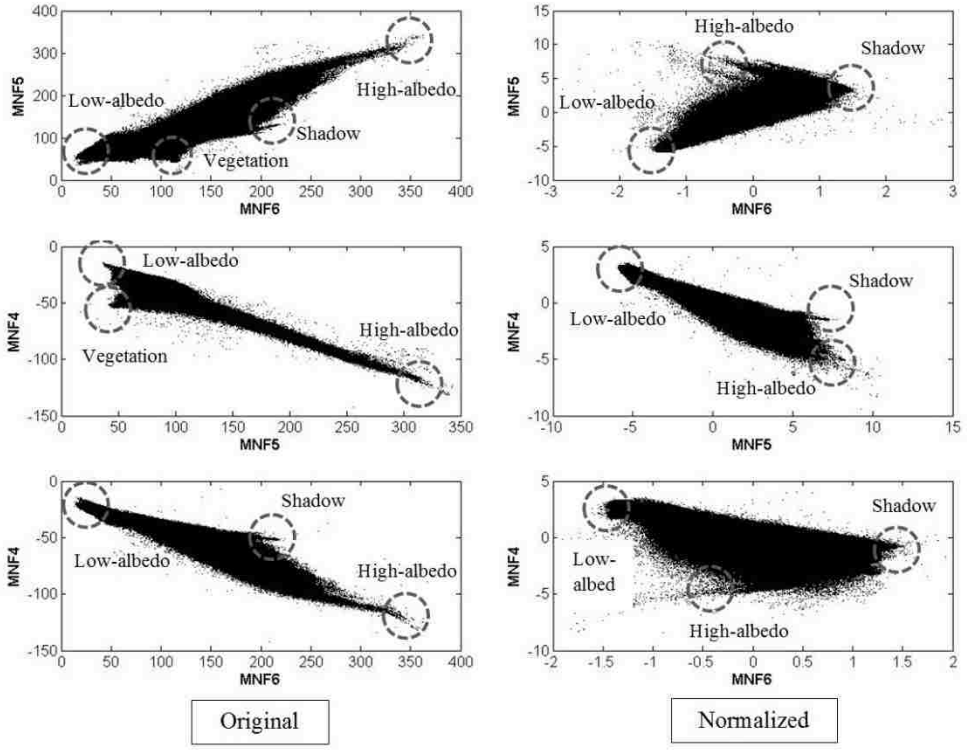

Figure 3.5 2-D scatterplot of the last three principal components of MNF (July 18, 2007)

For each endmember type, at least 20 representative pixels were selected. Thus, spectral signatures of HA, LA, VG, and SH land-cover types were extracted using four variations of data treatment, including PCA-Original, PCA-Normalized, MNF-Original, and MNF-Normalized.

3.5.2 Spectral Mixture Analysis

Spectral mixture analysis (SMA) is used to retrieve subpixel land-cover fraction of each class. Often, a pixel contains a mixture of land-cover categories. In fact, the number of pure pixels that contain only one feature or class is small. Nevertheless, the value of a pixel with a mixed land cover depends on the ensemble of responses for each constituent land cover. SMA has been extensively employed for land-cover mapping using TM data (Elmore, Mustard, Manning, & Lobell, 2000; Song, 2005; Wu & Murray, 2003). Equations (1.13), (1.14), and (1.15) are solved for each cell to estimate fractions such that residual error *e* is minimized (Canty, 2010). The Nedler-Mead method (available in MATLAB 2014a), is used to minimize the residual, is a multidimensional, unconstrained, nonlinear minimization for finding the minimum of a scalar function of several variables (Lagarias, Reeds, Wright, & Wright, 1998).

Validation of the land-cover fractions produced by SMA is necessary to establish quality of the output. Therefore, the SMA results are compared with land cover based on high-resolution NAIP imagery. Subpixel fractions are retrieved for a TM image acquired on May 10, 2010, and compared to classification of a NAIP image acquired on May 7, 2010. The comparison is made over a randomly selected rectangular area within the City of Las Vegas. The NAIP image is classified using a supervised image-classification tool in ArcGIS 10.2.2 for the same four endmembers used in SMA. Pixels representing the endmembers are manually selected for the image-classification process. Additionally, land-cover fractions of all TM image pixels are

calculated using SMA. As mentioned earlier, NAIP imagery has a 1-m resolution and TM images have a 30-m resolution. Thus, pixels of each TM image included 900 NAIP pixels. Therefore, two land-cover datasets are calculated for the land-cover fractions of the TM images and the NAIP imagery. In order to compare TM image results with NAIP imagery results, four types of data are used as input for the SMA process: PCA-Original, PCA-Normalized, MNF-Original, and MNF-Normalized. The correlation coefficient is calculated to determine the relationship between image classification and SMA results.

3.5.3 Trend Analysis

Trend analysis is performed on the time series of land-cover fractions retrieved from SMA and data treatment. In order to analyze the effects of the construction of USSE plants on land-cover patterns, time-series data are classified as pre-, syn-, and post-installation data. The average land-cover fraction of each land-cover type is calculated for pre- and post-installation. Due to the abrupt change in endmember fractions in some areas after USSE plant construction, the averaging method is used to identify the change between before and after construction.

3.6 Results and Discussion

In this section, the results of subpixel land-cover estimation and their temporal analysis with respect to solar installations are presented. First, a brief comparison of four data treatments is discussed to identify a suitable treatment for selecting endmembers and applying SMA. Second, the fractional area maps of four endmembers produced by SMA are presented and discussed at the two study sites. Finally, the pre- and post-installation fractional area maps are compared to estimate the effects of solar facilities on land-cover patterns.

3.6.1 Comparisons of Data Treatment Techniques

In order to identify a suitable treatment for selecting endmembers, the SMA results are validated using NAIP imagery acquired on May 7, 2010. To do so, a random rectangular area is selected within the City of Las Vegas. Figure 3.6a displays the area on which the validation process is applied. The image in Figure 3.6b is obtained from the image classification process for the four showing classes (in the legend), which are manually determined. Commercial building roofs and high-reflectance soils are classified as high-albedo, and roads and water bodies are classified as low-albedo. Shadow is mainly represented by the shadows of large buildings. As shown in Figure 3.6b, SMA is applied on the closest available Landsat imagery, acquired on May 10, 2010, is classified in the same area on the first four bands of PCA and the last four bands of MNF, based on the four endmember types obtained from Figure 3.4 and Figure 3.5.

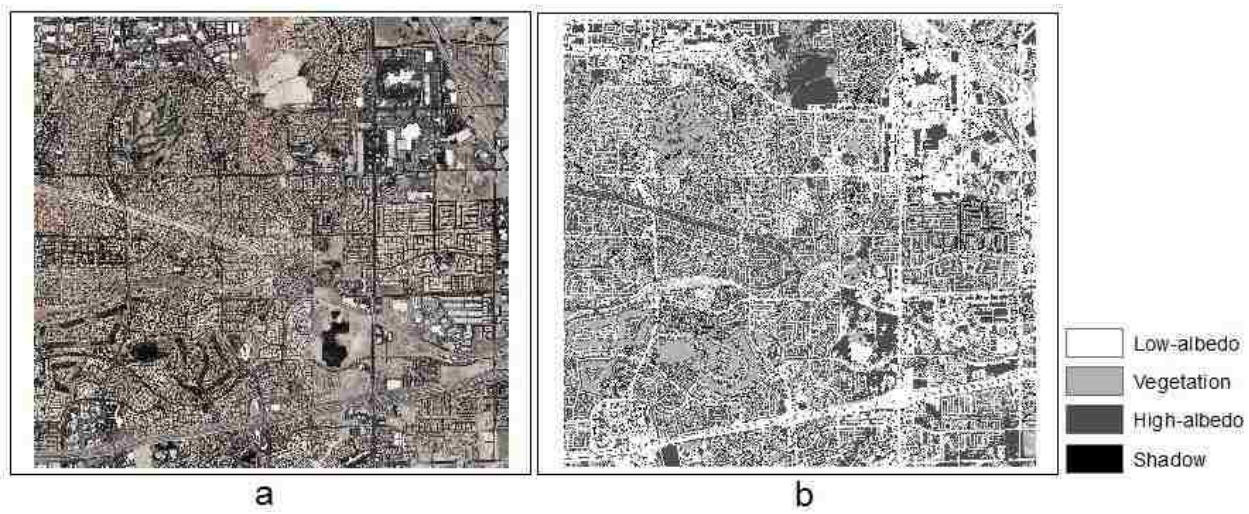

Figure 3.6 a) NAIP imagery (7 May 2010) of a random area in the City of Las Vegas b) Classified image

Figure 3.7 shows the relationship between the estimated fractions of each endmember by SMA and NAIP imagery classifications. According to Figure 3.7, high-albedo and low-albedo can be estimated with higher correlation coefficients (r) by PCA-Normalized (r = 0.62 and r = 0.72). In addition, MNF- Original shows the highest correlation coefficient for vegetation (r = 0.81). The calculated fractions for shadow have low-correlation coefficients. The possible reason might be that a shadow moves along the ground throughout the day, and the NAIP imagery and the Landsat images were not taken at the same time of day, therefore, the fraction of shadow in the NAIP imagery differs from that of the Landsat images.

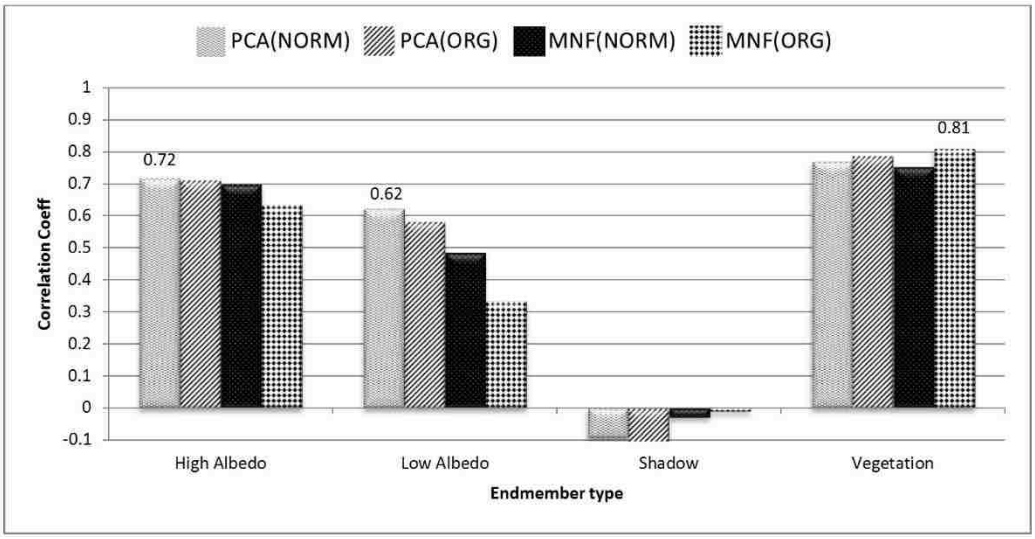

Figure 3.7 Relationship between the estimated fractions of each endmember by NAIP imagery classification and applied methods (7 May 2010)

Figure 3.8 shows component-based signatures of endmembers for PCA-Normalized and MNF-Original. The first band of PCA (PCA1) and the last band of MNF (MNF6) clearly represent the endmembers. In contrast, endmember values of PCA's last band (PCA4) and MNF's first band (MNF3) are in the lower range and are relatively hard to recognize.

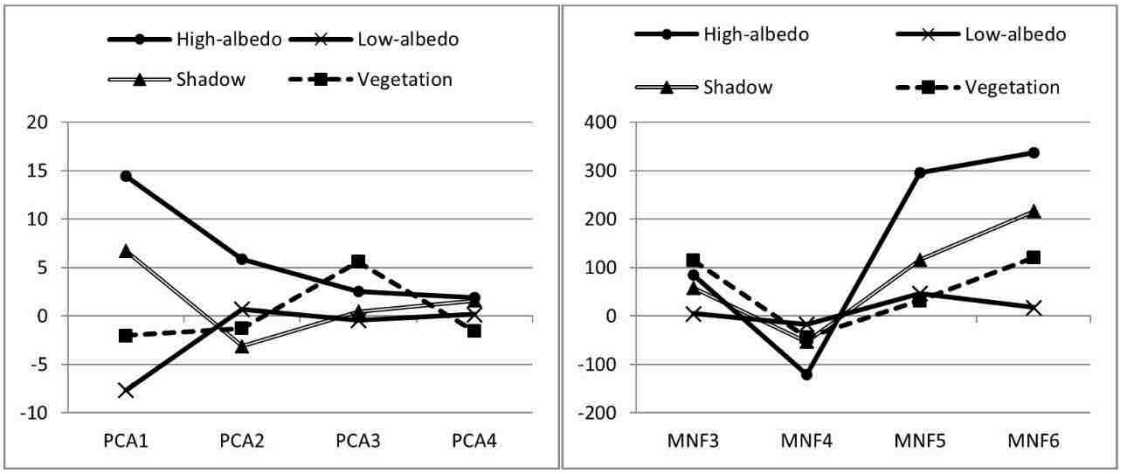

Figure 3.8 Reflectance characteristics of the endmembers for PCA-Normalized and MNF-Original (7 May 2010)

3.6.2 Trend Analysis

According to the correlation coefficients obtained in Figure 3.7, PCA-Normalized and MNF-Original datasets are selected as the data preparation methods used to apply SMA on Landsat 5 TM images from 2004 to 2011. SMA is applied to 76 cloud-free PCA-Normalized and MNF-Original images (Landsat 5 TM). The calculation process is pixel by pixel, and the result of each pixel is independent of the other pixel results.

The mathematical process is applied to satisfy equation (1.13) with the constraint equations (1.14) and (1.15). Accordingly, the summation of the endmember fractions in each pixel must be equal to 1; however, the results showed some errors for certain pixels. One way to determine errors is to find the summation of the four fractions and set the acceptable range as high and low limits for the data. As a result, 1.1 and 0.9 are assumed as the high and low limits, respectively. An unreliable pixel is defined as a pixel with a summation either less than 0.9 or greater than 1.1. Therefore, the ratio of number of unreliable pixels to all pixels is calculated for the two solar plants.

Figure 3.9 shows the percent of error in each area for the two datasets. According to Figure 3.9, the calculated results by PCA-Normalized had less error percentage to compare with MNF-Original. The average percentage error for PCA-Normalized results at Nevada Solar One and the Nellis Solar Power Plant area are 3.09% and 6.81%, respectively; the average percentage error for MNF-Original results are 29.09% and 32.86%, respectively. A possible reason for the lower errors in Nevada Solar One is that this facility is located out of town, and so the pixels were not filled by complicated and mixed endmembers. The Nellis Solar Power Plant is located within an urban area; therefore, pixel structures are more complicated than in the desert. Further, the results of SMA on PCA-Normalized have a higher number of errors during winter and summer and a lower number of errors in fall and spring; in contrast, the error plot of MNF-Original do not have a specific pattern. Consequently, SMA on PCA-Normalized resulted in the highest accuracy.

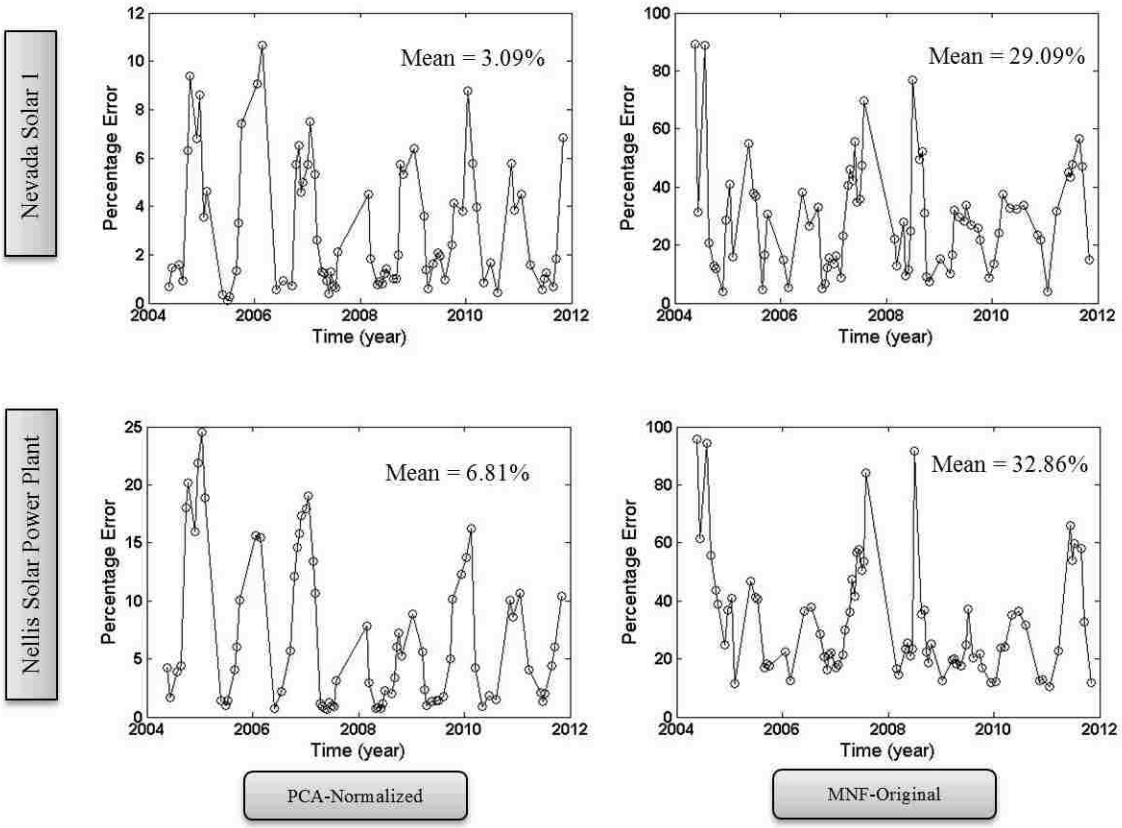

Figure 3.9 Percentage of error in calculated land-cover fractions from 2004 to 2011

The time series of endmember changes, obtained from SMA on PCA-Normalized, are plotted for Points 1A and 1B within the two facilities areas (Figure 3.10 and Figure 3.12), and Points 2A and 2B for outside of the facilities (Figure 3.11 and Figure 3.13).

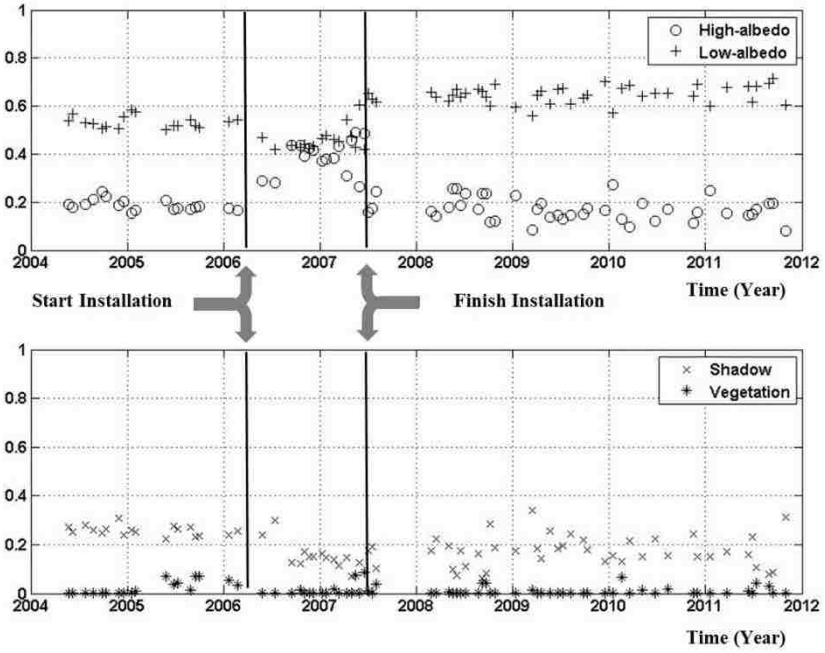

Figure 3.10 Time series of land-cover types at Point 1A, located inside Nevada Solar One

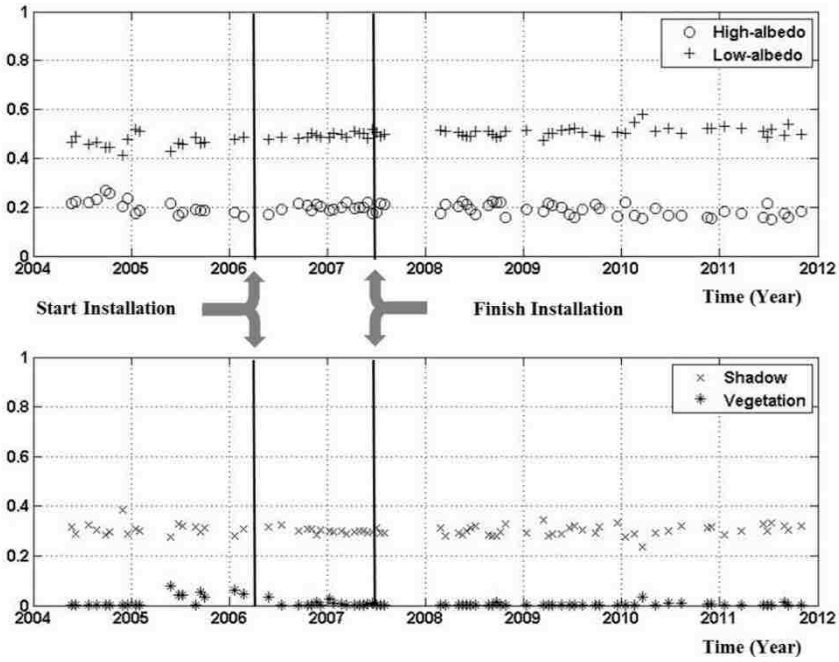

Figure 3.11 Time series of land-cover types at Point 2A, located outside Nevada Solar One

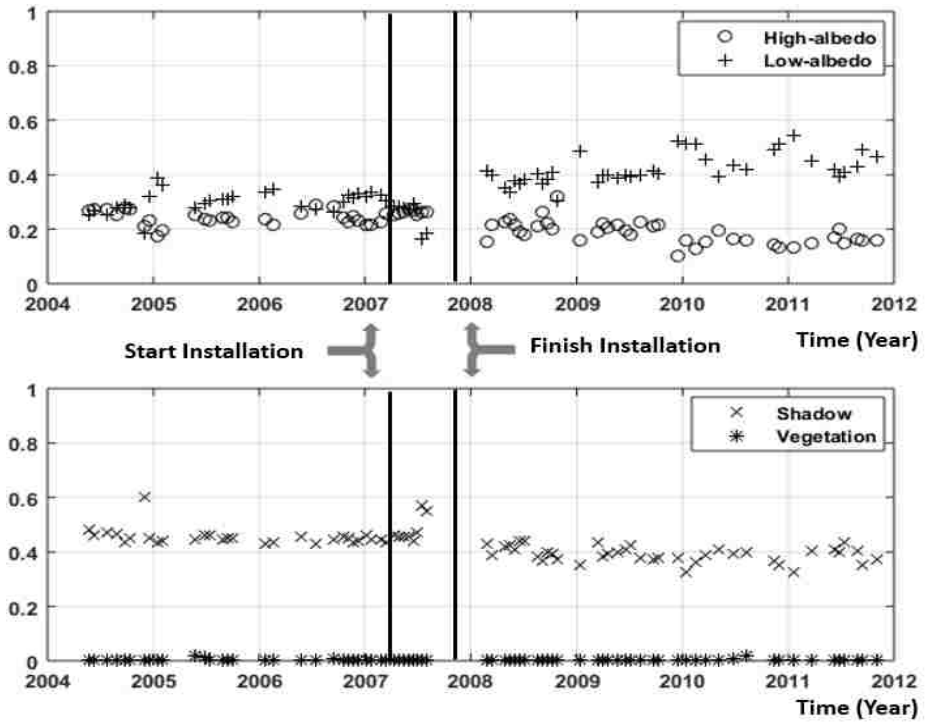

Figure 3.12 Time series of land-cover types at Point 1B, located inside the Nellis Solar Power Plant

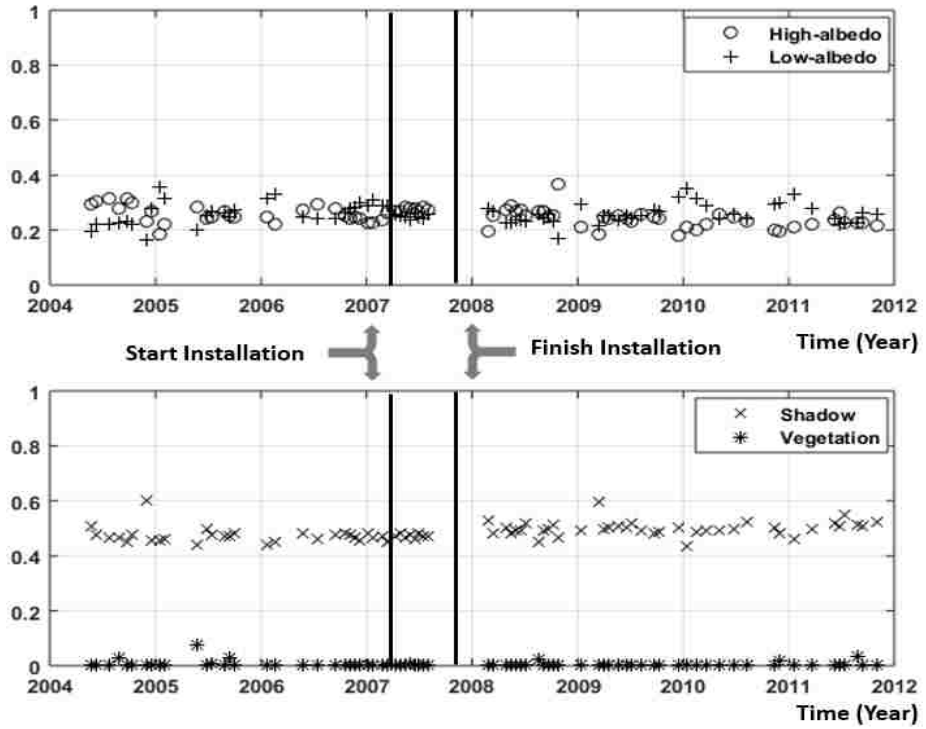

Figure 3.13 Time series of land-cover types at Point 2B, located outside the Nellis Solar Power Plant

For clarity, high-albedo and low-albedo fractions are plotted separate from vegetation and shadow fractions. Mean fraction values of endmembers for pre-installation, syn-installation, and post-installation at Points 1A, 2A, 1B, and 2B are calculated (Table 3.2).

Table 3.2 Mean values of Endmembers for Pre-installation, Syn-installation, and Post-installation at Points 1A, 2A, 1B, and 2B

Point	Endmember	Pre-Installation	Syn-Installation	Post-Installation
Point 1A	HA	18.47	39.18	19.13
	LA	53.01	46.05	63.12
	SH	25.98	14.77	16.38
	VG	2.53	0	1.36
Point 2A	HA	20.31	19.6	18.53
	LA	46.5	48.84	50.77
	SH	30.46	29.47	30.42
	VG	2.73	2.08	0.27
Point 1B	HA	24.30	24.82	18.72
	LA	30.10	26.89	42.11
	SH	45.43	48.26	39.04
	VG	0.16	0.03	0.13
Point 2B	HA	25.94	26.58	24.10
	LA	26.23	25.30	25.75
	SH	47.32	47.98	49.88
	VG	0.5	0.13	0.27

The time series plot of endmember types at Point 1A, located inside Nevada Solar One, is shown is Figure 3.10. The low-albedo fraction decreased during the construction, and increased after the construction. Furthermore, the high-albedo fraction increased during the construction, and then decreased after the installation of the solar panels. There is no significant change for the vegetation fraction for pre-construction and post-construction. During construction, because the surface is being prepared for installation of the solar panels, grading and shrub removal, the land

cover would be bare soil, which is brighter when compared to shrubland. Therefore, high-albedo is increased and low-albedo is decreased during the construction phase. After construction, the soil is covered with solar panels and partially shadow. Thus, reduction of the high-albedo and increase in the low-albedo fraction is expected after construction.

On the other hand, the results for Point 2A, which is located outside of Nevada Solar One at a distance of 1500 m from Point 1A, show that the endmembers fractions are not affected by solar-facility construction (Figure 3.11). In other words, the mean value of the endmember fractions for pre-installation, syn-installation, and post-installation do not change significantly (Table 3.2). In Point 2A, low-albedo had the highest fraction and vegetation had the lowest fraction. The low value of the vegetation fraction seems logical because the facility is located in an arid area with a low amount of vegetation. In addition, the dominant land-cover type in the area is shrubland and barren, which is represented as a combination of mostly low-albedo, high-albedo, shadow, and a small amount of vegetation.

Figure 3.12 and Figure 3.13 show similar results for the Nellis Solar Power Plant. Figure 3.12 shows the changes for the time series of the endmember types for Point 1B within the facility's area, and Figure 3.13 for Point 2B outside of the facility. The low-albedo fraction increased and the high-albedo fraction decreased after construction at Point 1B within the facility (Table 3.2). Nellis Solar Power Plant construction was required less land preparation (grading and shrub removal) compared to Nevada Solar One construction; thus, the changes in endmember fractions between pre- and syn-installation is negligible at Point 1B. The fraction of vegetation is close to zero before and after the construction at Point 1B. Figure 3.13 displays the time series of the endmember changes at Point 2B, which is located 850 m from Point 1B. According to the plots,

the endmember fractions in areas outside of the facility did not change significantly by the construction of the solar facility.

In order to compare the endmember fractions during pre- and post-construction in the entire area, the mean value of each endmember fraction in each pixel for post-construction is subtracted from the pre-construction value of that pixel. The following equation summarizes the operation,

$$\Delta F = F_{post} - F_{pre} \tag{3.2}$$

where ΔF is change in land-cover fraction, F_{pre} is the mean value of endmember fraction for pre-construction, and F_{post} is the mean value of endmember fraction for post-construction. Figure 3.14 shows the results for Nevada Solar One and Figure 3.15 for the Nellis Solar Power Plant.

In Figure 3.14 and Figure 3.15, the blue color represents a zero value, which means that no changes have occurred in those pixels between pre- and post-construction in terms of the corresponding endmember type. Moreover, the red color indicates higher values, which represent an increase of the fraction after the installation. Similarly, the green color indicates lower values, which means that the fraction of the endmember decreased after construction. The color of the pixels that include solar panels for low-albedo is pink and red (Figure 3.14 and Figure 3.15), which means that the fraction of low-albedo surface increased after construction. The plant borders are relatively light blue because the soil had been disturbed; however, no solar panel is installed there to absorb the light, produce shade, and increase the low-albedo. Equally, the colors of bordering pixels are pink in high-albedo, which indicates an increase of high-albedo fractions. It shows that disturbed or bare soil reflects the sunlight more than the solar panels. On the other hand, even though the high-albedo fraction inside Nevada Solar One increased during the construction, there is no significant change in high-albedo between pre- and post-construction. The reason behind this

fact is that the bare soil that increased the high-albedo is covered partially after the construction with panel and shade, therefore, the fraction of high-albedo remains close to pre-construction situation. However, since less land preparation was required inside Nellis Solar Power Plant, the soil was disturbed less during construction and therefore, the high-albedo fraction decreased after panel installation compared with pre-installation.

Moreover, in the shadow images, the solar panels areas are green, which means that the fraction of shadow decreased after construction. The decrease in the shadow fraction occurred due to installation of the solar panels but according to Figure 3.7, the correlation coefficient of shadow is low; thus, the shadow fraction images do not have high accuracy. Generally, in Nevada Solar One, rows of parabolic concentrators with mirrors are used to exploit the sun's energy and are aligned on a north-south axis. Because the concentrators track the sun's location, they are built at regular spaces to catch the sunlight with the maximum efficiency. Thus, it is expected that shadow exists in the distance between the concentrators and the length of shadow changes in different seasons and different times in a day. In contrast, the Nellis Solar Power Plant uses single-axis PV solar panels. In this case, the solar panels are installed separately (not in rows). Therefore, the fraction of shadow should be more after the construction at the two solar facilities.

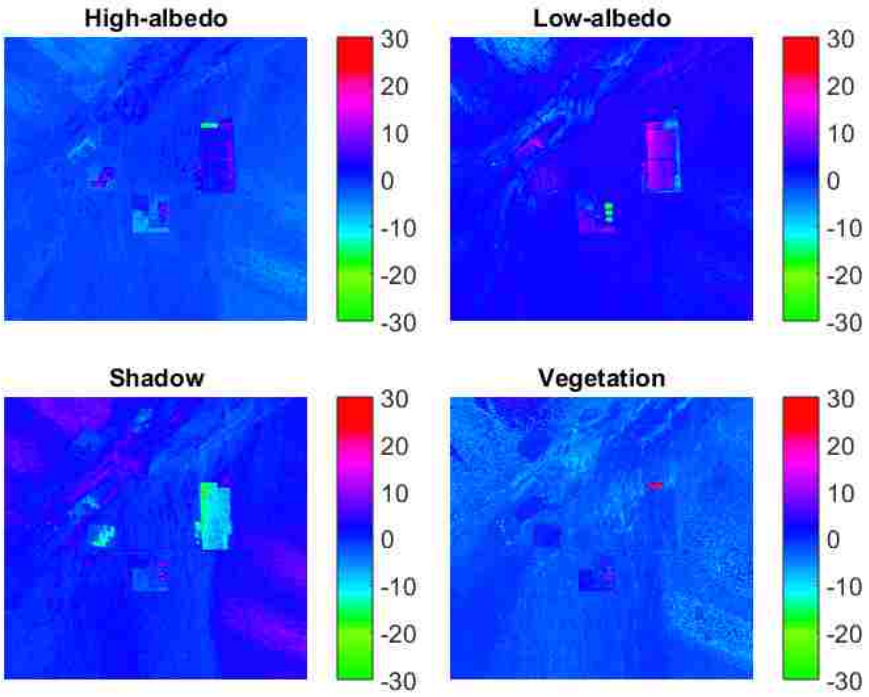

Figure 3.14 Mean difference of pre- and post-installation at Nevada Solar One for high-albedo, low-albedo, shadow, and vegetation.

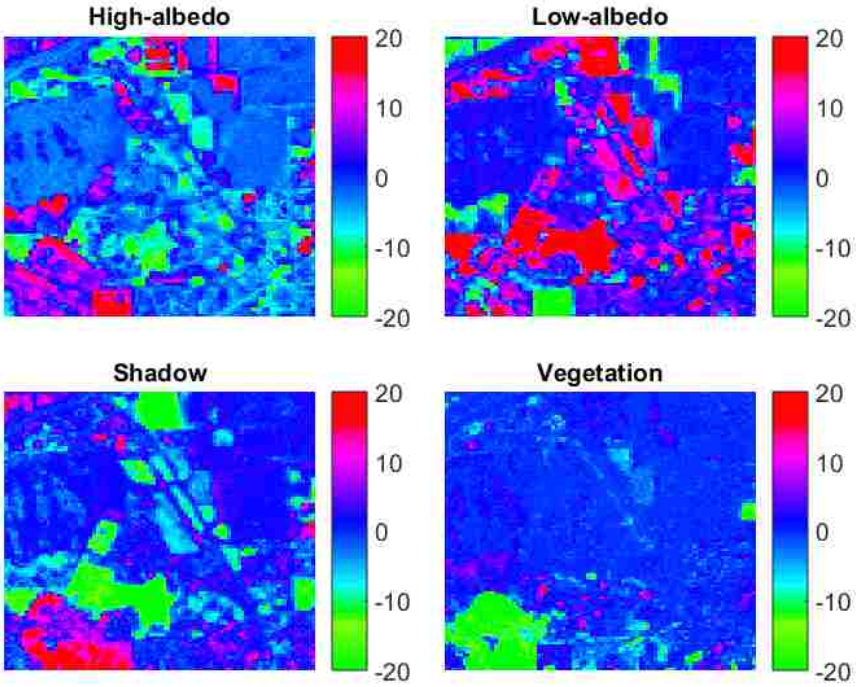

Figure 3.15 Mean difference of pre- and post-installation at the Nellis Solar Power Plant for high-albedo, low-albedo, shadow, and vegetation

Vegetation fractions did not change significantly from pre- to post-construction. Consequently, the color of the endmember image for vegetation, which represents changes due to solar-facility construction are almost the same (blue) all over the areas, and even the facilities are relatively hard to distinguish in Figure 3.14 and Figure 3.15. The reason is that the facilities are constructed in arid areas, therefore, the amount of vegetation is negligible from the beginning of construction onwards. According to Figure 3.14 and Figure 3.15, it was expected that this method will reveal a halo of impacted pixels in the immediate vicinity of solar installations. The output revealed no such halo. Nevertheless, we conjecture that such effect might be profound in areas with higher vegetation. It means that, based on the aforesaid analysis, the effect of solar facility construction on land-cover patterns in neighboring area is negligible in this area (especially Figure 3.14 that shows NS-1 which has been built outside the urban area).

3.7 Summary

In this objective, the effects of two USSE installations on land cover in an arid environment is studied. This study is conducted at Nevada Solar One and the Nellis Solar Power Plant in the southwest region of the U.S., both installed within the last decade. The effects are measured using changes in the land-cover types within and around each facility.

Two common methods for spectral data treatment are tested: PCA and MNF. According to the validation process, PCA-Normalized and MNF-Original datasets are selected as the data-preparation method. Endmembers are defined based on a two-band scatter plot of pixels. The common endmembers in all the scatter plots are determined as high-albedo, low-albedo, shadow, and vegetation. It needs to be mentioned that each endmember does not necessarily indicates

specific land-cover type, however, change in endmember fractions can be inferred to change in land cover.

Among the applied treatment methods, SMA on PCA-Normalized have the highest accuracy with correlation coefficient of 0.72 and 0.62 for high-albedo and low-albedo, respectively. In addition, SMA on MNF-Original showed the highest accuracy to estimate vegetation fraction ($r = 0.81$). In order to understand the effects of solar facility construction on land cover, the changes for endmember trends are compared using pre- and post-installation fractions.

The land preparation process including shrub removal and grading increase the high-albedo fraction but the fraction decreases after solar panel installation. The increase in the high-albedo fractions indicates the increase in solar reflectivity of the soil surface after site preparation. Reflectivity is directly related to thermal characteristics of a surface and represents the solar radiation absorbance rate. In addition, the results of land-cover analysis of the areas within the facility showed that the low-albedo fraction increased after construction. The fraction of vegetation was close to zero before and after the construction, due to the plants being constructed in an arid area.

Although land-cover radiative characteristics are significantly affected after construction within plants area, land-cover analysis of the areas located outside of the facilities showed that the endmember fractions for pre-, syn-, and post-installation do not change significantly. Since the endmember fractions do not change, it can be interpreted that land-cover types do not change as well. Such change is not observed even in the areas close to the plants.

The results of this study generally appertain to the effects of USSE installations on land-cover trends in arid environments. The results might be different in other areas, especially where the vegetation fraction is higher. In addition, endmember types that indicates that various classes of land-cover types could be different in other studies. For example, low-albedo could represent water bodies and asphalt, even though these two land-cover types could be defined individually as endmembers.

Due to increasing trends in USSE plant construction, it is important to understand their effects on the environment and land cover. Land-cover change may impact on temperature, biodiversity, soil degradation, infiltration rate, groundwater level and hydrology of a region. The significance of this research is determination of land-cover change caused by construction of USSE plants. It provides useful insight into their effects on land cover at two solar plants in Nevada. This work has been published in "Renewable and Sustainable Energy Reviews" (Edalat & Stephen, 2017).

4. CHAPTER 4- EFFECT OF UTILITY-SCALE SOLAR ENERGY PLANTS ON LAND SURFACE TEMPERATURE

4.1 Introduction

Land surface and ambient temperature can alter due to USSE plant construction and it is important to understand the impacts of USSE plants on land surface. Solar plants are designed to collect sun's energy and thus, cause energy imbalance in the region through changing the surface albedo, reflectivity, and absorbance. The panel temperature differs from land surface temperature, which may need additional considerations for utility-scale plants. In addition, solar panels cause shading on the ground where the aerial footprint of shade changes daily and seasonally. Augmented with regional climate change, solar plants can effect plant ecosystem and potentially result in the alternation of vegetation types (Cho et al., 2010). Wildlife and habitat loss is one of the main impacts as a result of temperature rise in a region. Furthermore, with the population growth and increase in the popularity of solar energy, the distance between residential areas and solar plants are decreasing, and following that, urban areas and human life might be affected as well (Barron-Gafford et al., 2016). Therefore, it is important to understand the thermal effects of USSE facilities inside and outside the plants.

4.2 Research Approach

This objective aims to study the thermal effects of USSE facilities. This study analyzes the time series of land surface temperature (LST) with particular comparison of pre- and post-installation conditions. The significance of LST trends due to USSE construction in the plant areas is determined. A statistical trend analysis of remote sensing based LST is performed to quantify the role of USSE with a particular consideration of panel shadowing. LST is obtained from top of

atmosphere brightness temperature observed by Landsat 5 TM and Landsat 8 TIRS. Brightness temperature is converted to LST using land surface emissivity (LSE). Since LST varies daily and seasonally, it can overwhelm the variations due to construction of a facility. Therefore, LST data is treated to remove seasonal and gradual temperature variation in the data. The shadowing of the land surface due to solar panels is also studied in relation to LST. The proportion of shadow casted by panels is estimated by analyzing sun angles for different times of year to determine impact on LST.

4.3 Study Area

This study is conducted in Copper Mountain Solar 1 (CM1) which is located ~40 miles southeast of Las Vegas, in the Eldorado Valley near Boulder City, Nevada. Construction of this 58-MW solar plant was completed in December 2010. This area is selected to study the LST impacts of USSE plants because of two main reasons. First, there is no developed area close to this region and all the possible observed impacts are most likely because of the solar plant facilities. The second reason is that because there are five USSE facilities installed in this region, if USSE plants have any impacts on LST, it should be observed. Figure 4.1 compromises each USSE project completion year in the study area. The plant uses PV solar energy through approximately one million thin-film PV modules. CM1 is built in the vicinity of four other USSE plants; Nevada Solar One, Copper Mountain Solar 2, Copper Mountain Solar 3, and Copper Mountain Solar 4. Figure 4.1 shows an aerial view of solar plants in the Eldorado Valley indicating the starting year. All of the plants use PV technology except Nevada Solar One that uses CSP technology. The dominant land-cover type in the area is shrubland.

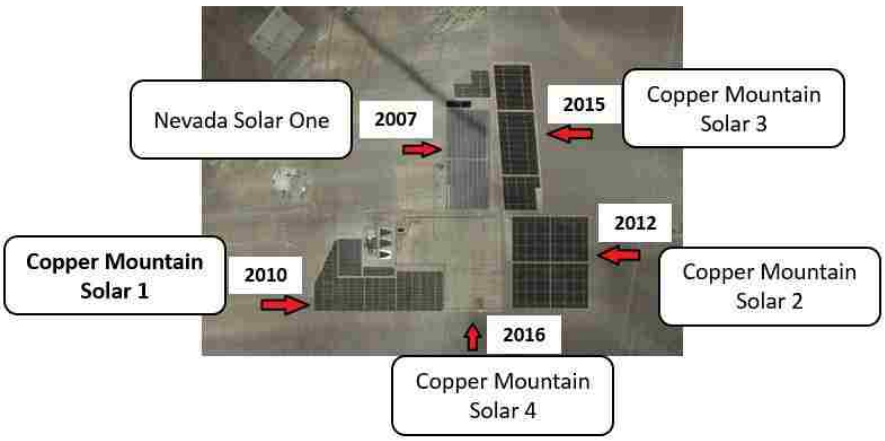

Figure 4.1 Study area (acquired March 15, 2016)

4.4 Remote Sensing Data

The Landsat 5 TM and Landsat 8 TIRS data (path: 39 and row: 35) are used to obtain LST. Landsat 5 and Landsat 8 launched in 1984 and 2013, respectively, but Landsat 5 transmitted its last image on January 2013. LST used in this study ranges from January 2005 to September 2016 estimated from 134 cloud free images taken at 10 AM local time (91 images from Landsat 5 TM and 43 images from Landsat 8 TIRS, 700 by 800 pixels). Spatial resolutions of thermal infrared band in Landsat 5 TM and Landsat 8 TIRS are 120 and 100 meters, respectively. Both bands are resampled to 30 meters in the delivered data product of quantized calibrated pixel values (DN) that are first converted to spectral radiance at the sensor's aperture and then converted to top of atmosphere (TOA) brightness temperature in Kelvin. In addition to remote sensing data, ground data is measured for ε retrieval for inside CM1 using FLIR ONE, which is a thermal imaging device that is used for in situ surface temperature measurements (http://www.flir.com/).

4.5 Methods

The overall research approach is based on the statistical significance of trends in time series of temperature. However, it involves three key steps including temperature retrieval from remote sensing data; removal of background seasonal trends to enhance any impact of USSE, and shade fraction quantification. Therefore, methodology is divided into three main sections. In the first section, LST retrieval using LSE is explained. Because of the high complexity of the land surface inside the plant area, emissivity of inside and outside pixels of CM1 are calculated separately. For outside pixels, NDVI-based method is applied, whereas for inside pixels, field measurements are implemented. In the second section, a method to treat LST data is explained. The purpose of treatment is to remove seasonal and gradual variation in LST for better comparison between pre- and post-installation of the USSE plant. The treatment method is called difference method, which creates a new dataset from LST (ΔLST i.e., difference of temperature from a reference value). Mann-Kendall test is applied on LST and ΔLST dataset to determine the significance of trends. In the third section, shade analysis is presented to understand the impact of panels' shading on LST inside the USSE facilities. For that purpose, sun's position is calculated at the time of each image acquisition to estimate the proportion of shade in those pixels. Figure 4.2 shows an overview of the methodology which each section is explained in detail in the following sections.

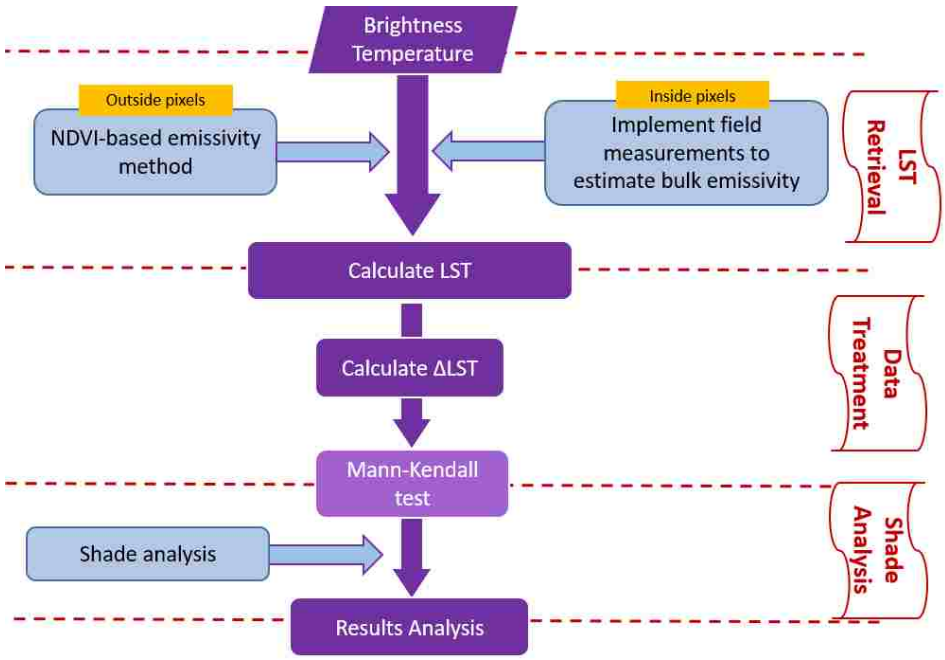

Figure 4.2 Overview of the methodology

4.5.1 Land Surface Temperature Retrieval

In order to retrieve LST, the TOA or at-sensor T_B is calculated from spectral radiance of thermal bands using equation (2.5) (Band 6 of Landsat 5 TM and Band 10 of Landsat 8 TIRS). According to equation (2.8), if ε of each pixel (called the bulk emissivity) is given, LST can be calculated for each pixel using T_B obtained from Landsat TIR images (Artis & Carnahan, 1982). In this research, all the pixels in the study area are divided as either inside or outside of CM1. The outside pixels are in desert area and dominated by shrubland, whereas the inside pixels mainly include three endelements, i.e., solar panels, bare soil, and shade caused by panels. Therefore, different LST retrieval methods are applied for inside and outside pixels. Figure 4.3 shows the flowchart of the methods used for LST retrieval which is explained in detail in the following parts.

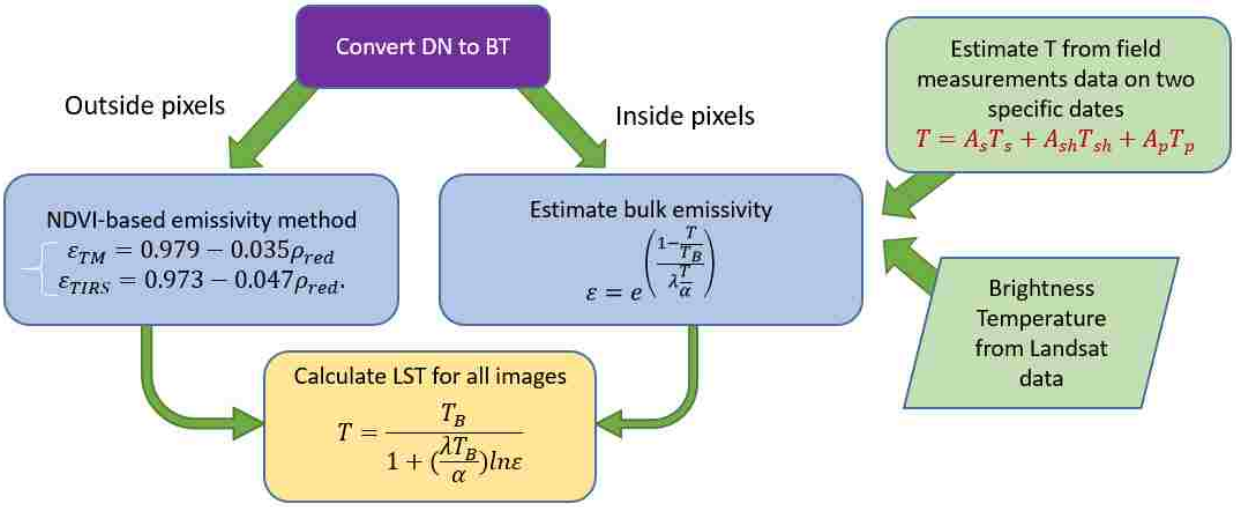

Figure 4.3 Flowchart of the LST retrieval from Landsat 5 TM and Landsat 8 TIRS images

Land Surface Temperature Retrieval for Outside Plant Pixels: In order to estimate ε for outside pixels, NDVI-based emissivity method is applied. Since the study area is located in a desert area and NDVI is less than 0.2 all over the area, equations (2.10) and (2.11) are used for ε retrieval. Therefore, having ε and T_B of outside pixels, LST is estimated using equation (2.8). The obtained ε from NDVI method for the outside plant areas is verified based on ASTER Global Emissivity Database (GED) (Hulley & Hook, 2009, 2011), and the MODIS UCSB Emissivity Library (http://www.icess.ucsb.edu/modis/EMIS/html/em.html).

Land Surface Temperature Retrieval for Inside Plant Pixels: The approach to calculate ε of inside plant area is more complicated than the outside pixels. If ε of inside plant pixels can be estimated, then LST can be computed for all Landsat 5 TM and Landsat 8 TIRS images of the area. Equation (2.8) can be written in a different way to calculate ε for a single pixel,

$$\varepsilon = e^{\left(\frac{1-\frac{T}{T_B}}{\lambda\frac{T}{\alpha}}\right)}. \quad (4.1)$$

According to equation (4.1), knowing T and T_B of a pixel, its ε can be computed. For that purpose, field measurements were performed on two dates to obtain surface temperature of the elements in those pixels and then ε of the pixel was calculated (bulk emissivity). Thus, the field measurements would provide ε of the pixel on the two dates.

Landsat view is considered as top view, because Roll Angle, the amount of Landsat roll at scene center, is ~0.001˚ based on Landsat data description document. Thus, the content of inside pixels from top view are mainly panel, shade and soil which means that three types of surfaces can be seen in such pixels. Accordingly, if surface temperatures of all elements in a pixel are given, the area-weighted average surface temperature can be calculated, and therefore bulk emissivity of the pixel can be determined using the T_B of the pixel. Since CM1 uses fixed-tilt tracking system, the proportion of panel in each pixel is constant all year round but the proportion of shade and soil can change in summer and winter based on sun's angles and positions. For that purpose, the field measurements were implemented two times in a year, once in summer, August 8, 2016, and once in winter, November 29, 2016. FLIR ONE is a thermal imaging device that is used for in situ surface temperature measurements (http://www.flir.com/). Figure 4.4 shows a typical pixel inside CM1 area.

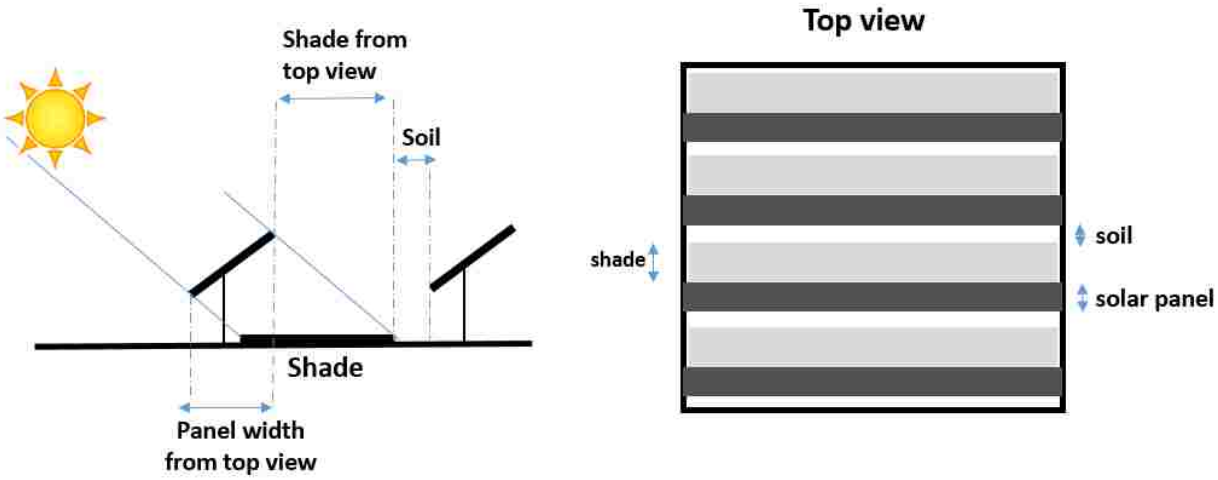

Figure 4.4 A Landsat pixel located inside solar plant area

The average surface temperature of a pixel inside plant area can be computed using

$$T = A_s T_s + A_{sh} T_{sh} + A_p T_p \tag{4.2}$$

where A_s, A_{sh}, and A_p are area contributing fractions of soil, shade and panel, and T_s, T_{sh}, and T_p are surface temperature of soil, shade and panel, respectively. The surface temperature obtained from field measurements can be used to estimate average surface temperature using equation (4.2). However, Landsat images are not available on August 8, 2016 and November 29, 2016 to provide T_B. For that purpose, based on similarity on climate condition (air temperature, moisture and wind) and sun's location, the corresponding T_B used for the pixel is obtained on July 26, 2014 and August 8, 2016, respectively. Again, the similarity of weather condition and shadow length have checked for the two pairs of dates. It needs to be mentioned that all the measurements were taken on University of Nevada, Las Vegas which is ~40 km away from CM1. According to a series of empirical correlations developed by Sandia National Lab, surface temperature of a PV module depends on incident solar irradiance, ambient temperature, and wind speed. Since the sun's location in the sky and the climate condition were the same in each pair of date, the measured data

used to estimate surface temperature for CM1. Therefore, using brightness temperature obtained from Landsat images, and the average surface temperature obtained from field measurements, the bulk emissivity of the pixel for the two dates are calculated. Thus, if the two calculated ε, one in winter and one in summer, are equal, it would be a fair assumption to consider one value for bulk emissivity for all the inside plant pixels, and thus, calculate all the LST based on that.

4.5.2 Land Surface Temperature Data Treatment

The temperature of each pixel mainly relates to seasonal change, gradual change and abrupt change (Verbesselt et al., 2010). Here, abrupt change refers to change in surface attributes. LST varies in each season and it even varies in each year because of gradual variation. Therefore, if the seasonal and gradual variations can be removed from the pattern of LST variation, the effect of surface attribute change on temperature can be detected easier. Figure 4.5 shows an example of simplified LST variation over times. In this example, line 1 represents LST of the pixel which is the summation of line 2, the seasonal variation, and line 3, the gradual temperature variation.

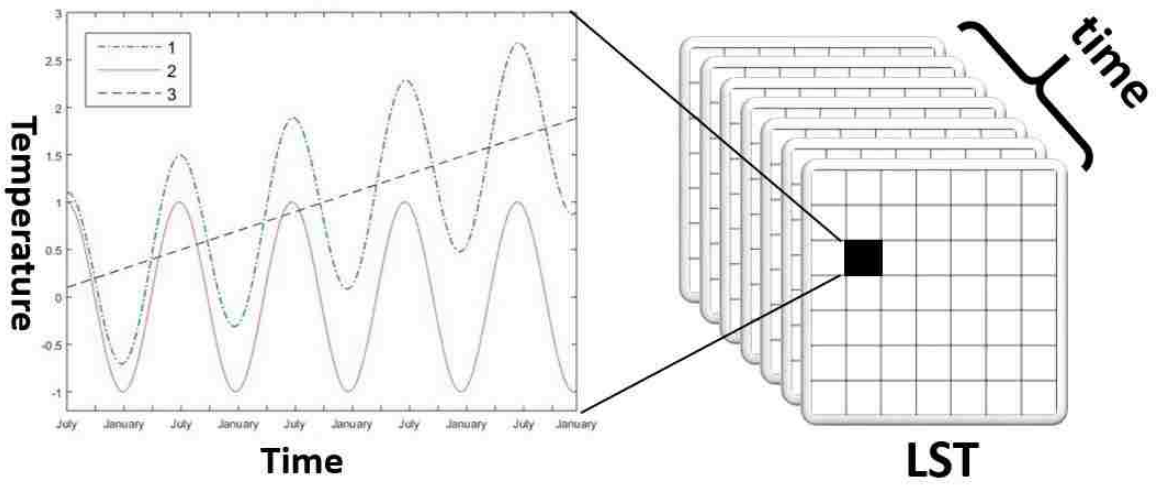

Figure 4.5 Example of LST variation; line 1 shows the LST variation, line 2 indicates the natural seasonal variation and line 3 indicates the gradual temperature variation

To do so, an area which here is defined as reference point is selected as a representative of the area that no intrusion and disturbance has happened during the time period in the area; activities, construction, solar panels, roads, etc. Furthermore, it is far enough away from any activities to make sure it has not been affected. It is expected that the LST of the reference point is able to show the seasonal and gradual LST trend for the study area. This also can be done by tracking temperature at the closest weather station but, first, there is not any weather station close to the study area that records temperature at ~10 AM (Landsat 5 and Landsat 8 crossing time at the area) every day from 2005 and, second, weather stations do not usually record land surface temperature. The data called ΔLST is obtained by subtracting the reference point LST value in each image from the LST value of each pixel. Thus, for a pixel with no surface attribute disturbance in the area, it is expected that ΔLST do not change significantly over time. The difference between ΔLST and LST, that is the actual seasonal and gradual LST variation, is removed in ΔLST based on the reference point variation. ΔLST can be calculated as follows,

$$\Delta LST_{i,j}^{k} = LST_{i,j}^{k} - R^{k}, \quad (4.3)$$

where $\Delta LST_{i,j}^{k}$ and $LST_{i,j}^{k}$ are the ΔLST and LST of *i*th and *j*th pixel at time *k*, respectively, and R^{k} is the LST of the reference point at time *k*. In order to calculate ΔLST, a rectangular area, 6 by 6 pixels in the southern part of the study area is selected as a reference area. For that purpose, the variance and the mean of the LST data for various sizes of reference area from 2 by 2 to 8 by 8 pixels were analyzed. Thus, a 6 by 6 pixels area is chosen due to its small variance and relatively covering large area which makes it more reliable. All the images are reviewed and no intrusion and disturbance has been observed in reference point during the time period.

Figure 4.6 illustrates an example of LST of a pixel, LST of reference point, and ΔLST of the pixel. The change in ΔLST can be easily recognized at year 6 due to surface attribute change. The possible problem with ΔLST method is that it may not happen all the time to find an accurate reference point. In other words, since ΔLST in each pixel is dependent on the reference point, it may not be happening always to find an area with no intrusion and disturbance. In this case, the Man-Kendall test on ΔLST determines if there is any significant trend because of the surface attribute change. ΔLST is more accurate to apply Man-Kendall test than LST because the seasonal and gradual variation are removed in each day based on the same day measurements. However, it needs additional efforts to find the reference point to remove actual seasonal LST variation.

Therefore, after LST treatment, Mann-Kendall test is applied on LST and ΔLST data to determine the significance of the trends due to USSE construction. In the next section, shade analysis is provided in order to estimate the proportion of shadow casted by panels for inside plant pixels. The purpose of shade analysis is to determine the impact of USSE construction on LST by shading on the ground.

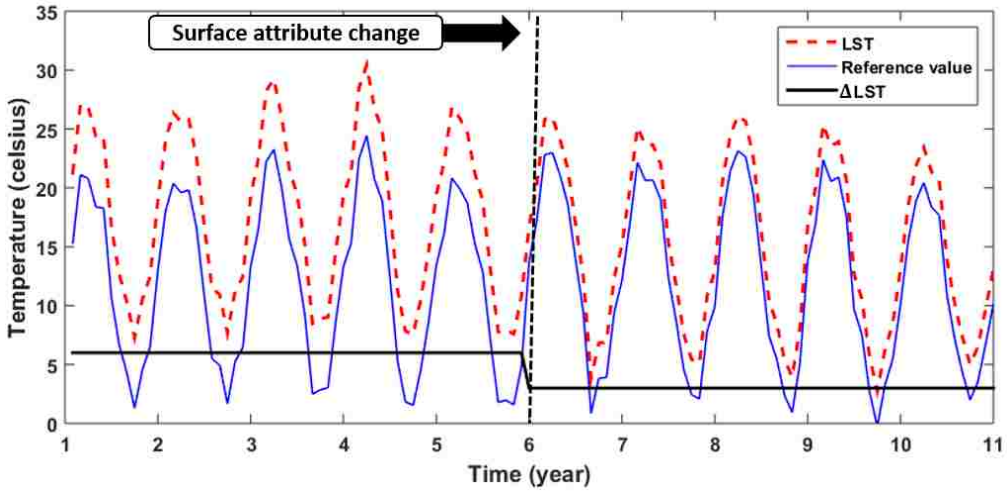

Figure 4.6 LST, LST reference point, and ΔLST

4.5.3 Shade Analysis

Solar panels are designed to capture sunlight and consequently this produces some shade on the ground. The shaded surfaces are not in direct sunlight and do not absorb the sun's energy directly, therefore, the temperature in shaded surfaces are cooler than unshaded surfaces.

Each pixel in Landsat thermal images inside CM1 plant areas includes solar panels and ground surface. The ground surface can be covered partially or fully by shade. Since shadow plays a big role in LST in solar plants, the portion of area covered with shadow in each Landsat thermal pixel needs to be calculated. The only thing that determines the length and direction of shadow is the position of the sun in the sky. To do so, a MATLAB code is written to calculate sun's position (Walraven, 1978). In general, the position of the sun is represented by solar altitude and azimuth angles (Figure 4.7). The altitude angle is the vertical angle between the horizontal plane and an imaginary line between the observer and the sun. The azimuth angle is the horizontal angle between the projection of the imaginary line on the horizontal plane and the North direction.

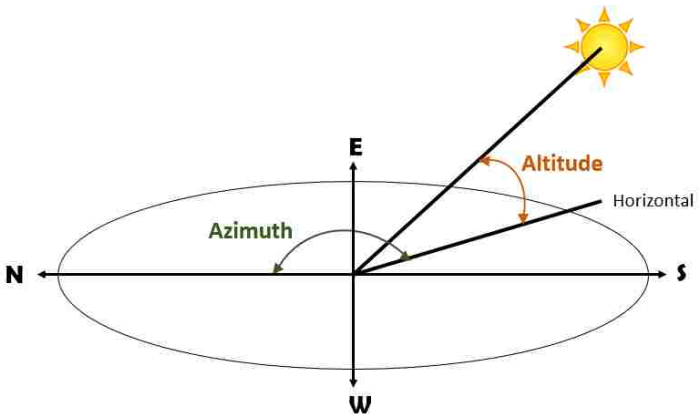

Figure 4.7 Solar altitude and azimuth

The altitude and the latitude are depended on geographic location, time of year and time of day. The azimuth increases every day from sunrise to sunset. In addition, the altitude increases from sunrise to noon, and then decreases until sunset. In the northern hemisphere, the sun's altitude and the azimuth range decreases from summer to winter. Figure 4.8 illustrates the sun's path in the CM1 area from 9 AM to 3 PM on June 21 and December 21, 2016 for every 30 minutes interval. In Figure 4.8, the radius and the altitude are inversely related. As mentioned earlier, Landsat 5 and 8 equatorial crossing time are ~10 AM for the study area all year round. Therefore, the sun's azimuth angle range is from 112˚ to 155˚ (10 AM on June 21 and December 21, respectively) and the sun's altitude angle range is from 26˚ to 65˚ (December 21 and June 21, respectively).

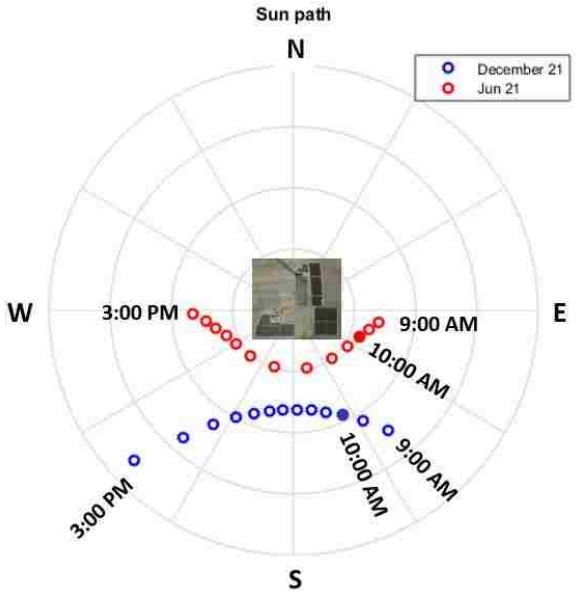

Figure 4.8 Sun path on December 21 and Jun 21, from 9 AM to 3 PM every 30 minutes

Knowing the sun's altitude and azimuth, the length and the position of the solar panels' shade can be estimated. In other words, the portion of the ground covered by shade needs to be computed from the top view to simulate and analyzed the images from the Landsat view. Panels' width, tilt angles, height from the ground and the distance between the panels determine the shade position (Figure 4.4). Each pixel value in the thermal band represents the LST of a mixture of panels, soil and shade. Depending on the fraction of each element, the LST of a pixel represents the average LST of all the elements inside the pixel.

At CM1 facility, panel width is 1.85 meter, tilt angle is 30˚, height from the ground is 0.5 meter, and inter-row space (the distance between panel poles) is 3.75 meter (obtained from http://www.firstsolar.com/ and areal images). Thus, the distance between panels that can be shaded from the top view is 2.15 meter. Figure 4.9 shows the length of panels' shade from top view in 21th day of each month from 9 am to 2.30 pm. In general, it can be seen that the visible length of shade from top view increases from sunrise to noon, and then decreases again until sunset.

Although the altitude is more at noon which can cause shorter shade, the sun shines from the south at noon (the azimuth is close to 180 degree) which can lead to produce longer shade on the ground. The dotted-line determines the length of shade at 10 AM on each month. Thus, it is expected to see huge portion of shade in December, January and November. On the other hand, there is no shade on the ground in the images taken on Jun, May, July, April and August. Hence, the ground is fully covered with shade in winter while there is no shade in the acquired images in summer.

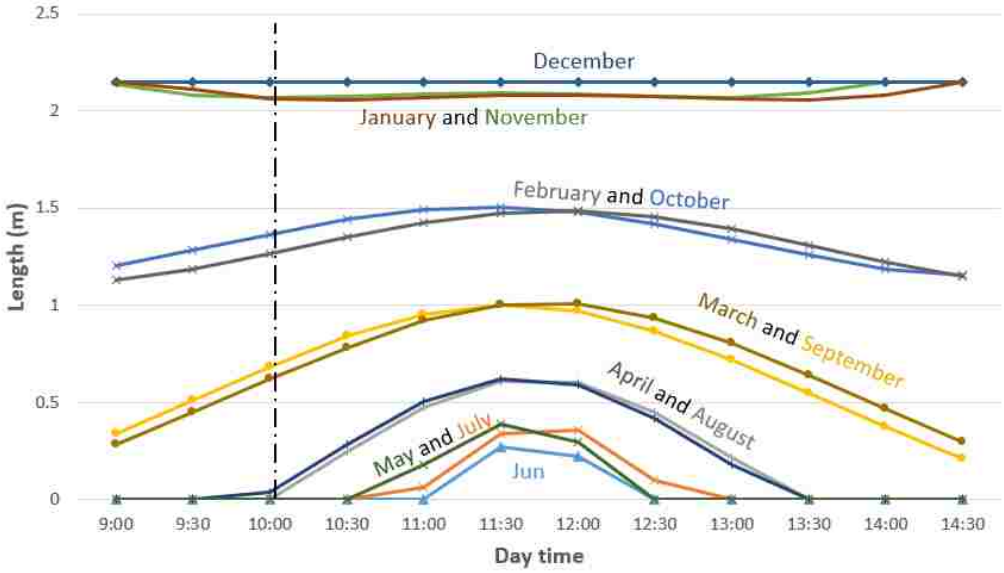

Figure 4.9 Length of panels' shade from top view in different times of a year

Figure 4.10 shows the length of panel's shade in the acquired images. As noted above, the length of shade in summers are 0 and in winters are 2.15 meter, which is the maximum length that can be covered with shade.

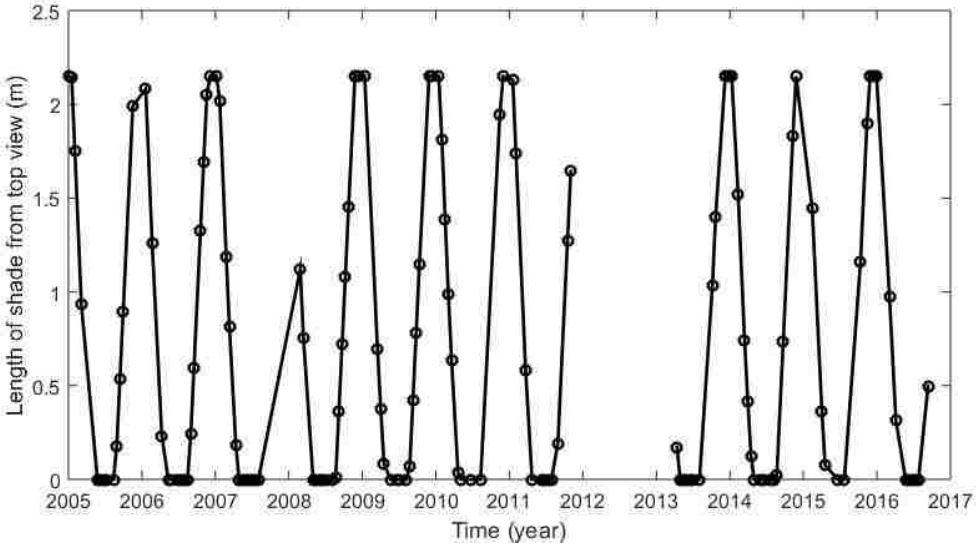

Figure 4.10 Length of shade from top view in all the Landsat 5 and 8 images

4.6 Results

LST is retrieved for the study area from 2005 to 2016, and treated to remove seasonal and gradual variation. Man-Kendall test is applied on all the recorded ΔLST for each pixel to determine the significance of the trends. In the following sections, ΔLST for a pixel inside and a pixel outside of CM1 are plotted and the impact of panels' shade on LST are assessed. The results are analyzed and discussed considering the panels' shading path in summers and winters.

4.6.1 Land Surface Temperature Retrieval

In order to estimate ε inside CM1 using equation (4.1), field measurement is implemented to obtain data required in equation (4.2). As mentioned in the methodology, ε is estimated for two dates, one in summer and one in winter. Table 4.1 comprises the field measurement results including surface temperature of solar panel, soil and shaded soil. Figure 4.11 shows the acquired thermal images in the field. It should be noticed that the data regarding solar panel surface

temperature in Table 4.1 refers to the average surface temperature of the panel that is shown in Figure 4.11. It can be observed that some parts of the PV panels are warmer than the other parts.

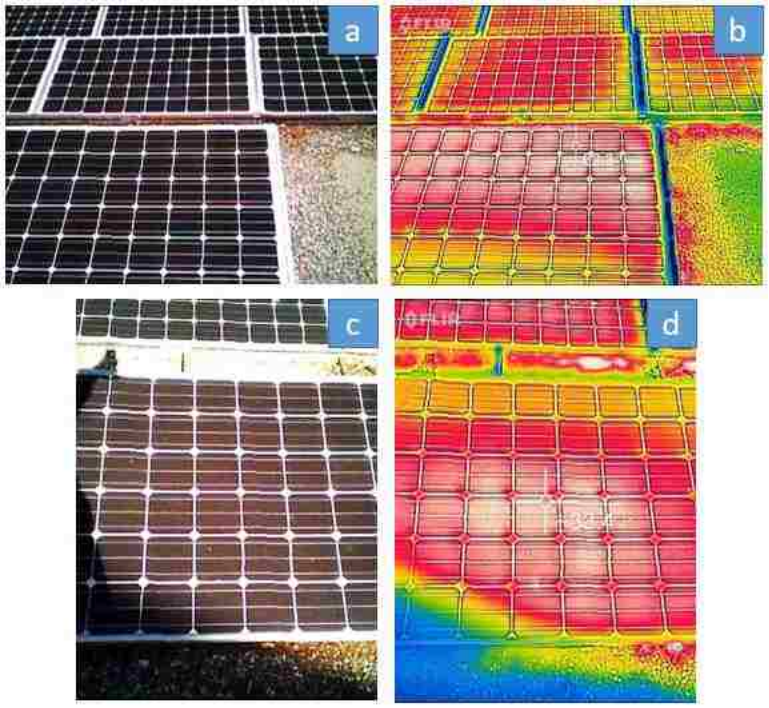

Figure 4.11 Actual and thermal image acquired on August 8, 2016 (a and b), and November 29, 2016 (c and d)

Table 4.1 Field measurement results in Celsius at 10 AM

Parameters	August 8, 2016	November 29, 2016
Air temperature (˚C)	37	12
Solar panel surface temperature (˚C)	63	33
Contributing fraction of solar panel in the pixel	0.43	0.43
Soil surface temperature (˚C)	53	22
Contributing fraction of soil in the pixel	0.57	0
Shaded soil temperature (˚C)	N/A	10
Contributing fraction of shade in the pixel	0	0.57
T (˚C)	57.27 (330.4 ˚K)	19.81 (292.96 ˚K)

In Table 4.1, T, the average surface temperature, is obtained using equation (4.2), and is the kinematic surface temperature for a pixel inside CM1 plant area. T and T_B are needed to be inserted in equation (4.1). Based on air temperature, weather condition and fraction of shade, the closest measured T_B in Landsat images to August 8, 2016 and November 29, 2016 are July 26, 2016 and December 1, 2010, respectively. Therefore, the bulk emissivity for inside CM1 pixels is calculated as shown in Table 4.2.

Table 4.2 Parameters used to estimate inside plant emissivity

Parameters	August 8, 2016	July 26, 2016	November 29, 2016	December 1, 2010
T	330.4 ˚K	-	292.96 ˚K	-
T_B	-	320.3 ˚K	-	284 ˚K
$\boldsymbol{\varepsilon}$	**0.88**		**0.88**	

The bulk emissivity that is calculated for both conditions, summer and winter, is equal to 0.88. Generally, ε of the inside pixels should be close to 0.88 in other seasons, therefore ε of all the inside CM1 pixels are considered to be 0.88 for all the images. The calculated ε is then applied to estimate LST of inside plant area after CM1 construction. In other words, ε of CM1 area acquired from equation (2.10) from 2005 to November 2010 (construction date), and it considered as 0.88 for the rest of the images. Hence, LST is retrieved for the study area including inside and outside CM1 solar plant from 2005 to September 2016. It needs to be mentioned that CM1 uses thin-film PV modules but the one that is shown in Figure 4.11 is monocrystalline solar panel, but according to the study implemented by (Bashir, Ali, Khalil, Ali, & Siddiqui, 2014), the temperature of both types of panels are considered to be equal.

4.6.2 Land Surface Temperature Analysis

Figure 4.12 shows the location and the LST data variation from 2005 to 2016 for the reference point. The temperature variation clearly indicates seasonal LST trends in which winters have the lowest and summers have the highest recorded values.

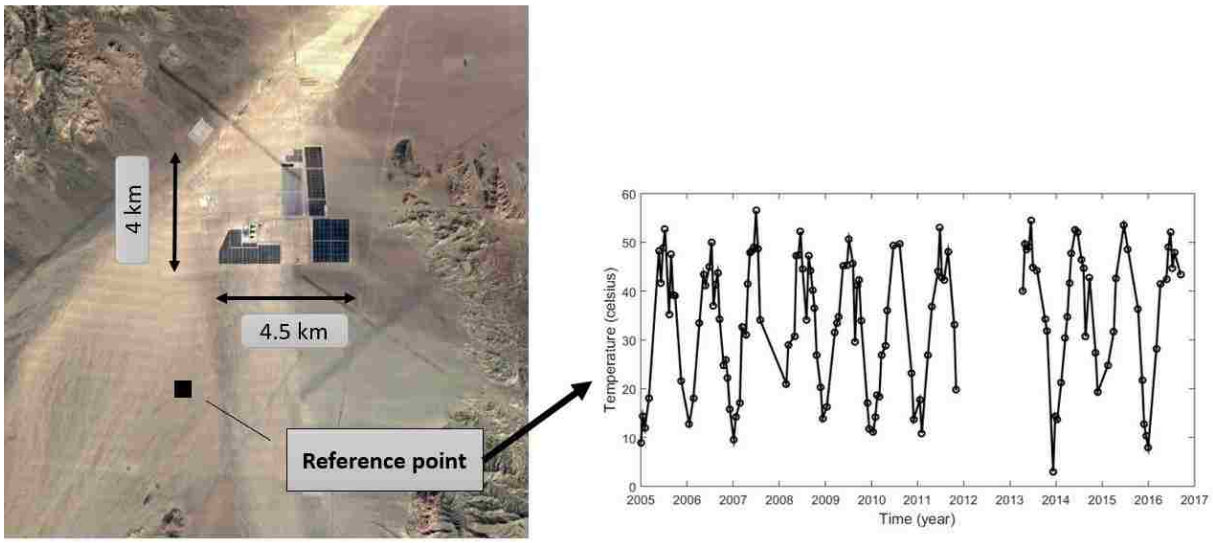

Figure 4.12 Reference point (6 by 6 pixels) location and its LST from 2005 to 2016

To evaluate and make comparison between LST and ΔLST, a pixel inside CM1 is selected. Figure 4.13 shows the location of the selected pixel, LST and ΔLST variation from 2005 to 2016. The seasonal trend in the LST at the selected pixel can be observed in Figure 4.13 where in all cases, LST in summers are higher than winters. Even though the dotted red lines show the plant installation time, it is hard to recognize any change in pattern between pre- and post-installation in LST.

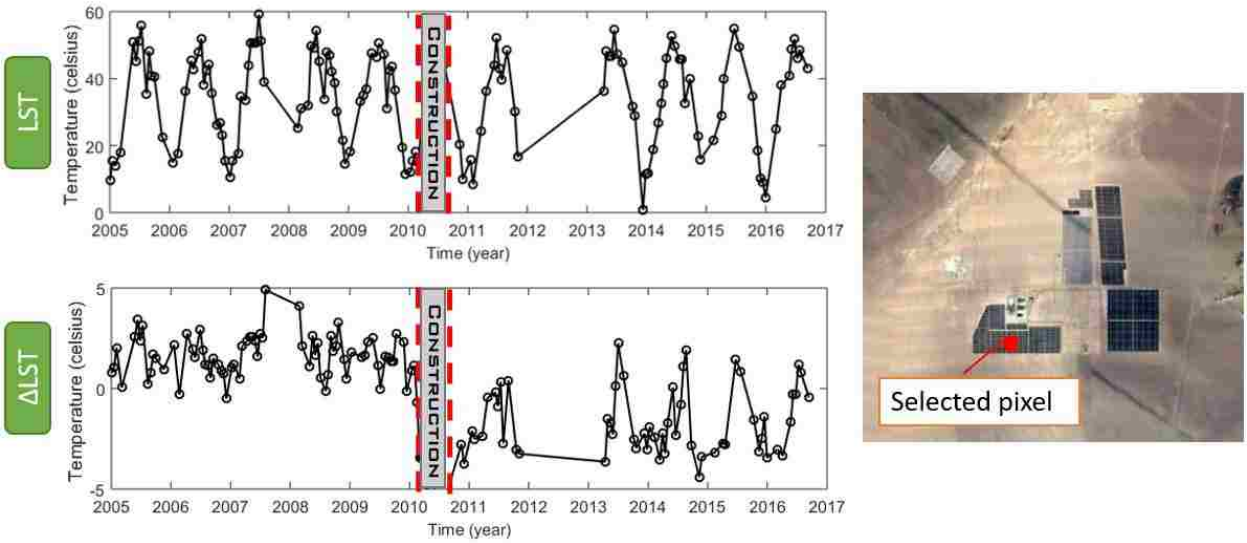

Figure 4.13 LST and ΔLST at Point 1, 2 and 3; dotted red lines show panels installation time

On the other hand, the change in ΔLST after construction is considerable in Figure 4.13 which clearly shows the change in surface attribute at the selected point. For better comparison, ΔLST of two pixels are plotted in Figure 4.14, one inside CM1 plant and one outside. As shown in Figure 4.14, the average temperature after CM1 construction is decreased by 3.23˚ C to compare with before construction for the pixel inside the plant. This value for the pixel outside the plant is 0.25 ˚ C. The blue lines indicate average values before and after construction.

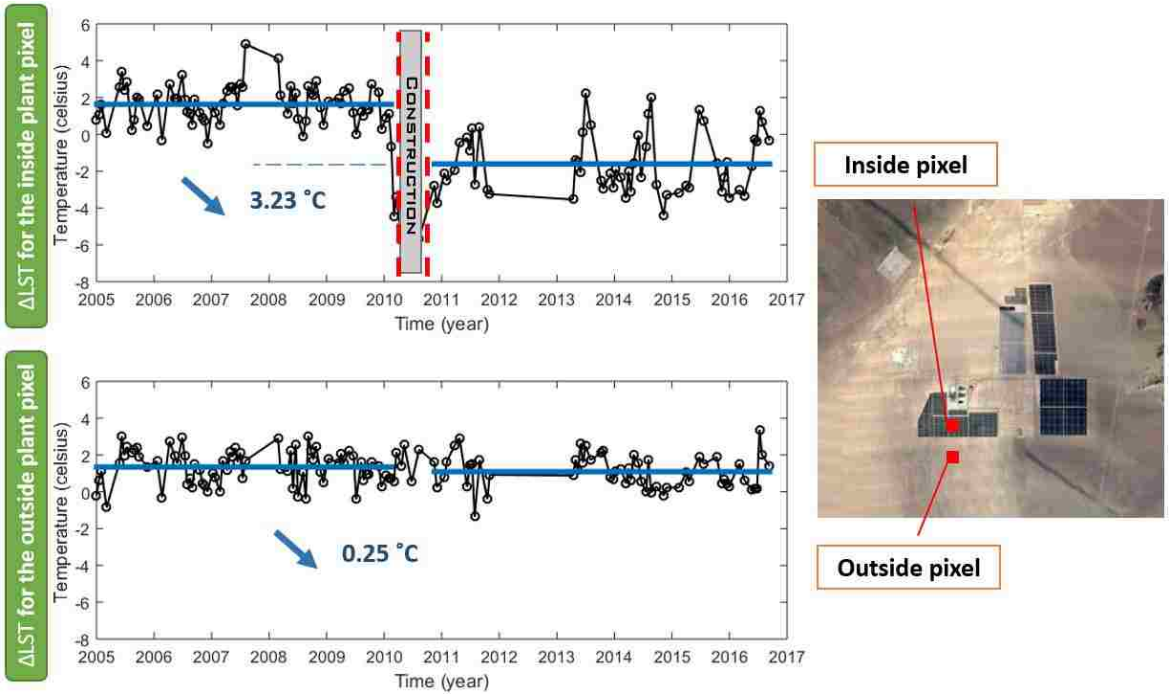

Figure 4.14 ΔLST of the two selected pixels inside and outside of CM1 facility from 2005 to 2016

Mann-Kendall trend test is applied in all the pixels in the study area to determine if there is any significant trend in LST inside and outside of CM1 area. In order to implement Mann-Kendall test, alpha, significance level of the test, is selected as 0.01 to test the rejection of the null hypothesis at the alpha significance level. The test is applied on LST and ΔLST but the results on the LST dataset did not show significant trend in the whole study area (failure to reject the null hypothesis). Figure 4.15 shows the result of Mann-Kendall test on the ΔLST, where light-blue color means significant LST trend and dark-blue color means non-significant trend has been observed. The area shown in red color refers to the inside of the other solar plants in the area were the LST inside them was not studied in this research.

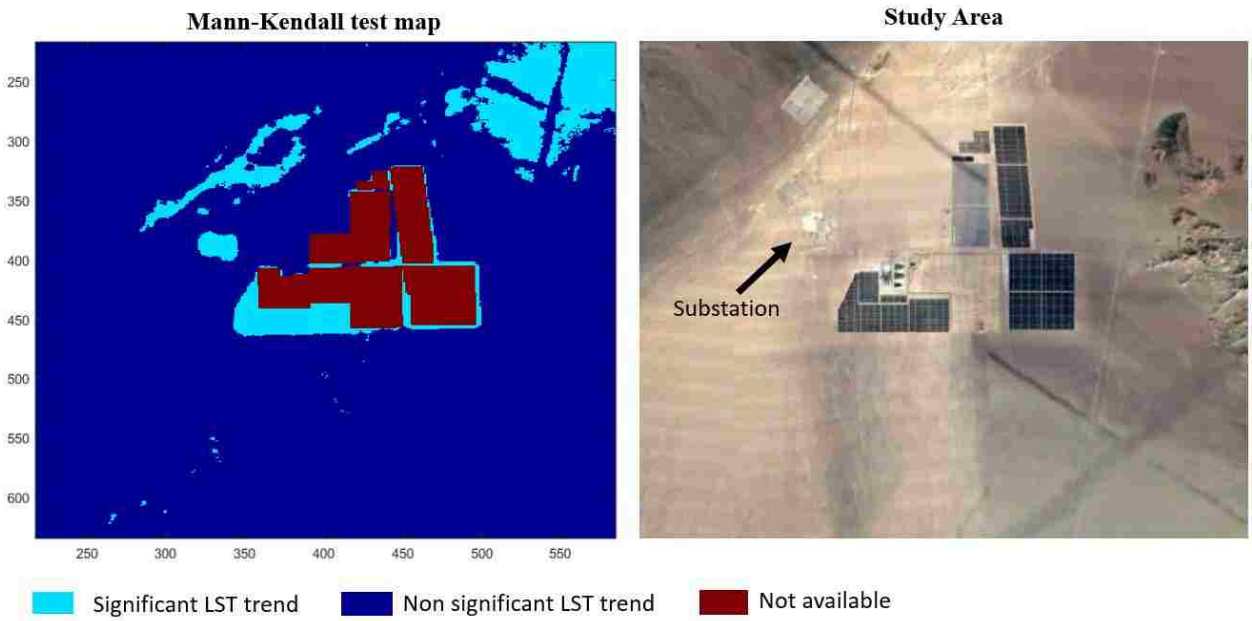

Figure 4.15 Mann-Kendall test results on ΔLST (left), and the study area (right)

4.7 Discussion

According to the results, after CM1 installation LST decreased inside the plant areas, while it did not significantly change outside the plant areas. In this section, it is discussed what parameters influence the LST. Considering the changing in surface albedo and shading on the ground caused by PV panel installation, the results are discussed in this section.

As discussed in the methodology, ε is a critical parameter in LST retrieval. The obtained ε from NDVI method for the outside plant areas was verified based on ASTER GED, and the MODIS UCSB Emissivity Library. On the other hand, the inside plant pixels are mixed pixels and comprise solar panel, soil and shade. The measured surface temperature of solar panels are verified from reported data by (Bashir et al., 2014). Acciani et al. have reported ε of various thin-film solar cell materials which is from 0.83 to 0.96 (Acciani, Falcone, & Vergura, 2010). Therefore, the estimated ε for inside plant pixels seems a decent assumption to compare with previous studies.

The selected pixel shown in Figure 4.13 represents all the inside plant pixels behavior with high precision. This is due to the spatial resolution for thermal infrared bands in Landsat 5 TM and Landsat 8 TIRS (120 and 100 meters, respectively) that are resampled to 30 meters. Thus, because solar panels are installed in regular rows, the content of inside pixels are relatively equal. In addition, the comparison of LST inside plant area showed that the LST of all the pixels inside CM1 are in a very narrow range (less than 1 degree of Kelvin).

ΔLST was selected for further analysis. LST variation can be up to 60˚C from summer to winter, and as mentioned in the methodology, small changes are not detectable in LST trend. In ΔLST, it is tried to remove all the seasonal and gradual variation based on actual measured data at the reference point. Thus, any detectable change in ΔLST refers to surface attribute change.

USSE plant construction decreases LST at 10 AM inside the plant area but does not impact on LST outside the USSE plant area. As shown in Figure 4.14, the average ΔLST after CM1 construction has been decreased by 3.23˚ C to compare with ΔLST before the construction. On the other hand, there is no abrupt change in the LST plot of the outside pixel and subsequently it can be concluded that PV plants do not impact on LST in the surrounding area. The decrease in the average LST inside the plant area is because of the decrease that has happened in LST in winters after plant installation. It is noticed that ΔLST after construction in summers are significantly higher than winters, and is close to ΔLST before CM1 construction. The difference between ΔLST in summer and winter has been observed up to 6˚ C, while such trend is not detected for outside plant pixels. This is happened because of the variation in shade portion in each pixel from summer to winter. In order to perform deeper analysis, Figure 4.16 reveals the impact of shade in ΔLST inside plant area. In Figure 4.16, the upper plot indicates ΔLST of the inside plant pixel, and the

lower plot shows the length of shade in each date. As a result, in winter months, the ground is shaded and it gets cooler which is visible in the ΔLST plot. On the other hand, in summer months, there is no shade in the pixel from the top view at 10 AM. Therefore, the decrease in the average ΔLST, and consequently the Man-Kendall test results that showed significant trend, are mostly refers to winter months ΔLST and the impact of shade on it.

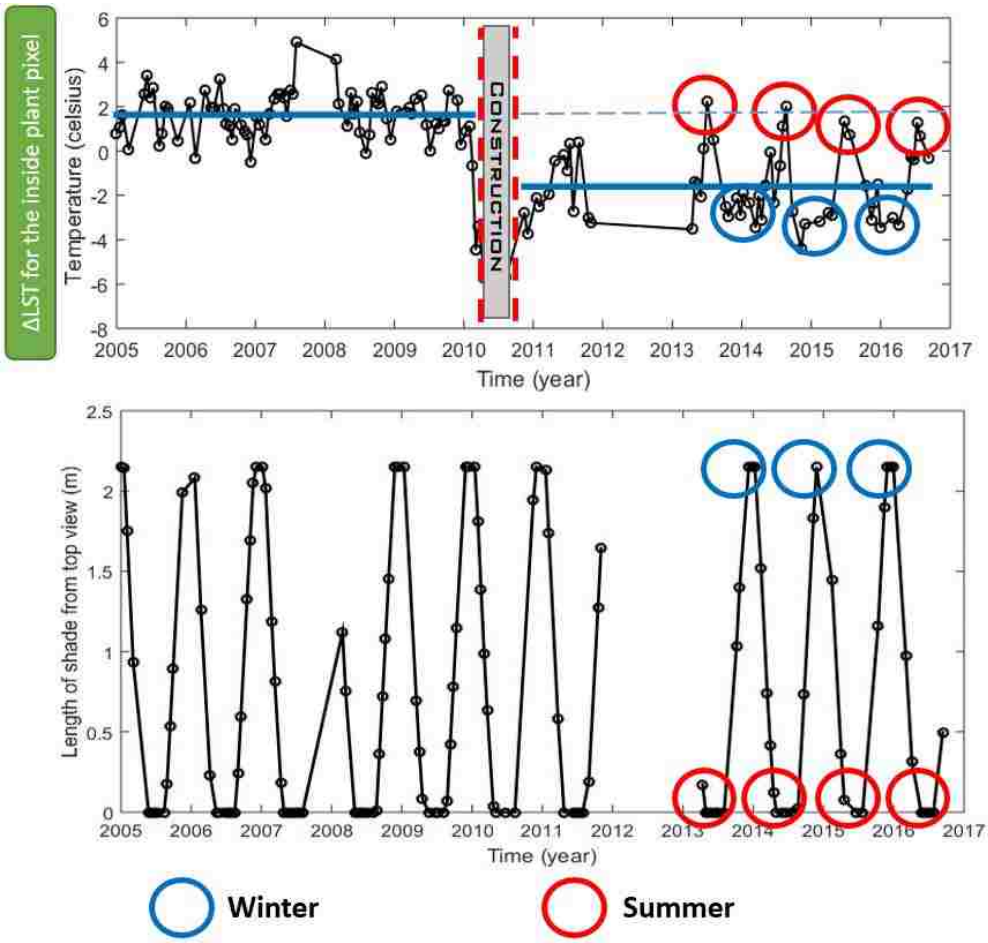

Figure 4.16 DLST and length of shade in the pixel inside CM1 plant in summer and winter

The Man-Kendall test results showed USSE solar plants do not significantly impact on LST at 10 AM in the surrounding environment, especially in the southern part of CM1 (Figure

4.15). The observed significant trend in the areas on the upper right in Figure 4.15 showing with light-blue color is far enough from the nearest USSE plant in the area (~2 km), and the authors decided the observed LST trend is not because of CM1 construction. The small area on the northwestern side of CM1 comprises the plant substation including a variety of structures, transmission towers, grids and conductors and other features that result in an industrial appearance. The significant trend in the LST of substation area is due to surface attribute change for electric transmission. Therefore, the effect of USSE construction on LST is not only restricted to panel areas, but also the substation construction of solar plants can effect on environment and LST.

Site preparation of solar plants increases high-albedo and that makes the ground cooler to compare with before plant construction. From Landsat view, 43% of each inside plant pixels is filled by PV panels and the remaining 57% is filled by soil and/or shadow. In summer months, even though there is no shade in those pixels at 10 AM and the surface temperature of solar panels are higher than soil surface temperature (measured as 63˚C in August 2016), the LST of those pixels are not higher than before plant construction (Figure 4.16). That is happened because the pixel's LST indicates the average surface temperature of all the objects in the pixel. Thus, this fact shows the soil temperature is very lower than the panels' temperature. In other words, land grading which is a site preparation process before plant construction increase albedo of the soil (Edalat & Stephen, 2017). In general, higher albedo relates to higher reflectivity and lower absorbance. As a result, even in summer months, 43% of the pixel (panel's portion) is warmer and 57% (soil portion) is cooler than before construction and therefore the average temperature of the pixel is close to before plant construction.

Even though these results came from snapshots at 10 AM, LST can be estimated in other times based on the location of the sun and shading on the ground. Moreover, CM1 uses fixed-tilt technology and thus, the solar panels are placed east-west direction while single-axis technologies usually place north-south direction to absorb more sunlight. Therefore, shading changes depending on the technology and the position of the panels. On the other hand, location of the plant and specifically latitude determines inter-row distances because in higher latitude the sun's altitude is lower and shadow is longer. Therefore, in higher latitude the distance between panels are more, shadow is longer, and it is expected that decrease in LST would be more than lower latitude areas.

4.8 Summary

In this study, the change in land surface temperature due to CM1 construction is determined based on pre- and post-construction conditions both inside and outside the plant boundary. Remote sensing data acquired from Landsat 5 TM and Landsat 8 TIRS are used to retrieve LST based on thermal bands. The proportion of shadow casted by solar panels in pixels are considered to evaluate the impacts of USSE on LST. The difference method used to treat LST is successful to remove seasonal and gradual temperature variation in the data.

LST is significantly decreased at 10 AM inside the CM1 after the construction. The decrease in LST mainly occurred in winters due to lower sun's altitude, which casts longer shadows on the ground. Thus, longer shadows in winter cause significant decrease in LST inside plants boundary, however, LST in summers are close to pre-development.

In addition, shrub removal and land grading increase high-albedo fraction, which cause lowering the soil surface temperature between the panels. There is no significant panel shadow in summers, thus, LST in summers are closer to the pre-installation condition. This is happening

because after installation, panels get warmer and soil gets cooler than pre-installation (higher albedo), and therefore the mean temperature has not significantly changed.

The results also show that CM1 construction did not significantly impact on LST outside the boundary. However, it is showed that the effects of USSE construction on LST is not only restricted to the inside of plant areas, the substation, gridline and road construction can impact on LST. The reported results are valid for 10 AM and may change at different times in a day.

Inclusion of shadow in the LST analysis improved the explanation of observed trends. The shade and temperature analysis that is provided in this research can be used to understand and predict the behavior of vegetation and biota under the panels. Solar panel installation causes shading on ground and it moves daily and seasonally. Shading path considerably differs from summer to winter and it can create different environment for the animals, plants and other organism living inside the solar plants area and needs to be carefully considered.

5. CHAPTER 5- EFFECT OF A PV PANEL INSTALLATION ON HYDROLOGICAL RESPONSE

5.1 Introduction

Hydrological assessment of solar plants area is critical in order to preserve natural hydrological behavior of the region. USSE plants cause disturbance in soil characteristics during site preparation phase; panel installation, soil compaction, vegetation removal, grading, etc. Furthermore, being in the pathway of the rain drops during a rainfall, solar panels create rain shadows. Almost all of the plants that are under construction and development in the US are intended to use PV technology (Solar Energy Industries Association, 2016). While most of the plants use fixed-tilt technology, more than 20% use single-axis tracking. In single-axis tracking, the rows are usually aligned on a north-south axis and the panels are designed to follow the daily movement of the sun (Wolfe, 2013). Therefore, in single-axis tracking, shadowing of rainfall reaching the ground surface changes with time of day. It can cause serious problems during heavy storm events and therefore, it is important to consider the coupled effect of rainfall shadowing and soil characteristics alteration. For example, during the 2012 summer monsoon season, 6 inches of rain fell over a 2-day period in Genesis Solar Energy Project region located in Chuckwalla Valley, Riverside County, California. It caused a massive flash flood in the area resulting in $5 million in damages and displacement of more than 30,000 cubic yards of soil leading to sedimentation. A detailed analysis revealed that disturbed soils inside the plant area were affected more than the relatively undisturbed soil i.e., the natural drainage did not cause erosion over the undisturbed soils.

USSE projects require less than 5% of average land slope. Often vegetation removal and grading is also required for certain technologies to create relatively uniform topography (Bureau of Land Management, 2012). Otherwise, driven piles and ground screws are used that do not change surrounding soil characteristics (Wolfe, 2013). The changes in land surface characteristics impact the surface runoff and subsequent solar panel installation creates rainfall shadows diverting rain droplets before reaching the ground. The area below the panel does not receive direct rainfall: instead the panel reroutes it to the edge resulting in a concentrated downpour. Henceforth this effect is termed as rainfall redistribution. In typical hydrological analysis of solar facilities, the impact of rainfall redistribution is usually neglected and mostly the reports are focused on changes to soil characteristics. The drainage design and analysis of solar plants that include channel and in some cases detention basin design are conducted without consideration of rainfall redistribution effects. The rainfall redistribution may not have significant impact on a small scale, but significant runoff modification could arise on a utility-scale solar energy plants due to a large spatial footprint of panel shadowing. Thus, it is imperative to understand the impacts of rainfall redistribution on hydrological response of a USSE plant.

5.2 Research Approach

This objective aims to study the hydrological impacts of PV plants in arid regions. Pre- and post-installation hydrological response over single-axis technology is compared. A theoretical explanation is developed to explain flows under the influence of PV panels. Moreover, a distributed parametric hydrologic model is used to estimate runoff before and after the construction of PV plants. Four parameters are identified for sensitivity analysis including PV panel tilt angle, PV panel orientation, antecedent soil moisture, and land preparation practices including

compaction and shrub removal. In particular, impacts of PV plants on peak discharge, time of peak, and runoff volume are related to the geometry of panels and soil properties.

5.3 Hypothesis

It is hypothesized that PV panel installation reduces rainfall infiltration loss during a storm, and therefore, increases runoff volume from an area. Previous studies showed that runoff volume and peak flow discharge increase after land preparation processes including shrub removal and soil compaction. When panels are installed facing toward the watershed's slope, it is expected that peak flow happens earlier compared to the pre-development flow. It is also expected that the effect of panel tilt angle on hydrological behavior increases at lower angles. The runoff volume is expected to increase after PV panel installation due to the rainfall redistribution.

5.4 Theoretical Development

In this section, the impact of solar panel installation on the hydrology of a region is theoretically discussed. Consider an area where a solar panel is to be installed (Figure 5.1). It is assumed that the area consists of a single drainage area and the location of the outlet point is on the lower-right corner. The general slope of the ground is toward south-east. The flow paths in Figure 5.1 represent rainfall overland flow paths when rainfall is uniformly distributed in the area. Suppose that a PV panel is installed in the middle of the region, aligned on an east-west axis, and is oriented south-facing. During a storm, the panel divides the area into three zones; spacer, dry, and wet zone (Cook & McCuen, 2013). Spacer is the inter-row area, which is not covered with the panel. Dry zone is the area located beneath the panel which does not receive direct rainfall. Wet zone is the strip line located beneath the edge of the panel. Since PV panels are impermeable

surface, the wet zone not only receives direct rainfall but that accumulated from panel surface as well. The hydrological behavior of each zone is discussed in the following paragraphs.

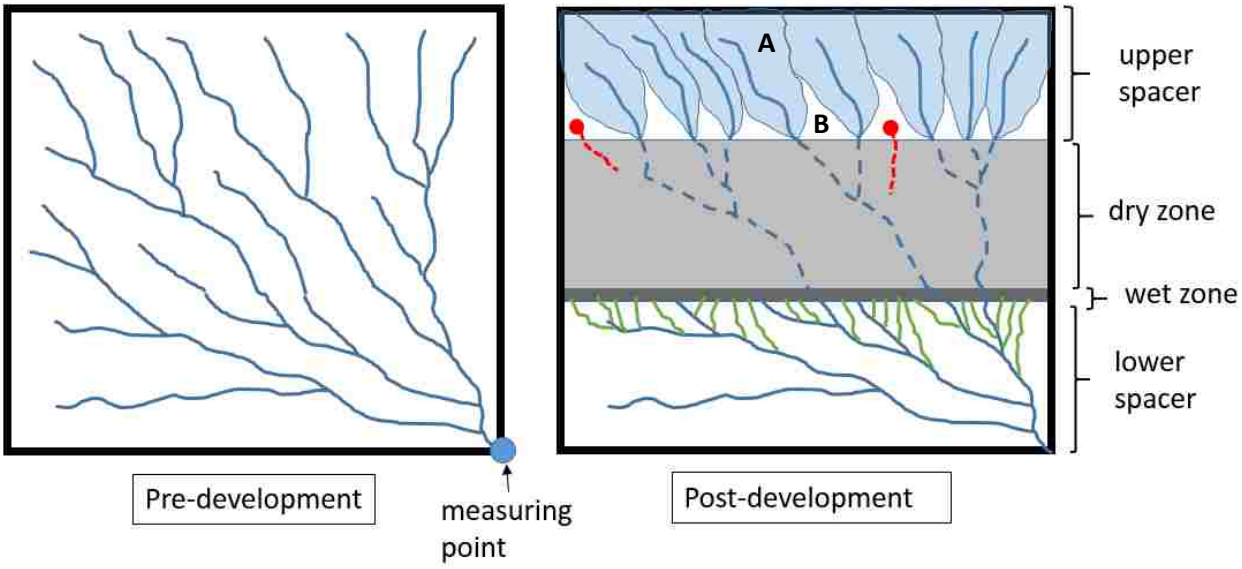

Figure 5.1 Pre- and post-development scheme (PV panel is aligned on an east-west axis, oriented south-facing)

During a storm, a fraction of rainfall becomes runoff after meeting infiltration and evaporation demand and flows over the surface through flow paths. When a panel is installed, the overland flow produced in the upper spacer is not affected and flows under the panel as a sheet flow (dotted-line in Figure 5.1). The rain that falls within the catchments shown in the upper spacer (shown in blue shaded regions, e.g., region A in Figure 5.1) will flow through the main flow paths in the dry zone (dotted-lines). On the other hand, for the rain that falls in the upper spacer but outside of the shown catchment basins (e.g., red dots in region B in Figure 5.1), because of being in smaller catchment basins which parts of them are in the dry zone, and not reaching the main flow paths in the upper spacer, it is expected that this flow does not reach the main flow paths especially for storms with small depths. This happens because most of the runoff is lost through

infiltration in the dry zone. In other words, the rain fallen in those area not only has to overcome the infiltration loss in the upper spacer, but also has to overcome the infiltration loss in the dry zone before becomes runoff and flows over the surface. In case of heavy rainfalls, the produced runoff will eventually reach the main flow paths and becomes free path.

Since the dry zone does not receive direct rainfall, the flow paths that start in the dry zone (relatively higher elevation) will stay dry and do not participate in the overland flow. Even in heavy storms, there might be some areas in the dry zone which are not close to main flow paths that is flowing from the upper spacer. However, since the rain shadow depends on wind, some of the dry zone will get rain under windy conditions. To compare with pre-development, less rainfall will be lost through infiltration in the dry zone. In other words, in pre-development, infiltration loss has to be met in all over the area before surface flow begins, but in post-development, it does not need to happen because of the existence of the flow paths in the dry zone. Therefore, since infiltration decreases in post-development, it is hypothesized that total runoff volume will increase.

Moreover, the rain that was supposed to fall in the dry zone diverts in the wet zone through the panel surface. Indeed, the overland flow in this section is one step ahead compared with pre-development, because it has reached into the wet zone earlier (flowing on a steep and smooth panel) without infiltration losses. Therefore, the wet zone behaves like a source of water for the flow paths in the lower spacer and injects water with higher depth than normal rainfall (green lines in Figure 5.1). The higher depth of water produces higher flow velocity to the outlet point, however, can somewhat compensate the slower flow in the dry zone. Therefore, it is hypothesized that the point of raise of the hydrograph, and the peak flow time for post-development occur earlier compared to pre-development.

To summarize, the area under the PV panel does not receive direct rainfall and that causes the reduction in infiltration loss after pane installation. However, the panel reroutes the rainfall to the edge faster with minimal loss compared with pre-development. Thus, it is hypothesized that runoff volume increases and peak flow occurs earlier after PV panel installation in which the panel is oriented to the watershed's slope.

Now consider the installed PV panel is aligned on an east-west axis but is oriented north-facing (Figure 5.2). In this case, when a storm occurs, the hydrological behavior differs because the wet zone is in the upstream and dry zone is the downstream. Similar to the previous condition, because the flow paths that start in the dry zone will not participate in the overland flow, some parts of the dry zone will stay dry. Thus, less water will be lost through infiltration and again, it is hypothesized that runoff volume will be increased compared to pre-development condition.

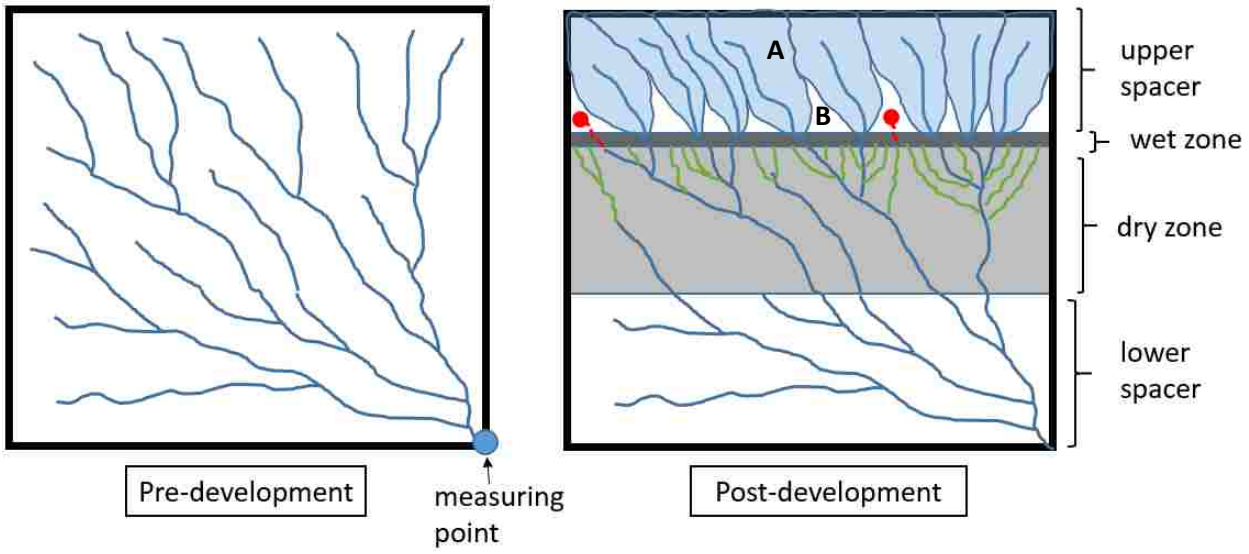

Figure 5.2 Pre- and post-development scheme (PV panel on an east-west axis, north-facing)

The rain that falls within the shown catchment basins in the upper spacer (e.g., region A in Figure 5.2) will be joined to the wet zone and flows in the main flow paths in the dry zone. Furthermore, the rain that falls outside of the shown catchment basins in the upper spacer (e.g., red dots in region B) flows through the wet zone and becomes greater in flow rate and velocity. After the wet zone, runoff flows to reach the main flow paths in the dry zone (green lines). Thus, overland flow has high velocity and after infiltration losses in the dry zone, will be added to the flows produced in lower spacer. Since the wet zone is located in the upstream in this case, it is expected that the point of raise of the hydrograph in Figure 5.1 occurs before than that in Figure 5.2. In Figure 5.1, the wet zone is closer to the outlet point, and unlike Figure 5.2, the high velocity flows passing the wet zone do not need to overcome infiltration losses in the dry zone. Thus, in Figure 5.1 peak flow occurs earlier than that in Figure 5.2. In general, if the angle between direction of the panels' slope and the watershed's slope is called φ (Figure 5.3), it is hypothesized that there is a relationship between φ, and peak flow discharge, peak flow time, and runoff volume.

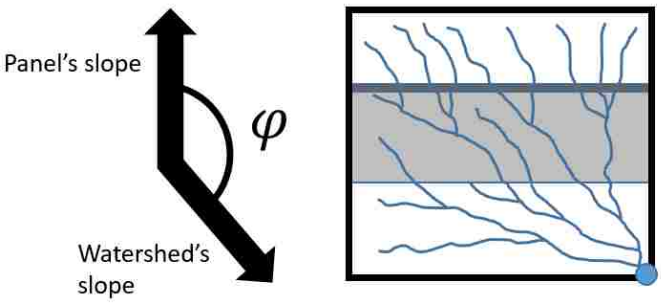

Figure 5.3 Schematic diagram of the angle between panel's slope and watershed's slope

The difference in the predicted behavior between Figure 5.1 and Figure 5.2 is the peak flow time and time of point of raise of hydrograph. As mentioned earlier, when the wet zone is closer to the outlet point, peak flow and point of raise of the hydrograph occur earlier. Moreover, it is

hypothesized that the impacts on hydrological behavior decreases in higher tilt angles, because less area is covered by the panel. Therefore, the dry zone is smaller, and the wet zone receives lower depth of accumulated rainfall in higher tilt angles.

5.5 Study Area and Data

A rectangular area with a footprint of 837 m^2 is chosen inside the Eldorado Valley near Boulder City, Nevada. The area has an arid climate with an annual rainfall of 162 millimeters. The dominant land-cover type is shrubs (USGS National Gap Analysis Program, 2017), and the general slope of the area is less than 5%. According to USDA National Resources Conservation Service, the soil type of the study area is gravelly loamy fine sand (USDA NRCS, 2017). Figure 5.4 shows an aerial view of the study area. A catchment basin with the area of 340 m^2 is selected inside the study area for validation of the hydrological model (Figure 5.4).

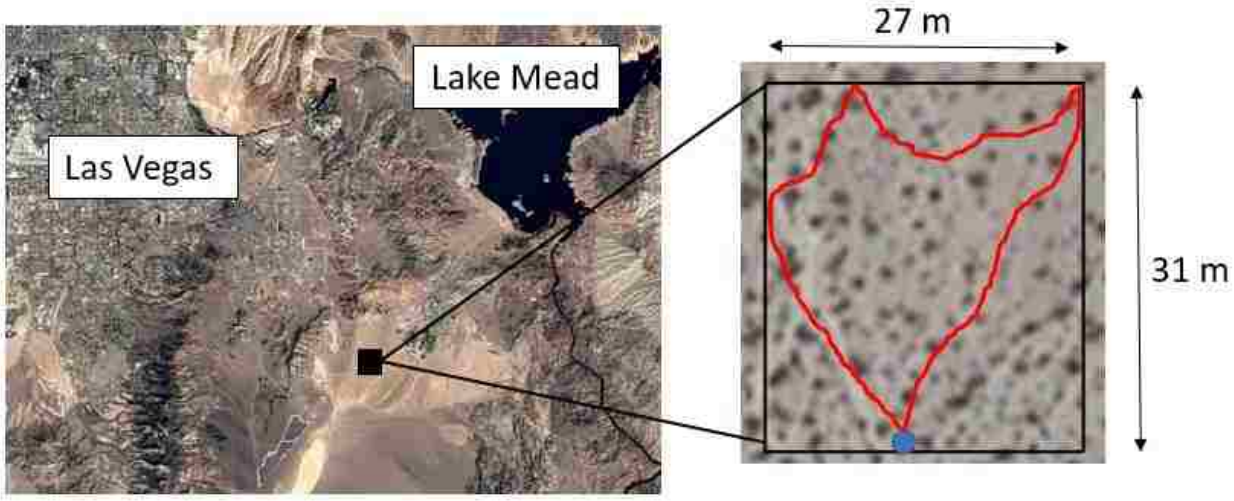

Figure 5.4 Aerial view of the location of the study area and the selected watershed

Light Detection and Ranging (LiDAR) data is used to create high resolution digital elevation map (DEM). The data is interpolated and converted to gridded format to create raster elevation map with 20-centimeter cell size. The void fill method used is natural neighbor interpolation which estimates the elevation between the measured points by applying area-based weights to the terrain's natural neighbors of a query point. The interpolated DEM is used in the hydrological model to estimate the hydrological behavior of the study area after PV panel installation.

5.6 Methods

In this section, first, the distributed parametric hydrologic model used for runoff simulation is explained. Second, the model validation for the study area using HEC-HMS is provided. Later, parameterization for sensitivity analysis is described to verify the hypothesis. Over 350 simulations are performed for various conditions to relate peak discharge, time of peak, and runoff volume to the geometry of panels and soil properties. Figure 5.5 shows the flowchart of methods.

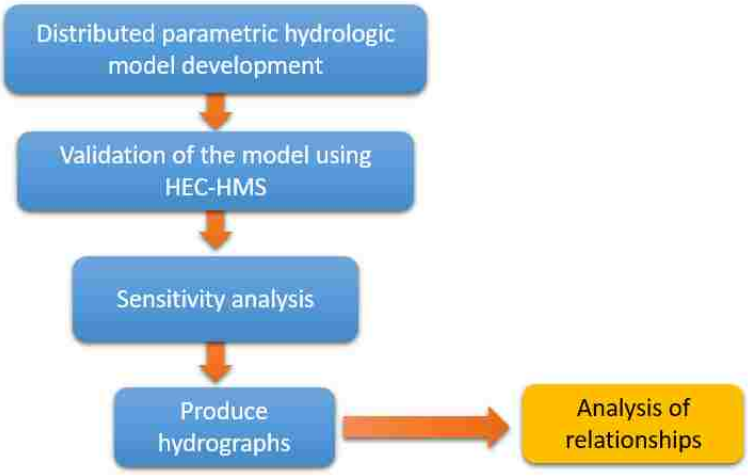

Figure 5.5 Flowchart of the method used

5.6.1 Hydrological Model

A spatially distributed parameter hydrologic model is used to convert rainfall to runoff. The basis of the model is cell-to-cell routing and is a modified version of the procedure used by Smith (Smith, 1993) called GIS-based distributed parameter hydrologic model further explained below. The information needed are raster maps of topographic information, soil types and land cover. Before the use of the hydrological model, few processing steps needs to be applied to derive hydrologically important parameters. Based on the elevation map, the steepest slope of the eight neighboring cells for all the cells are calculated and assigned as the overland flow direction. Therefore, each cell has only one outflow to its neighbor cell but may receive more than one inflow from its neighbors. Using the flow directions for each cell, drainage area is determined for a pour point of interest. In this procedure, the outflow of each cell becomes the inflow of its downstream cell in the next time step. The rainfall losses considered for each cell is infiltration for which Green and Ampt method is used. The coupling of the continuity equation and the Manning's equation for turbulent flow is used transform excess rainfall to runoff for each cell. Figure 5.6 shows the variables used to calculate overland flow where h_1 and h_2 are water depths in the cell in the beginning of each time step, and at the end of each time step, respectively. The symbols a and b represent cell width and length.

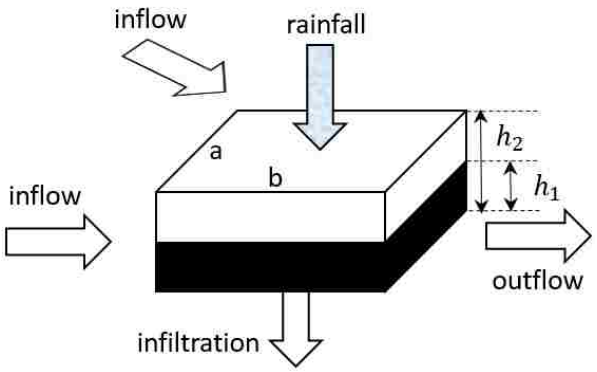

Figure 5.6 Cell dimensions, inputs and outputs

According to Figure 5.6, the continuity equation for the cell in each time step can be written as,

$$\sum inflows - outflow + rainfall - infilteration + \frac{(h_2 - h_1)ab}{\Delta t} = 0. \quad (5.1)$$

Outflow [L^3T^{-1}] is computed using Manning's equation for shallow water overland flow,

$$outflow = \frac{a.h_2^{5/3}.s^{1/2}.\Delta t}{n} \quad (5.2)$$

where s is slope, and n is Manning's roughness coefficient. Equation (5.1) can be inserted in equation (5.2) to compute h_2 and subsequently outflow will be calculated in each time step. Newton-Raphson method is applied to calculate cumulative values of infiltration using Green and Ampt method, and h_2 from equations (5.1) and (5.2) in each cell. The time step is computed based on cell size and maximum water depth to meet model stability by the Courant–Friedrichs–Lewy (CFL) condition.

The main difference between this model and the method used by Smith (Smith, 1993) is that in this model, sinks do not fill prior the application of the hydrological model. Instead DEM

is to fill sinks with runoff. Therefore, cells that do not have a flow path to the main outlet end up contributing to a depression storage. Once the depression cells' water depth is higher than its neighbors, it can overflow to the next depression or drainage outlet. Thus, flow direction changes when inundation occurs and the water is distributed in the neighboring cells based on potential level. The inundation in one watershed can cause overflow into neighboring watershed over the boundary cells.

5.6.2 Model Validation

HEC-HMS is applied to validate the hydrological model. The computed hydrograph by the hydrological model for two conditions are compared to the HEC-HMS results; pre-development and post-development. For that purpose, a 340 m^2 catchment basin shown in Figure 5.4 is modeled in HEC-HMS. The loss method is considered as Green and Ampt method, and the transform method is set to SCS unit hydrograph. The Green and Ampt parameters are obtained for loamy sand (Rawls, Brakensiek, & Miller, 1983). The lag time is calculated based on the time of concentration which is calculated from the longest overland flow path to the outlet using Arc Hydro. According to NOAA National Weather Service, the 15-minute 100-year design rainfall for the study area is 1.02 inches. The rainfall intensity and distribution is simulated using SCS type II rainfall distribution.

For post development, it is assumed that two rows of panels are installed in the area that covers 80 m^2 of the area. In order to simulate the panels in HEC-HMS model, it is considered that the area covered by panels is impermeable. However, the limitation of this assumption is that there will be infiltration loss for the flow under the panel which cannot be considered in HEC-HMS.

Following the above-mentioned validation, a sensitivity analysis of the model is also conducted. In the following section, the parameter selection for sensitivity analysis is described.

5.6.3 Parameterization and Sensitivity Analysis

In this section, parameter selection and sensitivity analysis are described for single-axis PV technology to compare the effects on the hydrological behavior. Four parameters are identified for sensitivity analysis in post-installation condition; PV panel tilt angle, PV panel orientation angle, antecedent soil moisture, and land preparation practices.

Tilt angle (θ) is the angle in degrees the panel is tilted from flat (Figure 5.7). In single-axis trackers, tilt angle is designed to change in different times in a day to follow the daily movement of the sun. Tilt angle is a parameter that determines the covered area by the panel from top view which ascertains the area under the panel (dry zone). Therefore, depending on the panel's area from top view, the rainfall intensity diverted on the edge line is modified. For sensitivity analysis, eight tilt angles between 0˚ and 77˚ are selected in a way that the covered area under the panel reduces by ~10% in each angle interval. 0˚ represents horizontal panel and it happens at noon, when sun's altitude is maximum. On the other hand, 77˚ refers to maximum tilt angle that happens in early morning and in the evening. The panel width is chosen to be 1.8 meter which is the panel types used in Copper Mountain Solar 1 (Chapter 4). The cell sizes are 20 centimeters which gives the ability to have eight different tilt angles, because one row of covered cells gets exposed to rainfall when tilt angle increases. A rainfall map is created for each tilt angle, and is used in the hydrological model as a representative of spatial rainfall distribution. In each time step, the rainfall depth is multiplied by the number of covered cell (in dry zone) and is applied in the cell row at the edge of the panel (wet zone).

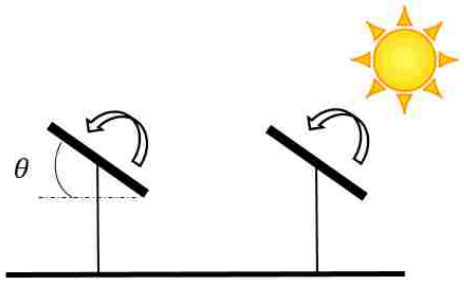

Figure 5.7 Tilt angle

In the Northern Hemisphere, single-axis trackers are generally aligned on a north-south axis. However, in some cases, the axis is tilted (e.g., towards the equator) in order to improve orientation and gain more energy. For sensitivity analysis, regardless of the orientation for the study area, eight orientation angles (φ) from 0˚ to 360˚ are selected to relate the hydrological response to orientation angle of the panel. The rationale of using different orientations is to understand the hydrological behavior for various conditions and applications e.g., similar rain shadowing in urban areas. Figure 5.8 indicates orientation angle for a solar panel. φ is defined as the angle between direction of the watershed's slope and the panels' slope on the horizontal plane (Figure 5.3 and Figure 5.8). For example, when $\varphi = 0^{\circ}$, the panel is facing toward the watershed's slope, and when $\varphi = 180^{\circ}$, the panel is rotated 180˚ in the counterclockwise direction. In Figure 5.1 and Figure 5.2, φ is ~315˚ and ~135˚, respectively.

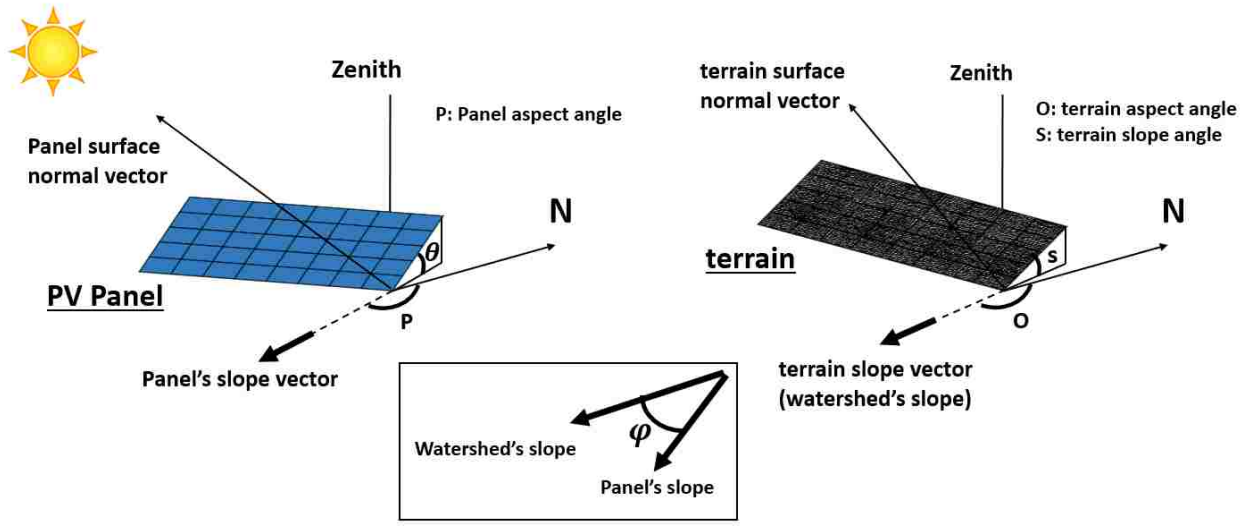

Figure 5.8 Orientation angle (φ)

Antecedent soil moisture reduces infiltration rate (Hardie et al., 2011). The available moisture content in the beginning of the storm is considered as the third parameter for sensitivity analysis. The maximum moisture content is equal to the porosity, which is considered as 0.43 for the study area. Moisture content is expressed as a ratio in which 0 m^3/m^3 represents completely dry soil. Three initial moisture contents, 0, 15, and 30 (m^3/m^3) are used as the antecedent moisture content representing dry, wet, and very wet condition based on the study conducted by Koonce on water balance and soil moisture in the area (Koonce, 2016). Initial moisture content changes available moisture content which is required in the hydrological model to estimate infiltration using Green and Ampt method. However, changes in the soil moisture impact on the hydraulic conductivity and wetting front suction head as well. In this study, for the purpose of sensitivity analysis, the impact of antecedent soil moisture is considered by changing in the available moisture content in the beginning of simulations, and hydraulic conductivity and wetting front suction head are assumed to be constant. Hydraulic conductivity is considered to be affected by site preparation practices as the forth sensitivity analysis parameter.

The last parameter is the site preparation including soil compaction and shrub removal. Soil compaction and shrub removal reduce infiltration rate and surface roughness, respectively. Thus, two conditions are considered, i.e., with and without site preparation. In case of with site preparation, hydraulic conductivity (k) and Manning's coefficient (n) are modified in the study area based on a percentage reduction. It is considered that 20% reduction in Manning's coefficient, and 50% reduction in hydraulic conductivity occurs after site preparation (Gregory, Dukes, Jones, & Miller, 2006; Pitt, Chen, & Clark, 2002).

For the purpose of sensitivity analysis, a 40 m^2 rectangular basin inside the study area is selected for model simulations. The general slope of the ground is toward south with small tilting toward south-west. For pre-development, no solar panel is installed and the rainfall is uniformly distributed in all the cells. Therefore, only antecedent soil moisture and site preparation parameters are considered for sensitivity analysis in pre-development condition.

To determine post-development response, it is assumed that a panel is installed in the middle of the area (1.8 m width and 4 m length) that covers 18% of the area from top view. In general, PV panels cover more area in solar facilities. For example, PV panels cover 43% of the area in Copper Mountain Solar 1. Here, because the panel is going to rotate for different orientation angles, more area needs to be available around the panel to make sure the panel stays within the considered area at all the time. Therefore, the observed effects in the simulations will be augmented in PV solar plants. A total of 384 simulations ($8 \times 8 \times 3 \times 2$) are performed to simulate the runoff for various conditions. The rainfall is not uniformly distributed in all the post-development scenarios. Because PV panel surfaces are impermeable, it is assumed that all the rainfall that falls on the panel's surface will be diverted on the cell row under the edge of the panel (wet zone). It

needs to be mentioned that the time difference between the time that takes for a rain drop to reach the ground and the time that takes to flow on the panel and then reach the ground is ignored. Table 5.1 summarizes the parameters information for sensitivity analysis.

Table 5.1 Parameters information

Parameters	Values
Tilt angle (θ)	$0^{\circ}, 27^{\circ}, 39^{\circ}, 48^{\circ}, 56^{\circ}, 64^{\circ}, 70^{\circ}, 77^{\circ}$
Orientation angles (φ)	$0^{\circ}, 45^{\circ}, 90^{\circ}, 135^{\circ}, 180^{\circ}, 225^{\circ}, 270^{\circ}, 315^{\circ}$
Antecedent soil moisture	Dry: $0\ m^3/m^3$, wet: $15\ m^3/m^3$, very wet: $30\ m^3/m^3$
Site preparation	w/o: $n = 0.03, k = 2.5\ cm/hr$ & w: $n = 0.024, k = 1.25\ cm/hr$

5.7 Results and Discussion

In this section, first, the model validation results are provided. Second, the results of sensitivity analysis are presented and discussed for pre- and post-installation of a PV panel.

5.7.1 Model Validation

Figure 5.9 shows the computed hydrograph from the hydrological model and the simulated hydrograph by HEC-HMS for pre- and post-development. According to the validation results, the calculated peak flow for pre-development using the hydrological model and HEC-HMS simulation are 3.2 $\times 10^4$ cm^3/s and 2.9 $\times 10^4$ cm^3/s, respectively. The peak flow happens in 7.6 minutes for the hydrologic model, and 8 minutes for HEC-HMS. However, it is noted that HEC-HMS creates the runoff for one minute resolution whereas the time resolution of the hydrological model can be determined by user (one second in this case). In post-development, the computed peak flow using the hydrological model and HEC-HMS simulation are 3.12 $\times 10^4$ cm^3/s and 3.1 $\times 10^4$ cm^3/s,

respectively. Runoff volume is increased from pre-development to post-development in both simulations. The calculated peak flow by HEC-HMS is increased after development because the panel area is identified as impermeable. However, in the hydrological model, the panel area is determined as the area that does not receive direct rainfall but not impermeable. That is the reason that the computed peak flow did not increase from pre-development to post-development in the hydrologic model. It should be noticed that according to the results shown in the next section, the orientation of the panels determines if peak flow increases or decreases after installation.

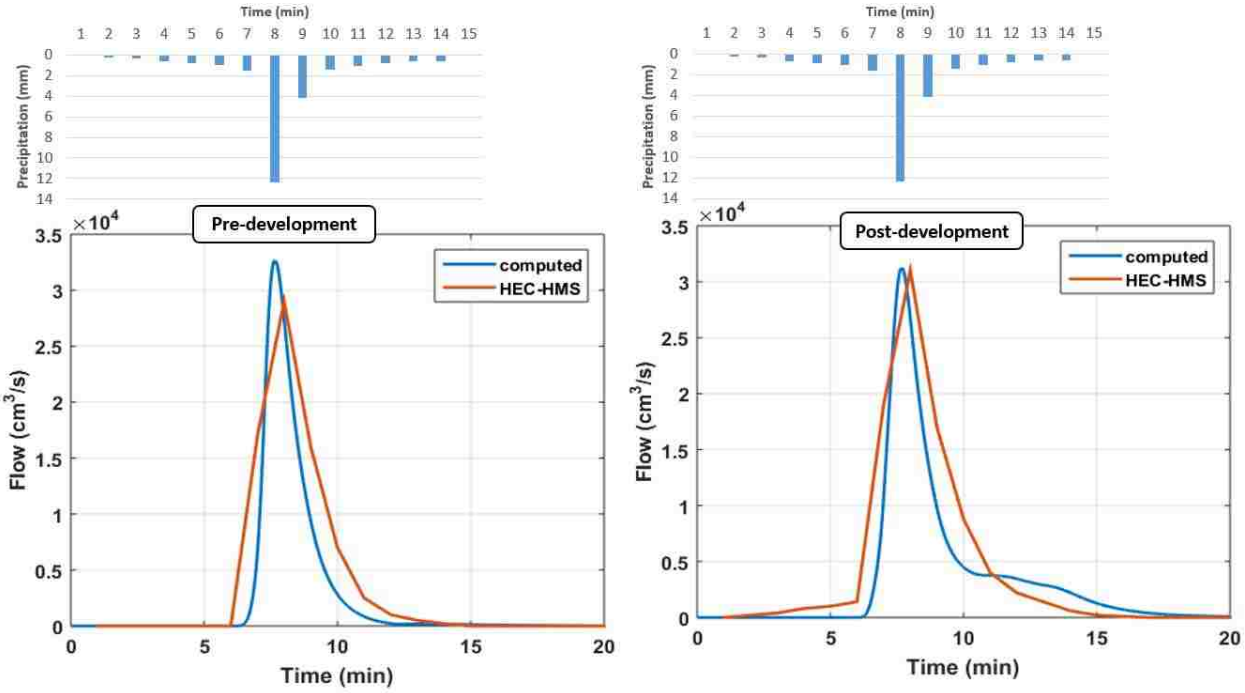

Figure 5.9 Model-computed hydrograph versus HEC-HMS hydrograph for pre- and post-development

The comparison of the computed hydrographs by the hydrological model and HEC-HMS revealed that the hydrological model is validated for further analysis. As a result, the hydrological

model is used to predict the hydrological behavior of the region in pre- and post-installation of the PV panel.

5.7.2 Results of the Sensitivity Analysis

In this section, first, the results of pre-development condition including antecedent soil moisture and site preparation are presented and discussed. Second, the results of sensitivity analysis for post-development including all parameters are shown and discussed.

5.7.2.1 Panel Pre-Development

The hydrological model is applied to simulate the runoff for a 15-min 100-year design rainfall. For the pre-development condition, the sensitivity analysis parameters only include antecedent soil moisture and site preparation as no solar panels are installed yet.

Table 5.2 presents peak flow, peak flow time, and runoff volume for the panel pre-installation. Without consideration of rainfall redistribution effects, the analysis of typical hydrological assessment reports is restricted to the "with" and "without" site preparation practices. Existing practices to design of drainage channels and detention basins at solar facilities are based on the site preparation impacts on hydrological behavior that is shown in Table 5.2.

Table 5.2 Pre-installation model results

Antecedent soil moisture (m^3/m^3)	Peak flow (cm^3/s)		Peak flow time (min)		Runoff volume (cm^3)	
	w site preparation	w/o site preparation	w site preparation	w/o site preparation	w site preparation	w/o site preparation
0	7,891	7,798	7.17	7.21	1,019,019	998,176
15	7,892	7,798	7.17	7.21	1,025,647	1,011,663
30	7,892	7,798	7.17	7.21	1,032,272	1,025,173

According to Table 5.2, site preparation practices increase peak flow and runoff volume, but decrease peak flow time. This is hydrologically intuitive, as shrub removal reduces surface roughness and therefore, runoff velocity increases and the peak flow happens earlier at the outlet point. Moreover, soil compaction reduces infiltration rate and that increases the measured runoff flowrate and runoff volume at the outlet point. On the other hand, runoff volume increases with antecedent soil moisture, but no significant change has been observed in the peak flow and peak flow time for different antecedent soil moistures. Antecedent soil moisture reduces rainfall infiltration loss and thus, runoff volume increases in wet and very wet condition.

5.7.2.2 Panel Post-Development

In this section, the impacts of panel installation on peak flow, peak flow time, and runoff volume are separately discussed. First, the impacts are examined with respect to the panel's orientation angle. Then, the impacts are discussed due to the change in panel tilt angle.

For the post-development, four parameters are evaluated for sensitivity analysis; PV panel tilt angle (θ), PV panel orientation angle (φ), antecedent soil moisture (dry, wet, and very wet), and land preparation practices (w and w/o site preparation). Figure 5.10 shows the calculated hydrological response, i.e., peak flow, peak flow time, and runoff volume, with respect to φ, and Figure 5.11 indicates the calculated hydrological response with respect to the panel tilt angle. Similar to the pre-installation condition, peak flow, peak flow time, and runoff volume have been affected by site preparation practices after panel installation. According to Figure 5.10 and Figure 5.11, the impacts of initial soil moisture can only be identified on runoff volume after panel installation. Figure 5.12 provides more detail about Figure 5.10 and Figure 5.11 with the purpose of comparison of two plots at the same time.

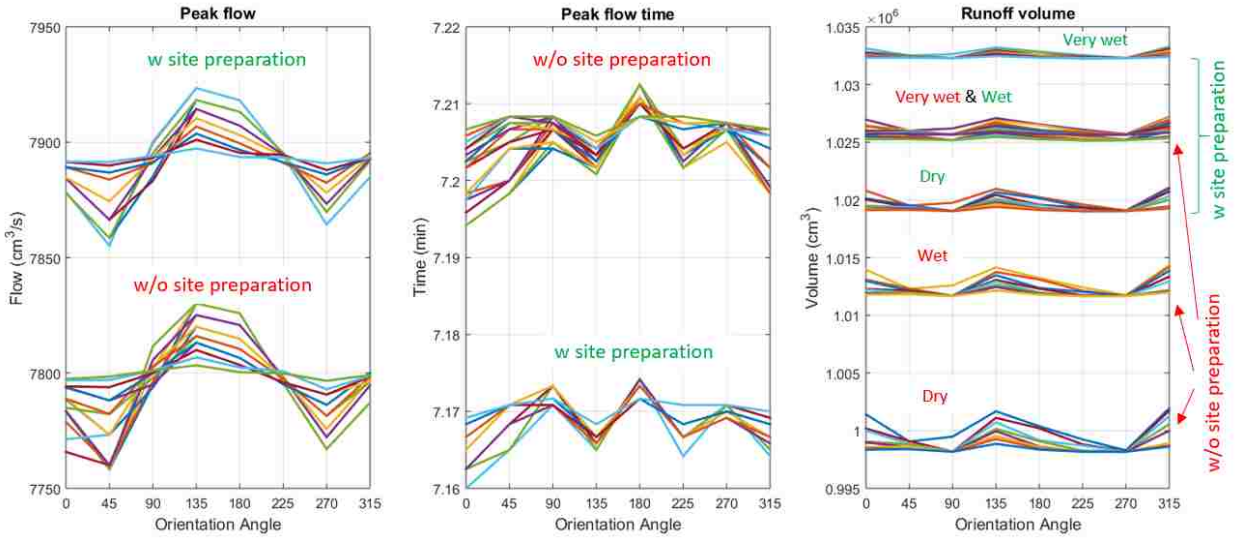

Figure 5.10 The relation between panel orientation angle (φ) and peak flow, peak flow time, and runoff volume. The colored lines represent tilt angles, antecedent soil moisture, and site preparation condition

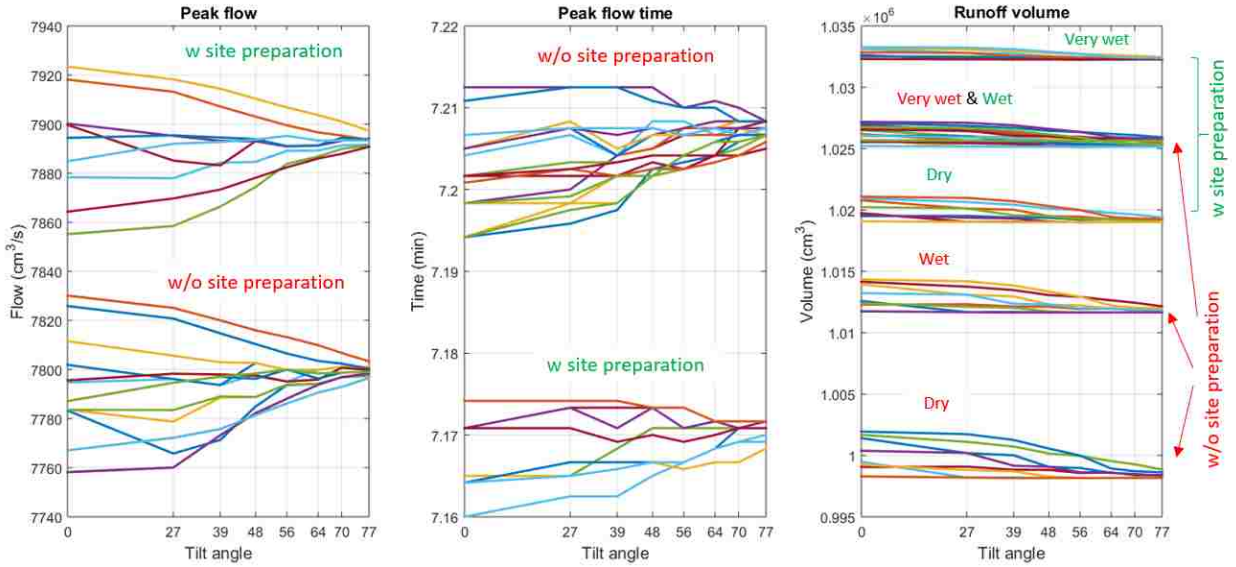

Figure 5.11 The relation between panel tilt angle (θ) and peak flow, peak flow time, and runoff volume. The colored lines represent orientation angles, antecedent soil moisture, and site preparation condition

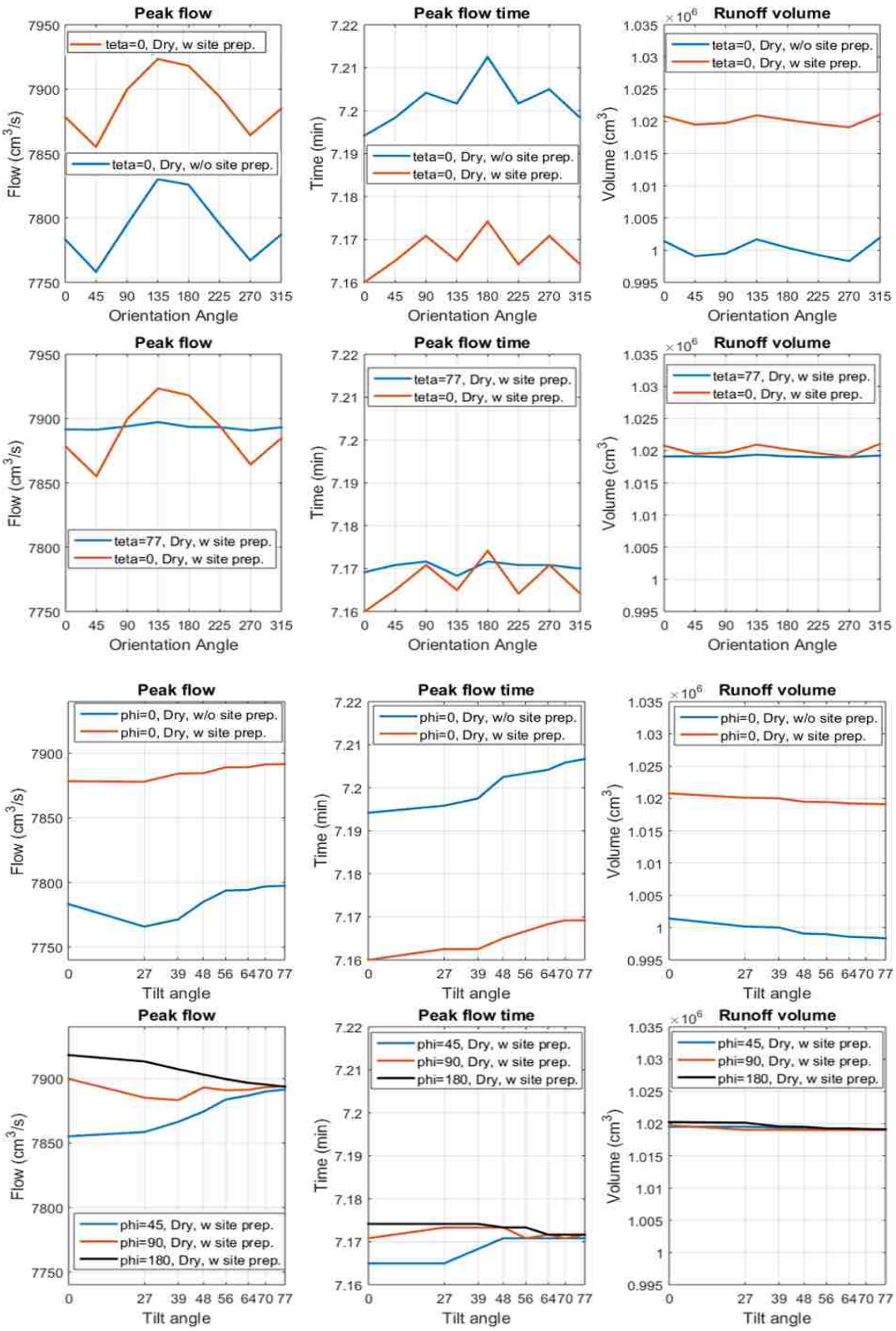

Figure 5.12 Sensitivity analysis results for peak flow, peak flow time and runoff volume

Impacts on peak flow with respect to φ; According to Figure 5.10, the plots of peak flow versus φ can be categorized into two groups, with and without site preparation. In both groups of plots, the periodic variation in peak flow with respect to φ is observed. In general, all the plots show higher peak flow between $\varphi = 90^{\circ}$ and 225° compared to the mean peak flow of all plots. As a result, when wet zone is closer to the watershed outlet point, peak flow is less and vice versa. Higher water depth in the wet zone causes higher runoff velocity compared with the other areas exposed to rainfall. When wet zone is closer to the outlet point ($\varphi = 0^{\circ}, 45^{\circ}, 270^{\circ}, 315^{\circ}$), the peak flow generated in the wet zone (from the peak rainfall intensity) reaches to the outlet point faster than the peak flow generated in other areas. On the other hand, when wet zone is farther from the outlet point ($\varphi = 135^{\circ}, 180^{\circ}$), the peak flow generated in the wet zone reaches to the outlet at the same time with more peak runoff generated in other areas which are closer to the measuring point (due to the difference in the runoff velocity). Therefore, when wet zone is closer to the outlet point, peak flow is less.

Impacts on peak flow time with respect to φ; The two groups of plots (due to site preparation) can also be identified in the plots showing peak flow time versus φ (Figure 5.10). The minimum peak flow time happens when $\varphi = 0^{\circ}$, and the maximum peak flow time happens when $\varphi = 180^{\circ}$. In other words, when $\varphi = 180^{\circ}$, the panel diverts the rainfall to the farthest distance to the outlet point and therefore, it takes more time to reach the outlet point. On the other hand, when $\varphi = 0^{\circ}$, the panel diverts the rainfall to the closest distance to the outlet point and thus, it reaches the outlet point faster. Moreover, compared to pre-installation condition, peak flow happens earlier when $\varphi = 0^{\circ}$, and happens later when $\varphi = 180^{\circ}$.

Impacts on runoff volume with respect to φ; Compared to pre-installation, runoff volume is increased in all orientation angles. Although, the increase in $\varphi = 0^{\circ}, 135^{\circ}$, and 315° is higher, and in $\varphi = 90^{\circ}$, and 270° the increase is lower. It seems if the panel's edge line is perpendicular to the direction of the main tributaries, the increase in runoff volume would be higher in post-installation. The maximum computed increase in runoff volume after panel installation is ~4,000 cm^3, however, the increase after site preparation is ~20,000 cm^3 in pre-installation condition.

In Figure 5.10, the runoff volume versus φ is plotted. Similar to pre-installation, runoff volume is affected by site preparation and antecedent soil moisture. Five groups of plots can be recognized that refers to various soil moisture and site preparation conditions. However, runoff volume plots representing very wet soil without site preparation, and wet soil with site preparation are falling on each other and show similar behavior. In addition, in higher antecedent soil moistures, the variation in runoff volume decreases. This is mostly related to the decrease in infiltration loss due to initial soil moisture. In other words, in higher initial soil moistures, the dry zone located under the panel does not behave as a dry region.

Impacts on peak flow with respect to θ; Similar to Figure 5.10, peak flow, peak flow time, and runoff volume are sensitive to site preparation practice, and only runoff volume is sensitive to antecedent soil moisture change (Figure 5.11). The peak flow plots converge to a single value of peak flow in pre-installation for higher tilt angles (Table 5.2). In fact, the impacts of panel installation on peak flow reduce from $\theta = 0^{\circ}$ to 77° and gets closer to the computed peak flow in pre-installation condition (Table 5.2). In peak flow plots, the maximum peak flows when $\theta = 0^{\circ}$

refers to $\varphi = 180^{\circ}$ and 135°, and the minimum peak flows are obtained when $\varphi = 0^{\circ}$. Therefore, all the peak flow plots representing other orientation angles are fallen between these plots.

The maximum variations in peak flow plots in Figure 5.10 relate to the plots representing $\theta = 0^{\circ}$ (flat panel), and the minimum variations relate to $\theta = 77^{\circ}$ (more details are provided in Figure 5.11 and Figure 5.12). This is because of the reduction in the panel coverage area in the higher tilt angles. In post-installation condition, the minimum computed peak flow without site preparation is 7,758 cm^3/s and the maximum is 7830 cm^3/s. In addition, the minimum computed peak flow with site preparation is 7855 cm^3/s and the maximum is 7923 cm^3/s. Peak flow may increase up to ~70 cm^3/s (0.9%) by panel installation, however, the peak flow increases ~90 cm^3/s (1.2%) by site preparation practices. Therefore, the peak flow modification after panel installation is considerable and has to be taken care of in large solar farms. Moreover, the comparison of peak flow between pre- and post-installation showed that depending on the orientation and tilt angle of the panel, peak flow can increase or decrease after panel installation.

Impacts on peak flow time with respect to θ; The plots of peak flow time with respect to the panel tilt angle are shown in Figure 5.11. Peak flow time plots also converge in higher tilt angles. The minimum peak flow time relates to $\varphi = 0^{\circ}$ and $\theta = 0^{\circ}$, and the maximum peak flow time relates to $\varphi = 180^{\circ}$ and $\theta = 0^{\circ}$. In other words, the peak flow happens earlier when the panel covers more area and the wet zone is closer to the outlet point. In higher tilt angles, the orientation angle of the panel does not significantly impact on the peak flow time. Similar to the peak flow, the variation in the plots showing peak flow time versus φ has a trend in which the variation decreases with tilt angle.

Impacts on runoff volume with respect to θ; According to Figure 5.11, all the computed runoff volumes are higher than the pre-installation condition. Runoff volumes also converge and reduce at higher tilt angles. The maximum runoff volume is observed when $\theta = 0^{\circ}$, and $\varphi = 0^{\circ}, 135^{\circ}$, and 315°. Again, at higher tilt angles, the orientation of the panel does not significantly impact runoff volume. In Figure 5.10, maximum variations in runoff volume plots refer to lower tilt angles ($\theta = 0^{\circ}$) because of the higher ground coverage, and minimum variations relate to higher tilt angles ($\theta = 77^{\circ}$), due to lower ground coverage.

According to the simulation results, the impacts of orientation angle and tilt angle on peak flow and peak flow time are more substantial than antecedent soil moisture. However, the increase in runoff volume for higher initial soil moisture is more than all orientation and tilt angles. Compared with the impacts of site preparation on peak flow, the impacts of panel installation are considerable. Thus, the increase in peak flow caused by site preparation practices can be intensified or reduced depending on the orientation and tilt angles. In other words, the design of drainage channels for peak flow inside PV solar plants can be affected by θ and φ. It should be mentioned that the observed impacts relate to the simulated panel, which covers 17% of the area, and is roughly 1/3 of the coverage ratio in regular PV plants. Thus, the computed impacts shown in Figure 5.10 and Figure 5.11 are expected to be augmented in PV solar farms. However, the increase in runoff volume due to panel installation is significantly smaller than that with soil preparation and antecedent soil moisture. Therefore, from the engineering view, it is unlikely that panel installation makes significant change in the design of detention basins for solar farms.

As mentioned earlier, the typical hydrological reports of solar facilities are focused on changes to soil characteristics due to site preparation. Table 5.3 summarizes the hydrological

impacts of panel installation versus site preparation practices. According to Table 5.3, peak flow is more sensitive to panel installation than other hydrological parameters. Peak flow can be changed up to 0.9% by panel installation. However, runoff volume is more sensitive to site preparation practices than other hydrological parameters. Runoff volume can be changed up to 2% by site preparation practices. Moreover, compared with the impacts of site preparation, the impact of panel installation on peak flow is more, and on runoff volume is less significant than other hydrological parameters. It should be considered that the impact of panel installation is maximum when tilt angle is zero.

Table 5.3 Comparison of the hydrological impacts of panel installation and site preparation practices

Parameters	Peak flow (%)	Peak flow time (%)	Runoff volume (%)
Panel installation	0.9	0.3	0.4
Site preparation	1.2	0.6	2

As discussed earlier, the hydrological impacts of PV installation are more considerable in smaller tilt angles. Therefore, the impacts would be higher at noon because tilt angle is minimum. In addition, in some single-axis PV plants, the panels are designed to be flat after operation time (parking position at night). As a result, the hydrological response due to rainfall between sunset and sunrise will be affected more than any other times in a day due to panel installation.

Since tilt angle changes in different times in the day, orientation angle is also affected by changing the tilt angle. In other words, since the panel track the movement of the sun, the orientation angle alters for single-axis trackers by 180° at noon. For instance, if $\varphi = 0^{\circ}$ in the morning, it will change to 180° in the afternoon. Therefore, peak flow, peak flow time, and runoff

volume are going to behave differently in the storms happening before and after noon. These parameters should be considered in the hydrological assessment of utility-scale PV plants because significant runoff modification may arise due to a large spatial footprint of panel shadowing.

As a result, after panel installation, peak flow decreases and happens earlier when the panel is facing toward the watershed's slope and vice versa. Regardless of the panel orientation, runoff volume increases after panel installation. The impacts of panel installation on peak flow, peak flow time, and runoff volume decrease in higher tilt angles. However, the impacts of panel installation on runoff volume is relatively less than that on peak flow and peak flow time compared to the impacts of site preparation and antecedent soil moisture.

5.8 Summary

In this chapter, hydrological response of pre- and post-installation of a PV panel is studied using high resolution remote sensing DEM. In particular, impacts on peak flow, peak flow time, and runoff volume are investigated using hydrological simulations. Hydrological modeling is performed to identify the impacts of panel orientation angle, panel tilt angle, antecedent soil moisture, and site preparation practices through sensitivity analysis.

A distributed parametric hydrologic model is applied to study the behavior of flow under the influence of PV panels. The model is verified using HEC-HMS for a pre- and post-installation condition. An arid area in southern Nevada is selected for the simulations due to the construction of numerous solar power plants in the region. A total of 384 simulations are preformed to investigate the relationship between hydrological response and the geometry of panels and site properties.

The results of sensitivity analysis show that peak flow, peak flow time, and runoff volume alter after panel installation. It is shown that runoff volume increases after panel installation. Runoff volume has been increased regardless of the orientation and tilt angles. However, as expected, the hydrological impacts reduced with tilt angles. Moreover, the results show that peak flow time decreases when the panel is installed facing toward the watershed's slope and vice versa. In all cases, peak flow time is decreased when $\varphi = 0^{\circ}$, and increased when $\varphi = 180^{\circ}$.

The most significant hydrological impact of panel installation is on the peak flow. It is found that the orientation angle of a PV panel may alter the peak flow as much as site preparation practices can do. The results revealed that when panel is facing toward the watershed's slope, peak flow decreases, and in some cases, below the pre-installation condition. Conversely, when panel is facing in the opposite direction with the watershed's slope, peak flow increases, and in some cases, above the pre-installation condition. However, the impacts are higher when the panel is flat and decreases with tilt angles. The comparison of peak flow between pre- and post-installation showed that depending on the orientation of the panel, peak flow can increase or decrease after panel installation condition.

The time of rainfall is determinative of the expected peak flow at the outlet point. According to the movement of single-axis PV panels, two possible orientation angles can be considered for each plant which have 180° difference. Most single-axis PV trackers are aligned on a north-south axis and thus, the orientation angles switch at noon. Moreover, tilt angle is maximum in the morning and in the evening.

Antecedent soil moisture does not impact peak flow and peak flow time in both pre- and post- installation. However, site preparation and initial moisture content increase runoff volume in

both pre- and post-installation. Panel installation also increases runoff volume; however, the increase is less than the observed runoff volume increase after site preparation and antecedent soil moisture.

Rainfall redistribution effects are not considered in a typical hydrological assessment of solar plants. In this study, it is shown that stormwater drainage design can vary depending on the geometry of the panels. The results reveal that panel orientation and tilt angles is as important as site preparation practices in stormwater channel design to carry runoff peak flow. Here, the simulated panel covers less area than the panels cover in usual solar farms. Thus, the hydrological effects are expected to be augmented when panels cover larger areas. Due to the complexity of the hydrological processes, it is not expected that the measured impacts would linearly increase with increasing the number of panels and in larger areas. However, the observed impacts on the hydrological behavior of one panel is a sign and can be extended in larger spatial extents.

In this study, it is shown that disturbance in the rainfall distribution by USSE plant construction alter hydrological response in the region. The results revealed that the hydrological impacts of rainfall redistribution should not be neglected, specifically the impacts on peak flow. It is shown that the impacts may vary in different times in a day because of the changing in tilt angles and orientation angle from morning to evening. The results of this study revealed that it is imperative to consider the impact of panel installation on spatial rainfall distribution in the hydrological analysis reports and drainage design processes.

6. CHAPTER 6- CONCLUSIONS AND RECOMMENDATIONS

This research investigated the environmental impacts of USSE plants in arid area using remote sensing. Three potential surface impacts are studied including land cover, land surface temperature, and hydrological behavior. This chapter lists the conclusions of this research and recommendations for practitioners and future studies to enhance environmental sustainability of solar energy plants.

6.1 Conclusions

The research was driven by the hypothesis that USSE plants alter land-cover characteristics. It has been investigated with specific objective to measure the change in land cover between pre-, syn-, and post-installation of USSE plants both inside and outside the plants boundary. The results reveal that the high-albedo increases during construction. However, high-albedo decreases after solar panel installation because eventual covering of soil by solar panels. On the other hand, the low-albedo decreases during construction phase but increases after the panel installation. However, panel installation increases the low-albedo fraction because solar panels cover the soil.

The plants studied are from an arid region and show no significant impact on vegetation. The computed vegetation fraction is negligible for pre- and post-development conditions which is representative of the study area physical conditions. The key outcomes about land-cover analysis are as follows.

1. USSE plants do not significantly impact land cover outside the plant boundary. However, within plant area, land-cover radiative characteristics are significantly affected after construction.

2. Site preparation practices including shrub removal and land grading increase high-albedo and decrease low-albedo fractions.

3. Among the applied treatment methods, SMA on PCA-Normalized have the highest accuracy to retrieve subpixel land-cover fraction in USSE plants area. In addition, SMA on MNF-Original is more appropriate to estimate vegetation fraction.

Another hypothesis of this research was that USSE plants alter land surface temperature characteristics. The hypothesis has been investigated with specific objective to determine the change in LST due to USSE plants both inside and outside the plants boundary. The results revealed that shadows casted by solar panels decrease LST inside plants area. Longer shadows in winter cause significant decrease in LST inside plants boundary. The decrease is high during the winters, however, LST in summers are close to pre-development. The key outcomes about land surface temperature analysis are as follows.

4. The LST outside the boundary of the solar plant does not change, whereas it significantly decreases inside the plant at 10 AM after the construction.

5. Inclusion of shadow in the LST analysis improved the explanation of observed trends. The shade analysis revealed that the ground is fully covered with shade in winters which explains the LST reduction at 10 AM.

6. The increase in the high-albedo of the ground prevents the increase in LST in summers inside facilities. Even though the surface temperature of PV panels is relatively high, increase in high-albedo reduces the soil surface temperature after development. Although there is no shade in summers at 10 AM from top view, the LST inside plants area does not increase after development. This is due to the increase in solar reflectivity after site preparation practices.

Lastly, it was hypothesized that PV panels reduce rainfall infiltration loss during a storm and depends on the panel orientation and tilt angle. It has been investigated with specific objective to compare pre and post PV panel installation hydrological responses for single-axis tracking technology. The results revealed that the PV panel installation increases runoff volume during a storm. This is because of the reduction in runoff infiltration loss after panel installation. The increase in runoff volume is higher for smaller tilt angles, because of the larger ground coverage. In addition, if the panel's edge line is perpendicular to the direction of the main tributaries, the increase in runoff volume is higher than post-installation condition.

Runoff peak flow can increase or decrease after panel installation depending on the orientation angle. Peak flow increases for $\varphi = 90^{\circ}$ to 225° and decreases for $\varphi < 90^{\circ}$ or $\varphi > 225^{\circ}$. The increase in peak flow is significant after panel installation compared with site preparation effects on peak flow. In addition, runoff peak flow time may occur earlier or later after panel installation which depends on the orientation angle. The minimum peak flow time happens when $\varphi = 0^{\circ}$, and the maximum peak flow time happens when $\varphi = 180^{\circ}$. This explains that the peak flow happens earlier when the panel covers larger area and the wet zone is closer to the outlet point. The key outcomes about hydrological analysis are as follows.

7. Peak flow, peak flow time, and runoff volume significantly alter after panel installation. After panel installation, peak flow decreases and happens earlier when the panel is facing toward the watershed's slope and vice versa. Regardless of the panel orientation, runoff volume increases after panel installation. The impacts of panel installation on peak flow, peak flow time, and runoff volume decrease in higher tilt angles. However, the impacts of panel installation on runoff volume is relatively less than that on peak flow and peak flow time compared to the impacts of site preparation and antecedent soil moisture.

8. The time of rainfall is determinative of the expected hydrological response. The hydrological impacts would be higher at noon because tilt angle is the minimum. In addition, the impacts would be less in the morning and in the evening, when the tilt angle is the maximum. On the other hand, since the panel track the movement of the sun, the orientation angle alters for single-axis trackers by 180° at noon. Therefore, the impacted behaviors are different before noon compared to the afternoon.

9. Site preparation practices including shrub removal and soil compaction increase peak flow and runoff volume, but reduces peak flow time in both pre- and post-installation of the PV panel. In addition, antecedent soil moisture increases runoff volume, but does not significantly impact on peak flow and peak flow time in both pre- and post-installation of the PV panel.

This research reveals that the impacts of panel installation on spatial rainfall distribution should be considered in hydrological assessment reports. It is shown that a PV panel can significantly reduce or increase runoff peak flow. In addition, panel installation increases runoff volume. These impacts may change stormwater drainage design including channel and detention

basin design after solar plant construction. As mentioned, panel installation can reduce peak flow which means smaller channels are needed to carry the flow, and thus, it can save more money for the project.

This research confirms that remote sensing is an appropriate and powerful tool in the analysis of the environmental impacts of solar facilities. Large spatio-temporal information on land surface characteristics in solar plants area has provided the capability of monitoring and tracking the changes in land surface characteristics.

Overall, USSE plants are environmentally sustainable with insignificant impact outside the plant boundaries. USSE plants in arid regions do not impact land cover and LST in the surrounding. The impacts of USSE plants on land surface characteristics in arid regions are restricted to the area within the plant boundary.

6.2 Recommendation for Practitioners and Policy Makers

In this study, the environmental impacts of USSE plants in arid areas are studied. According to the results, the followings recommendations are made for practitioners and policy makers.

1. It is shown that USSE plants construction do not significantly impact land cover in arid areas outside the plant boundaries. Therefore, less concern needs to be placed regarding installation of a solar plant in the vicinity of areas of critical environmental concern of land cover change. However, proper sitting decisions can help to avoid other possible issues e.g., accidental release of chemicals. Moreover, depending on the location, a specialist

environmental consultant can also provide advice on the specific requirements in each region.

2. Even though the results show no significant impacts on land surface temperature at 10 AM outside the boundaries of solar plants, it is recommended for practitioners to be aware of the possible LST change in other times in a day, especially in areas that are more sensitive to temperature change. In addition, the impacts of panel shading and length of shade in different seasons need to be considered for better understanding of the behavior of vegetation types and growth characteristics inside the facilities.

3. The main recommendation of this study for practitioners and policy makers is to be aware of the hydrological impacts of solar panel installation. According to the results, the impacts of panel installation on spatial rainfall distribution should be considered in hydrological assessment reports. In fact, the impacts of panel installation can be as important as site preparation depending the orientation and tilt angles, especially in peak flow alteration. However, the changes in runoff volume would be less compared with site preparation practices. From the engineering view, it is recommended that practitioners and policy makers consider the orientation and tilt angles of the panels in the design of drainage channels and detention basins in USSE plant areas.

6.3 Recommendations for Future Studies

The followings are recommended for future studies.

1. The impacts of USSE plants on land cover in areas with more vegetation need to be understood. In arid area, since the vegetation fraction is low, no significant impact is

observed due to solar farm installation. It is shown that SMA on MNF-Original is able to estimate vegetation fraction with highest accuracy. Further research is recommended to apply the verified method to estimate the impacts of USSE plants on land cover in areas other than arid regions.

2. The thermal analysis performed in this research was based on the acquired data from Landsat 5 TM and Landsat 8 TIRS at 10 AM. However, the LST behavior might be different in other times in the day. Therefore, further studies on LST inside and outside USSE plants at different times in the day are recommended. Infrared thermal cameras that can be attached to unmanned aerial vehicles would be a good option to obtain LST data anytime in a day with high resolution.

3. In this study, hydrological impacts of one PV panel is studied for various orientation and tilt angles. However, it may not fully reflect the hydrological behavior change in USSE plants with millions of PV panels installed. Further studies are recommended to clarify how peak flow, peak flow time, and runoff volume would change in USSE plants with multiple rows of panels after installation with consideration of spatial rainfall distribution change.

APPENDIX

Renewable and Sustainable Energy Reviews Copyright Agreement

Copyright

Describes the rights related to the publication and distribution of research. It governs how authors (as well as their employers or funders), publishers and the wider general public can use, publish and distribute articles or books.

Journal Author Rights

In order for Elsevier to publish and disseminate research articles, we need publishing rights. This is determined by a publishing agreement between the author and Elsevier. This agreement deals with the transfer or license of the copyright to Elsevier and authors retain significant rights to use and share their own published articles. Elsevier supports the need for authors to share, disseminate and maximize the impact of their research and these rights, in Elsevier proprietary journals* are defined below:

For subscription articles	For open access articles
Authors transfer copyright to the publisher as part of a journal publishing agreement, but have the right to: • Share their article for Personal Use, Internal Institutional Use and Scholarly Sharing purposes, with a DOI link to the version of record on ScienceDirect (and with the Creative Commons CC-BY-NC- ND license for author manuscript versions) • Retain patent, trademark and other intellectual property rights (including research data). • Proper attribution and credit for the published work.	Authors sign an exclusive license agreement, where authors have copyright but license exclusive rights in their article to the publisher**. In this case authors have the right to: • Share their article in the same ways permitted to third parties under the relevant user license (together with Personal Use rights) so long as it contains a CrossMark logo, the end user license, and a DOI link to the version of record on ScienceDirect. • Retain patent, trademark and other intellectual property rights (including research data). • Proper attribution and credit for the published work.

*Please note that society or third party owned journals may have different publishing agreements. Please see the journal's guide for authors for journal specific copyright information.

**This includes the right for the publisher to make and authorize commercial use, please see "Rights granted to Elsevier" for more details.

Rights Granted to Elsevier

For both subscription and open access articles, published in proprietary titles, Elsevier is granted the following rights:

- The exclusive right to publish and distribute an article, and to grant rights to others, including for commercial purposes.
- For open access articles, Elsevier will apply the relevant third party user license where Elsevier publishes the article on its online platforms.
- The right to provide the article in all forms and media so the article can be used on the latest technology even after publication.
- The authority to enforce the rights in the article, on behalf of an author, against third parties, for example in the case of plagiarism or copyright infringement.

Protecting Author Rights

Copyright aims to protect the specific way the article has been written to describe an experiment and the results. Elsevier is committed to its authors to protect and defend their work and their reputation and takes allegations of infringement, plagiarism, ethic disputes and fraud very seriously.

If an author becomes aware of a possible plagiarism, fraud or infringement we recommend contacting their Elsevier publishing contact who can then liaise with our in-house legal department. Note that certain open access user licenses may permit quite broad re-use (https://www.elsevier.com/about/our-business/policies/open-access-licenses) that might otherwise be counted as copyright infringement. For details about how to seek permission to use an article see our permission page.

(https://www.elsevier.com/about/our-business/policies/copyright/permissions)

Personal Use

Authors can use their articles, in full or in part, for a wide range of scholarly, non-commercial purposes as outlined below:

- Use by an author in the author's classroom teaching (including distribution of copies, paper or electronic)
- Distribution of copies (including through e-mail) to known research colleagues for their personal use (but not for Commercial Use)
- Inclusion in a thesis or dissertation (provided that this is not to be published commercially)
- Use in a subsequent compilation of the author's works
- Extending the Article to book-length form
- Preparation of other derivative works (but not for Commercial Use)

- Otherwise using or re-using portions or excerpts in other works

These rights apply for all Elsevier authors who publish their article as either a subscription article or an open access article. In all cases we require that all Elsevier authors always include a full acknowledgement and, if appropriate, a link to the final published version hosted on Science Direct.

REFERENCES

Acciani, G., Falcone, O., & Vergura, S. (2010). Analysis of the thermal heating of poly-Si and a-Si photovoltaic cell by means of Fem. In *International Conference on Renewable Energies and Power Quality*.

Andersen, O., Gilpin, G., & Andrae, A. (2014). Cradle-to-gate life cycle assessment of the dry etching step in the manufacturing of photovoltaic cells. *AIMS Press*, *2*(4), 410–423. https://doi.org/10.3934/energy.2014.4.410

Armstrong, A., Waldron, S., Whitaker, J., & Ostle, N. J. (2014). Wind farm and solar park effects on plant-soil carbon cycling: Uncertain impacts of changes in ground-level microclimate. *Global Change Biology*, *20*(6), 1699–1706. https://doi.org/10.1111/gcb.12437

Artis, D. A., & Carnahan, W. H. (1982). Survey of emissivity variability in thermography of urban areas. *Remote Sensing of Environment*, *12*(4), 313–329. https://doi.org/10.1016/0034-4257(82)90043-8

Barron-Gafford, G. A., Minor, R. L., Allen, N. A., Cronin, A. D., Brooks, A. E., & Pavao-Zuckerman, M. A. (2016). The Photovoltaic Heat Island Effect: Larger solar power plants increase local temperatures. *Scientific Reports*, *6*(October), 35070. https://doi.org/10.1038/srep35070

Bashir, M. A., Ali, H. M., Khalil, S., Ali, M., & Siddiqui, A. M. (2014). Comparison of performance measurements of photovoltaic modules during winter months in Taxila, Pakistan. *International Journal of Photoenergy*, *2014*. https://doi.org/10.1155/2014/898414

Bernal-Agustín, J. L., & Dufo-López, R. (2006). Economical and environmental analysis of grid connected photovoltaic systems in Spain. *Renewable Energy*, *31*(8), 1107–1128. https://doi.org/10.1016/j.renene.2005.06.004

Beylot, A., Payet, J., Puech, C., Adra, N., Jacquin, P., Blanc, I., & Beloin-Saint-Pierre, D. (2014). Environmental impacts of large-scale grid-connected ground-mounted PV installations. *Renewable Energy*, *61*, 2–6. https://doi.org/10.1016/j.renene.2012.04.051

Boardman, J. W. (1994). Geometric mixture analysis of imaging spectrometry data. *Geoscience and Remote Sensing Symposium, 1994. IGARSS '94. Surface and Atmospheric Remote Sensing: Technologies, Data Analysis and Interpretation., International*, *4*, 2369–2371. https://doi.org/doi:10.1109/IGARSS.1994.399740

Bureau of Land Management. (2012). *Approved Resource Management Plan Amendments / Record of Decision (ROD) for Solar Energy Development in Six Southwestern States*.

Bureau of Land Management. (2016). Solar Energy. Retrieved from https://www.blm.gov/wo/st/en/prog/energy/solar_energy.html

Bureau of Land Management, & U.S. Department of Energy. Final Programmatic Environmental Impact Statement (PEIS) for Solar Energy Development in Six Southwestern States (FES 12-24; DOE/EIS-0403), 1 Statewide Agricultural Land Use Baseline 2015 § (2015). https://doi.org/10.1017/CBO9781107415324.004

Calvert, K., Pearce, J. M., & Mabee, W. E. (2013). Toward renewable energy geo-information infrastructures: Applications of GIScience and remote sensing that build institutional capacity. *Renewable and Sustainable Energy Reviews*.

https://doi.org/10.1016/j.rser.2012.10.024

Canty, M. J. (2010). *Image analysis, classification and change detection in remote sensing: With algorithms for ENVI/IDL* (second edi). CRC Press.

Chander, G., Markham, B. L., & Helder, D. L. (2009). Summary of current radiometric calibration coefficients for Landsat MSS, TM, ETM+, and EO-1 ALI sensors. *Remote Sensing of Environment*, *113*(5), 893–903. https://doi.org/10.1016/j.rse.2009.01.007

Charney, J., Stone, P. H., & Quirk, W. J. (1975). Drought in the sahara: a biogeophysical feedback mechanism. *Science (New York, N.Y.)*, *187*(4175), 434–435. https://doi.org/10.1126/science.187.4175.434

Chen, W., Sakai, T., Moriya, K., Koyama, L., & Cao, C. X. (2013). Estimation of Vegetation Coverage in Semi-arid Sandy Land Based on Multivariate Statistical Modeling Using Remote Sensing Data. *Environmental Modeling & Assessment*, *18*(5), 547–558. https://doi.org/Doi 10.1007/S10666-013-9359-1

Chiabrando, R., Fabrizio, E., & Garnero, G. (2009). The territorial and landscape impacts of photovoltaic systems: Definition of impacts and assessment of the glare risk. *Renewable and Sustainable Energy Reviews*, *13*(9), 2441–2451. https://doi.org/10.1016/j.rser.2009.06.008

Cho, J., Yeh, P. J.-F., Lee, Y.-W., Kim, H., Oki, T., Kanae, S., … Otsuki, K. (2010). A study on the relationship between Atlantic sea surface temperature and Amazonian greenness. *Ecological Informatics*, *5*(5), 367–378. https://doi.org/10.1016/j.ecoinf.2010.05.005

Cook, L. M., & McCuen, R. H. (2013). Hydrologic Response of Solar Farms. *Journal of*

Hydrologic Engineering, *18*(5), 536–541. https://doi.org/10.1061/(ASCE)HE.1943-5584.0000530

de Jong, R., de Bruin, S., de Wit, A., Schaepman, M. E., & Dent, D. L. (2011). Analysis of monotonic greening and browning trends from global NDVI time-series. *Remote Sensing of Environment*, *115*(2), 692–702. https://doi.org/10.1016/j.rse.2010.10.011

De Marco, A., Petrosillo, I., Semeraro, T., Pasimeni, M. R., Aretano, R., & Zurlini, G. (2014). The contribution of Utility-Scale Solar Energy to the global climate regulation and its effects on local ecosystem services. *Global Ecology and Conservation*, *2*, 324–337. https://doi.org/10.1016/j.gecco.2014.10.010

Denholm, P., & Margolis, R. M. (2008). Land-use requirements and the per-capita solar footprint for photovoltaic generation in the United States. *Energy Policy*, *36*(9), 3531–3543. https://doi.org/10.1016/j.enpol.2008.05.035

Di Leo, N., Escobedo, F. J., & Dubbeling, M. (2016). The role of urban green infrastructure in mitigating land surface temperature in Bobo-Dioulasso, Burkina Faso. *Environment, Development and Sustainability*, *18*(2), 373–392. https://doi.org/10.1007/s10668-015-9653-y

Edalat, M. M., & Stephen, H. (2017). Effects of two utility-scale solar energy plants on land-cover patterns using SMA of Thematic Mapper data. *Renewable and Sustainable Energy Reviews*. https://doi.org/10.1016/j.rser.2016.09.079

El Chaar, L., Lamont, L. A., & El Zein, N. (2011). Review of photovoltaic technologies. *Renewable and Sustainable Energy Reviews*. https://doi.org/10.1016/j.rser.2011.01.004

Elmore, A. J., Mustard, J. F., Manning, S. J., & Lobell, D. B. (2000). Quantifying Vegetation Change in Semiarid Environments. *Remote Sensing of Environment*, *73*(1), 87–102. https://doi.org/10.1016/S0034-4257(00)00100-0

Eltahir, E. A. B. (1996). Precipitation Recycling. *Reviews of Geophysics*. https://doi.org/10.1029/96rg01927

Fensholt, R., Rasmussen, K., Nielsen, T. T., & Mbow, C. (2009). Evaluation of earth observation based long term vegetation trends - Intercomparing NDVI time series trend analysis consistency of Sahel from AVHRR GIMMS, Terra MODIS and SPOT VGT data. *Remote Sensing of Environment*, *113*(9), 1886–1898. https://doi.org/10.1016/j.rse.2009.04.004

Fthenakis, V., & Yu, Y. (2013). Analysis of the potential for a heat island effect in large solar farms. *2013 IEEE 39th Photovoltaic Specialists Conference (PVSC)*, 3362–3366. https://doi.org/10.1109/PVSC.2013.6745171

Green, A. A., Berman, M., Switzer, P., & Graig, M. D. (1988). A transformation for ordering multispectral data in term of image quality with implications for noise removal. *IEEE Transactions on Geoscience and Remote Sensing*, *26*(1), 65–74.

Gregory, J., Dukes, M., Jones, P., & Miller, G. (2006). Effect of urban soil compaction on infiltration rate. *Journal of Soil and Water Conservation*, *61*(3), 117–124.

Grippo, M., Hayse, J. W., & O'Connor, B. L. (2015). Solar energy development and aquatic ecosystems in the southwestern United States: potential impacts, mitigation, and research needs. *Environmental Management*, *55*(1), 244–256. https://doi.org/10.1007/s00267-014-0384-x

Gunerhan, H., Hepbasli, A., & Giresunlu, U. (2008). Environmental Impacts from the Solar Energy Systems. *Energy Sources, Part A: Recovery, Utilization, and Environmental Effects*, *31*(2), 131–138. https://doi.org/10.1080/15567030701512733

Hardie, M. A., Cotching, W. E., Doyle, R. B., Holz, G., Lisson, S., & Mattern, K. (2011). Effect of antecedent soil moisture on preferential flow in a texture-contrast soil. *Journal of Hydrology*, *398*(3–4), 191–201. https://doi.org/10.1016/j.jhydrol.2010.12.008

Hernandez, R. R., Easter, S. B., Murphy-Mariscal, M. L., Maestre, F. T., Tavassoli, M., Allen, E. B., … Allen, M. F. (2014). Environmental impacts of utility-scale solar energy. *Renewable and Sustainable Energy Reviews*, *29*, 766–779. https://doi.org/10.1016/j.rser.2013.08.041

Hernandez, R. R., Hoffacker, M. K., & Field, C. B. (2014). Land-use efficiency of big solar. *Environmental Science and Technology*, *48*(2), 1315–1323. https://doi.org/10.1021/es4043726

Hernandez, R. R., Hoffacker, M. K., & Field, C. B. (2015). Efficient use of land to meet sustainable energy needs. *Nature Climate Change*, *5*(4), 353–358. https://doi.org/10.1038/nclimate2556

Home: W.M. Keck Earth Sciences & Mining Research Information Center. (n.d.). Retrieved November 13, 2015, from http://keck.library.unr.edu/

Horner, R. M., & Clark, C. E. (2013). Characterizing variability and reducing uncertainty in estimates of solar land use energy intensity. *Renewable and Sustainable Energy Reviews*, *23*, 129–137. https://doi.org/10.1016/j.rser.2013.01.014

Hosenuzzaman, M., Rahim, N. A., Selvaraj, J., Hasanuzzaman, M., Malek, A. B. M. A., &

Nahar, A. (2015). Global prospects, progress, policies, and environmental impact of solar photovoltaic power generation. *Renewable and Sustainable Energy Reviews*. https://doi.org/10.1016/j.rser.2014.08.046

Hulley, G. C., & Hook, S. J. (2009). The North American ASTER Land Surface Emissivity Database (NAALSED) Version 2.0. *Remote Sensing of Environment*, *113*(9), 1967–1975. https://doi.org/10.1016/j.rse.2009.05.005

Hulley, G. C., & Hook, S. J. (2011). Generating consistent land surface temperature and emissivity products between ASTER and MODIS data for earth science research. *IEEE Transactions on Geoscience and Remote Sensing*, *49*(4), 1304–1315. https://doi.org/10.1109/TGRS.2010.2063034

Jimenez-Munoz, J. C., Sobrino, J. A., Skokovic, D., Mattar, C., & Cristobal, J. (2014). Land surface temperature retrieval methods from landsat-8 thermal infrared sensor data. *IEEE Geoscience and Remote Sensing Letters*, *11*(10), 1840–1843. https://doi.org/10.1109/LGRS.2014.2312032

Johnson, P. E., Smith, M. O., & Adams, J. B. (1985). Quantitative analysis of planetary reflectance spectra with principal components analysis. *Journal of Geophysical Research Supplement*, *90*, 805-. Retrieved from http://ads.nao.ac.jp/cgi-bin/nph-bib_query?bibcode=1985JGRS...90..805J&db_key=AST

Johnson, R. A., & Wichern, D. W. (1992). *Applied Multivariate Statistical Analysis*. *Prentice Hall*. https://doi.org/10.1198/tech.2005.s319

Jolliffe, I. . T. (2002). *Principal Component Analysis*. *Springer Series in Statistics*.

https://doi.org/10.1007/b98835

Jomaa, I., Auda, Y., Saleh, B. A., Hamze, M., & Safi, S. (2008). Landscape spatial dynamics over 38 years under natural and anthropogenic pressures in Mount Lebanon. *Landscape and Urban Planning*, *87*(1), 67–75. https://doi.org/10.1016/j.landurbplan.2008.04.007

Jungbluth, N. (2005). Life cycle assessment of crystalline photovoltaics in the Swiss ecoinvent database. *Progress in Photovoltaics: Research and Applications*. https://doi.org/10.1002/pip.614

Kendall, M. G. (1955). *Rank correlation methods*. *Griffin: London*.

Klein, S. J. W., & Rubin, E. S. (2013). Life cycle assessment of greenhouse gas emissions, water and land use for concentrated solar power plants with different energy backup systems. *Energy Policy*, *63*, 935–950. https://doi.org/10.1016/j.enpol.2013.08.057

Koonce, J. (2016, May 1). *Water Balance and Moisture Dynamics of an Arid and Semi-Arid Soil: A Weighing Lysimeter and Field Study*. *UNLV Theses, Dissertations, Professional Papers, and Capstones*. Retrieved from http://digitalscholarship.unlv.edu/thesesdissertations/2692

Lagarias, J. C., Reeds, J. a., Wright, M. H., & Wright, P. E. (1998). Convergence Properties of the Nelder--Mead Simplex Method in Low Dimensions. *SIAM Journal on Optimization*, *9*(1), 112–147. https://doi.org/10.1137/S1052623496303470

Lambin, E. F., & Geist, H. (2006). *Land-use and land-cover change: local processes and global impacts*. *Global Change* (Vol. 43). https://doi.org/10.1007/s00267-008-9263-7

Li, Z.-L., Wu, H., Wang, N., Qiu, S., Sobrino, J. A., Wan, Z., … Yan, G. (2013). Land surface

emissivity retrieval from satellite data. *International Journal of Remote Sensing*, *34*(9–10), 3084–3127. https://doi.org/10.1080/01431161.2012.716540

Lu, D., & Weng, Q. (2004). Spectral Mixture Analysis of the Urban Landscape in Indianapolis with Landsat ETM + Imagery. *Photogrammetric Engineering & Remote Sensing*, *70*(9), 1053–1062.

M.M. Aman, K.H. Solangi, M.S. Hossain, A. Badarudin, G.B. Jasmon, H. Mokhlis, … S.N Kazi. (2015). A review of Safety, Health and Environmental (SHE) issues of solar energy system. *Renewable and Sustainable Energy Reviews*, *41*, 1190–1204. https://doi.org/10.1016/j.rser.2014.08.086

Mahtta, R., Joshi, P. K., & Jindal, A. K. (2014). Solar power potential mapping in India using remote sensing inputs and environmental parameters. *Renewable Energy*, *71*, 255–262. https://doi.org/10.1016/j.renene.2014.05.037

Mann, H. B. (1945). Nonparametric Tests Against Trend. *Mann Source: Econometrica*, *13*(3), 245–259. https://doi.org/10.1017/CBO9781107415324.004

Masson, V., Bonhomme, M., Salagnac, J.-L., Briottet, X., & Lemonsu, A. (2014). Solar panels reduce both global warming and urban heat island. *Frontiers in Environmental Science*, *2*(June), 1–10. https://doi.org/10.3389/fenvs.2014.00014

Mei, S., He, M., Wang, Z., & Feng, D. (2010). Spatial Purity Based Endmember Extraction for Spectral Mixture Analysis. *IEEE Transactions on Geoscience and Remote Sensing*, *48*(9), 3434–3445. https://doi.org/10.1109/TGRS.2010.2046671

Mekhilef, S., Saidur, R., & Safari, A. (2011). A review on solar energy use in industries.

Renewable and Sustainable Energy Reviews. https://doi.org/10.1016/j.rser.2010.12.018

Murphy, D. J., Horner, R. M., & Clark, C. E. (2015). The impact of off-site land use energy intensity on the overall life cycle land use energy intensity for utility-scale solar electricity generation technologies. *Journal of Renewable and Sustainable Energy*, *7*(3), 33116. https://doi.org/10.1063/1.4921650

NAIP Imagery. (n.d.). Retrieved November 13, 2015, from http://www.fsa.usda.gov/programs-and-services/aerial-photography/imagery-programs/naip-imagery/index

Neeti, N., & Eastman, J. R. (2011). A Contextual Mann-Kendall Approach for the Assessment of Trend Significance in Image Time Series. *Transactions in GIS*, *15*(5), 599–611. https://doi.org/10.1111/j.1467-9671.2011.01280.x

Nellis Air Force Base - Nellis Solar Array. (n.d.). Retrieved November 13, 2015, from http://www.nellis.af.mil/library/nellissolararray.asp

Nevada Solar One. (n.d.). Retrieved November 13, 2015, from http://www.acciona-energia.com/activity_areas/csp/installations/nevadasolarone/nevada-solar-one.aspx

Ong, S., Campbell, C., Denholm, P., Margolis, R., & Heath, G. (2013). *Land-Use Requirements for Solar Power Plants in the United States*. *NREL/TP-6A20-56290*. Retrieved from http://www.nrel.gov/docs/fy13osti/56290.pdf

Otterman, J. (1974). Baring high-albedo soils by overgrazing: a hypothesized desertification mechanism. *Science (New York, N.Y.)*. https://doi.org/10.1126/science.186.4163.531

Owe, M., & Vandegriend, A. A. (1993). On the Relationship Between Thermal Emissivity and the Normalized Difference Vegetation Index for Natural Surfaces. *International Journal of*

Remote Sensing;14 (6): 1119-1131 Apr 1993, *14*(December 2012), 37–41. https://doi.org/10.1080/01431169308904400

Pacca, S., Sivaraman, D., & Keoleian, G. A. (2007). Parameters affecting the life cycle performance of PV technologies and systems. *Energy Policy*, *35*(6), 3316–3326. https://doi.org/10.1016/j.enpol.2006.10.003

Parida, B., Iniyan, S., & Goic, R. (2011). A review of solar photovoltaic technologies. *Renewable and Sustainable Energy Reviews*. https://doi.org/10.1016/j.rser.2010.11.032

Phillips, J. (2013). Determining the sustainability of large-scale photovoltaic solar power plants. *Renewable and Sustainable Energy Reviews*, *27*, 435–444. https://doi.org/10.1016/j.rser.2013.07.003

Pitt, R., Chen, S.-E., & Clark, S. (2002). Compacted Urban Soils Effects on Infiltration and Bioretention Stormwater Control Designs. In *Ninth International Conference on Urban Drainage (9ICUD)*. https://doi.org/https://doi.org/10.1061/40644(2002)14

Plaza, A., Martinez, P., Perez, R., & Plaza, J. (2002). Spatial/spectral endmember extraction by multidimensional morphological operations. *IEEE Transactions on Geoscience and Remote Sensing*, *40*(9), 2025–2041. https://doi.org/10.1109/TGRS.2002.802494

Qian, C. (2014). Impact of land use/land cover change on changes in surface solar radiation in eastern China since the reform and opening up. *Theoretical and Applied Climatology*, 1–9. https://doi.org/10.1007/s00704-014-1334-5

Quattrochi, C. P. L. D. A., & Luvall, J. C. (1997). Application of high-resolution thermal infrared remote sensing and GIS to assess the urban heat island effect. *International Journal*

of Remote Sensing, *18*(2), 287–304. https://doi.org/10.1080/014311697219079

Rawls, W. J., Brakensiek, D. L., & Miller, N. (1983). Green- ampt Infiltration Parameters from Soils Data. *Journal of Hydraulic Engineering*, *109*(1), 62–70. https://doi.org/10.1061/(ASCE)0733-9429(1983)109:1(62)

Rogan, J., Franklin, J., & Roberts, D. A. (2002). A comparison of methods for monitoring multitemporal vegetation change using Thematic Mapper imagery. *Remote Sensing of Environment*, *80*(1), 143–156. https://doi.org/10.1016/S0034-4257(01)00296-6

Smith, M. B. (1993). A Gis-Based Distributed Parameter Hydrologic Model for Urban Areas. *Hydrological Processes*, *7*(1), 45–61. https://doi.org/10.1002/hyp.3360070106

Sobrino, J. A., Jiménez-Muñoz, J. C., & Paolini, L. (2004). Land surface temperature retrieval from LANDSAT TM 5. *Remote Sensing of Environment*, *90*(4), 434–440. https://doi.org/10.1016/j.rse.2004.02.003

Sobrino, J. A., Jiménez-Muñoz, J. C., Sòria, G., Romaguera, M., Guanter, L., Moreno, J., … Martínez, P. (2008). Land surface emissivity retrieval from different VNIR and TIR sensors. In *IEEE Transactions on Geoscience and Remote Sensing* (Vol. 46, pp. 316–327). https://doi.org/10.1109/TGRS.2007.904834

Sobrino, J. A., Jiménez-Muñoz, J. C., & Verhoef, W. (2005). Canopy directional emissivity: Comparison between models. *Remote Sensing of Environment*, *99*(3), 304–314. https://doi.org/10.1016/j.rse.2005.09.005

Sobrino, J. A., Raissouni, N., & Li, Z.-L. (2001). A Comparative Study of Land Surface Emissivity Retrieval from NOAA Data. *Remote Sensing of Environment*, *75*(2), 256–266.

https://doi.org/10.1016/S0034-4257(00)00171-1

Solangi, K. H., Islam, M. R., Saidur, R., Rahim, N. A., & Fayaz, H. (2011). A review on global solar energy policy. *Renewable and Sustainable Energy Reviews*. https://doi.org/10.1016/j.rser.2011.01.007

Solar Energy Industries Association. (2016). *Major Solar Projects in the United StatesOperating, Under Construction, or Under Development*. Retrieved from http://www.seia.org/research-resources/major-solar-projects-list/seia-major-solar-projects-list-update

Song, C. (2005). Spectral mixture analysis for subpixel vegetation fractions in the urban environment: How to incorporate endmember variability? *Remote Sensing of Environment*, *95*(2), 248–263. https://doi.org/10.1016/j.rse.2005.01.002

Taha, H. (2013). The potential for air-temperature impact from large-scale deployment of solar photovoltaic arrays in urban areas. *Solar Energy*, *91*, 358–367. https://doi.org/10.1016/j.solener.2012.09.014

Thenkabail, P. (2016). *Remote sensing of water resources, disasters, and urban studies*. CRC Press.

Thomlinson, J. R., Bolstad, P. V., & Cohen, W. B. (1999). Coordinating methodologies for scaling landcover classifications from site-specific to global: Steps toward validating global map products. *Remote Sensing of Environment*, *70*(1), 16–28. https://doi.org/10.1016/S0034-4257(99)00055-3

Tottrup, C., & Rasmussen, M. S. (2004). Mapping long-term changes in savannah crop

productivity in Senegal through trend analysis of time series of remote sensing data. *Agriculture, Ecosystems and Environment*, *103*(3), 545–560. https://doi.org/10.1016/j.agee.2003.11.009

Tsoutsos, T., Frantzeskaki, N., & Gekas, V. (2005). Environmental impacts from the solar energy technologies. *Energy Policy*, *33*(3), 289–296. https://doi.org/10.1016/S0301-4215(03)00241-6

Turney, D., & Fthenakis, V. (2011). Environmental impacts from the installation and operation of large-scale solar power plants. *Renewable and Sustainable Energy Reviews*, *15*(6), 3261–3270. https://doi.org/10.1016/j.rser.2011.04.023

Tyagi, V. V., Rahim, N. A. A., Rahim, N. A., & Selvaraj, J. A. L. (2013). Progress in solar PV technology: Research and achievement. *Renewable and Sustainable Energy Reviews*, *20*, 443–461. https://doi.org/10.1016/j.rser.2012.09.028

USDA NRCS. (2017). USDA Web Soil Survey. Retrieved from https://websoilsurvey.nrcs.usda.gov/app/WebSoilSurvey.aspx

USGS National Gap Analysis Program. (2017). Land Cover Viewer - Map. Retrieved May 21, 2017, from https://gis1.usgs.gov/csas/gap/viewer/land_cover/Map.aspx

Verbesselt, J., Hyndman, R., Newnham, G., & Culvenor, D. (2010). Detecting trend and seasonal changes in satellite image time series. *Remote Sensing of Environment*, *114*(1), 106–115. https://doi.org/10.1016/j.rse.2009.08.014

Voogt, J. A., & Oke, T. R. (2003). Thermal remote sensing of urban climates. *Remote Sensing of Environment*. https://doi.org/10.1016/S0034-4257(03)00079-8

Walraven, R. (1978). Calculating the position of the sun. *Solar Energy*, *20*(5), 393–397. https://doi.org/10.1016/0038-092X(78)90155-X

Wang, W., Yao, X., Ji, M., & Zhang, J. (2014). Spectral data treatments for impervious endmember derivation and fraction mapping from Landsat ETM+ imagery: a comparative analysis. *Frontiers of Earth Science*. https://doi.org/10.1007/s11707-014-0456-5

Weng, Q. (2001). A remote sensing?GIS evaluation of urban expansion and its impact on surface temperature in the Zhujiang Delta, China. *International Journal of Remote Sensing*, *22*(10), 1999–2014. https://doi.org/10.1080/713860788

Weng, Q. (2003). Fractal analysis of satellite-detected urban heat island effect. *Photogrammetric Engineering and Remote Sensing*, *69*(5), 555–566. Retrieved from http://www.scopus.com/inward/record.url?eid=2-s2.0-0038814823&partnerID=40&md5=660046c153d254404bba15e0f93b811f

Weng, Q. (2009). Thermal infrared remote sensing for urban climate and environmental studies: Methods, applications, and trends. *ISPRS Journal of Photogrammetry and Remote Sensing*, *64*(4), 335–344. https://doi.org/10.1016/j.isprsjprs.2009.03.007

Weng, Q., Lu, D., & Schubring, J. (2004). Estimation of land surface temperature-vegetation abundance relationship for urban heat island studies. *Remote Sensing of Environment*, *89*(4), 467–483. https://doi.org/10.1016/j.rse.2003.11.005

Wolfe, P. (2013). *Solar photovoltaic projects in the mainstream power market* (First). Routledge.

Wu, C., & Murray, A. T. (2003). Estimating impervious surface distribution by spectral mixture analysis. *Remote Sensing of Environment*, *84*(4), 493–505. https://doi.org/10.1016/S0034-

4257(02)00136-0

Yu, X., Guo, X., & Wu, Z. (2014). Land surface temperature retrieval from landsat 8 TIRS-comparison between radiative transfer equation-based method, split window algorithm and single channel method. *Remote Sensing*, *6*(10), 9829–9852. https://doi.org/10.3390/rs6109829

Zhang, J., Lv, F., & Zhang, L. (2012). Discussion on Environment Impact Assessment in the Lifecycle of PV Systems. *Energy Procedia*, *16*, 234–239. https://doi.org/10.1016/j.egypro.2012.01.039

CURRICULUM VITAE

Graduate College

University of Nevada, Las Vegas

Mohammad Masih Edalat

Email Address:

Mohammad.edalat@unlv.edu

Degrees:

Bachelor of Science, Civil Engineering, 2009

Islamic Azad University Najafabad Branch, Iran

Master of Science, Environmental Engineering, 2012

Shiraz University, Iran

Dissertation Title:

Remote sensing of the environmental impacts of utility-scale solar energy plants

Dissertation Examination Committee:

Chairperson, Dr. Haroon Stephen, Ph.D.

Committee Member, Dr. Sajjad Ahmad, Ph.D.

Committee Member, Dr. Jacimaria Batista, Ph.D.

Committee Member, Dr. Ashok Singh, Ph.D.

Graduate College Faculty Representative, Dr. Dale Devitt, Ph.D.